THE UNIVERSITY OF CHICAGO

DEVELOPMENT AND KINETIC ANALYSIS OF EMERGING POSITRON EMISSION TOMOGRAPHY RADIOTRACER VANDIUM-48-LABELED VANADYL ACETYLACETONATE

A DISSERTATION SUBMITTED TO
THE FACULTY OF THE DIVISION OF THE BIOLOGICAL SCIENCES
AND THE PRITZKER SCHOOL OF MEDICINE
IN CANDIDACY FOR THE DEGREE OF
DOCTOR OF PHILOSOPHY

COMMITTEE ON MEDICAL PHYSICS

BY
BRITTANY ANNJEAN BRODER

CHICAGO, ILLINOIS
JUNE 2022

"You cannot hope to build a better world without improving the individuals. To that end, each of us must work for his own improvement and, at the same time, share a general responsibility for all humanity."

-Marie Curie

TABLE OF CONTENTS

LIST OF FIGURES

LIST OF TABLES

ACKNOWLEDGMENTS

I am grateful to have benefited from the guidance of many people during my time at the University of Chicago. I would like to thank my advisor, Chin-Tu Chen, for his support, encouragement, and mentorship. He has helped me grow as a scientist and provided me with career advice that has proved invaluable in shaping my career path. I am honored to have been advised by such a reputable and knowledgeable scientist.

The members of my thesis committee have been invaluable in shaping this dissertation. I am grateful for their guidance, support, and scientific expertise in their respective areas. Dr. Bill O'Brien-Penney has provided his clinical expertise, helping to maintain a sense of the bigger picture in this research. Dr. Chien-Min Kao has been helpful in developing the kinetic modelling methods. Dr. Richard Freifelder has provided immeasurable guidance in the cyclotron production of ^{48}V; I appreciate the time he has dedicated to not only the experimental production of the radioisotope, but also teaching me about radioisotope production.

I want to acknowledge several members of the UC Cylotron Facility and Integrated Small Animal Imaging Research Resource (iSAIRR) who have contributed their expertise to this work. Anna Kucharski dedicated significant time to operating the cyclotron for the ^{48}V production. Dr. Mohammed Bhuiyan provided guidance in developing the compound characterization and chemistry synthesis methods described. Dr. Hannah Zhang provided guidance in developing the cell and animal studies. Dr. Lara Leoni provided assistance in conducting animal studies. Dr. Aaron Hsiu-Ming Tsai did the PET image reconstruction and provided guidance on the image analysis. Their contributions over the years have made these studies possible and enhanced my knowledge of radiotracer studies.

Several collaborators have provided guidance in the experimental methods of this work. Dr. Marvin W. Makinen (University of Chicago) provided guidance in developing the characterization procedures and synthesis procedures. Dr. Devkumar Mustafi (University of

Chicago) provided guidance on the cell lines to use. Dr. David Rotsch (Argonne National Laboratory) contributed to the compound separation and characterization methods. Dr. Jerry Nolen (Argonne National Laboratory) provided guidance on the TOPAS simulations.

I have appreciated the camaraderie of the Graduate Program in Medical Physics (GPMP) students and especially my classmates, Inna, Isabelle, and Jordan. I am also thankful for my friends in the BSD, many of whom I met on day one and have been some of my closest friends ever since. I am fortunate to have met so many wonderful, smart people.

I want to thank the GPMP faculty who taught courses and the GPMP administrative staff for their help over the years.

Last, I would like to thank my family. Their unwavering love and encouragement has helped propel me through this journey. They have supported me from the beginning, even when I decided to go to school for, as my dad put it, "the foreseeable future." My husband, Mahmoud, has kept me going when I faltered, gave encouragement when I needed support, and motivated me with countless pastries and baklava. I am grateful for such a wonderful support system.

ABSTRACT

Vanadyl acetylacetonate ($VO(acac)_2$) has shown promise as a magnetic resonance imaging (MRI) agent due to its high selectivity for cancer cells, which could facilitate differentiation of carcinogenesis stages progressing from inflammation to malignant tumor. This is especially vital for types of cancer where inflammation is a recognized component or precursor for tumorigenesis, such as colorectal cancer (CRC) [32]. The novel positron emission tomography (PET) radiotracer vanadium-48-labeled-$VO(acac)_2$ ($^{48}VO(acac)_2$) is a positron-emitting, long-lived ($t_{1/2} = 16$ days) chelated compound that could be used for physiological monitoring of relatively long biological processes not feasible with other modalities or using other radiotracers due to the high sensitivity of PET. This radiotracer could not only provide a new method for longitudinal studies and disease monitoring of CRC and other cancers, but also perhaps elucidate the mechanisms of $VO(acac)_2$ compound accumulation in cancer cells. There are currently no methods to synthesize, characterize, or use this radiotracer in the literature.

In this work, such methods are developed. The first objective is to **Produce ^{48}V using a Compact Medical Cyclotron**. Many facilities focused on clinical radiotracer production, such as the IBA 18/9 Cyclone cyclotron used herein, do not have a dedicated solid target system. However, we have modified a simple beamstop to be used as a target holder. Theoretical calculations and Monte Carlo simulations are done to assess the efficacy of this system.

With the irradiated target, the next objective is to **Establish a New Procedure for the Synthesis of $^{48}VO(acac)_2$**. The target is dissolved and the ^{48}V extracted via column separation, chelated as $^{48}VO(acac)_2$, and filtered. Methods are developed iteratively for each step of the process. The compound is characterized and synthesis is confirmed by gamma-ray spectroscopy, high performance liquid chromatography (HPLC), and thin layer chromatography (TLC); a new HPLC method specific to $VO(acac)_2$ was developed for this

work and compound characterization.

Using the synthesized compound, the final objective is to **Conduct *In Vitro* and *In Vivo* Studies to Model the Kinetics of** $^{48}VO(acac)_2$. Cellular and animal PET imaging studies using colorectal cancer cell lines HCA-7 and HCT-116 are done to obtain cell-uptake and time-activity curves. This data is used for kinetic modelling to obtain a value for tumor distribution volume ratio, a metric of how quickly the radiotracer enters and exits the tissue from the blood.

The proposed research will address and tackle these unexplored issues, potentially leading to significant advances in developing a new radiotracer for PET imaging of cancer.

CHAPTER 1

INTRODUCTION

1.1 History of Radiotracer Development

The first use of a radiotracer to study a living system was published in 1923 by George de Hevesy [41]. De Hevesy dipped plants into a solution containing a radioisotope of lead for 1-48 hours, then burned different parts of the plant. By assaying the ash from each part of the plant and comparing it to the radioactivity of the original solution, he could determine where the radioactivity had gone in various time frames. He received the Nobel Prize in chemistry for this work in 1943.

Early studies of radioactivity centered around naturally occurring radioactivity. In 1932, Irene Curie and Frederic Joliot found that bombarding aluminum, boron, and magnesium foils with alpha particles produced substances that continued to emit positrons even after irradiation ceased. They observed that radioactive gases were separated from each target, demonstrating the production of radioisotopes of nitrogen, phosphorus, and silicon [52]. This study was the first to demonstrate the production of artificial radioactivity, for which they received the Nobel prize in chemistry in 1935.

This methodology laid the groundwork for the generation and discovery of several radionuclides. The first biomedical study using artificial radioactivity was published in 1935. By feeding rats bread coated with phosphorus-32-phosphate and assaying organs and excreta, O. Chiewitz and de Hevesy concluded that phosphorus spends approximately two months in the rat body and that there is rapid turnover of phosphorus atoms in bone [22].

The first human physiology experiments using radioactivty were conducted by Joseph Hamilton in 1937 [36]. Patients drank a radioactive salt solution (sodium-24, $t_{1/2}$=16 h, decays via β- decay) [18]. Their hand was assayed to estimate the rate of absorption of sodium into the blood stream, which was found to begin within minutes and reach equilibrium

in 3-10 or more hours, varying per patient. Hamilton, along with co-authors Mayo Soley and Robley Evans, published the first study using iodine-131 (^{131}I) as a diagnostic agent two years later [37]. They observed iodine uptake and washout in patients with normal and diseased thyroids. ^{131}I remains in regular use for detection and treatment of thyroid cancer today.

The 1950's saw a rise of radionuclides for medical use, including the introduction of iodine-132 and technetium-99m radionuclide generators [90] [98]. Louis Sokoloff and Martin Reivich developed carbon-14 (^{14}C) labeled deoxyglucose to study glucose metabolism [54]; however, its utility in humans was limited by the long, 5,700 year half-life of ^{14}C [18]. Fluorine-18 (^{18}F) labeled deoxyglucose (FDG) was developed soon thereafter; ^{18}F was chosen as a substitute due to its lack of prompt gammas, reasonable half-life, stable decay product, and chemical reactivity [5]. These properties made ^{18}F-FDG feasible to use in human patients. Today, 19 PET radiotracers are approved by the FDA for clinical use, utilizing radioisotopes carbon-11 (^{11}C), ^{14}C, copper-64 (^{64}Cu), ^{18}F, gallium-68 (^{68}Ga), nitrogen-13 (^{13}N), and rubidium-82 (^{82}Rb) [45].

1.2 Motivation for Novel Radiotracer Development

Positron Emission Tomography (PET) is a powerful tool for diagnosing and locating abnormalities and monitoring treatment progression in patients. By coupling a positron-emitting radioisotope, such as ^{18}F, ^{11}C, or ^{68}Ga, among others, with a targeting vector, such as glucose, choline, or DOTATATE, the radiotracer is targeted to an area of interest, such as a malignancy. As the radioisotope decays, the emitted positrons can be used to locate the diseased tissues or follow the anomalous process.

With the utility of small medical cyclotrons, it is possible to produce radioisotopes and synthesize radiotracers more specific to certain types of disease onsite at medical facilities. Radiotracers follow the biological function of a vector most closely when the compound

contains a stable atom that has a radioactive isotope. By substituting the radioactive isotope for the stable atom, the compound's integrity is maintained, ensuring that the same biological function is monitored. With a larger variety of radioisotopes, it becomes more likely to find one that matches a given biological vector, allowing abnormal tissues to be better localized and increasing the chances of survivability.

The specific mechanisms of tracer (both radiotracer and non-radioactive compounds) uptake are often not entirely understood: selective uptake varies per cell line and receptor type and density. Additionally, the compound can undergo metabolic changes in the body, further complicating its uptake and retention within a cell. These factors influence not only the quantity of tracer taken up by a cell, but also the speed of uptake and washout. All of these factors lead to variability in diagnostic performance across diseases and risk poor detection of abnormalities in patients.

Kinetic modelling helps decipher these tracer kinetics by recording the activity in individual tissues or organs over time, enabling estimation of rate of uptake, washout, and involvement of key cell components including receptors related to tracer targeting. By quantifying these relevant functional parameters, it is possible to extract important physiological or pathological information: developing a mathematical model captures the relationship between observed data and physiological kinetics [16].

1.3 Objectives of the Current Work

Vanadyl acetylacetonate ($VO(acac)_2$) has been shown to preferentially accumulate in cancer cells [72] [67] [73]. This selectivity over normal tissue could potentially facilitate differentiation of various cancer stages, from inflammation to malignant tumor. While the synthesis of various vanadium-48 (^{48}V) labeled compounds, including vanadyl-pheophorbide, bis(maltolato)oxovanadium(IV), and vanadyl sulfate, has been previously investigated [89] [104] [50], there are currently no methods in the literature for synthesizing ^{48}V-labeled-

$VO(acac)_2$ and no *in vitro* cellular or *in vivo* animal imaging work has been done to understand its tracer kinetics.

One type of cancer where staging information would be advantageous in patient treatment is colorectal cancer (CRC). Ulcerative colitis, or chronic inflammation of the bowel, is increasingly recognized as a component of CRC tumorigenesis [32]. By introducing the positron emitter ^{48}V, PET imaging could not only monitor disease progression, but also provide metabolic information vital to following the disease. Thus, $^{48}VO(acac)_2$ could potentially be used for more accurate staging of CRC, allowing for better monitoring of disease progression and earlier treatment of malignancy.

The specific objectives of this proposed work are:

1. **Produce ^{48}V via a Compact Medical Cyclotron**. In lieu of a solid target system (not available on-site), a beamstop (a device that absorbs excess beam) will be used as a target holder; Monte Carlo simulations will assess the efficacy of this system.

2. **Establish a New Procedure for the Synthesis of $^{48}VO(acac)_2$**. Methods for radiotracer synthesis and characterization will be developed to produce and confirm the compound.

3. **Conduct *In Vitro* and *In Vivo* Studies to Model the Kinetics of $^{48}VO(acac)_2$**. The radiotracer produced herein is used for imaging studies to obtain time-uptake information, which can be used for kinetic modelling.

The proposed research will address and tackle these unexplored issues leading to significant advances in developing a new radiotracer for PET imaging of cancer.

1.4 Innovation of Radiolabeled Vanadyl Acetylacetonate

While several vanadium compounds have been synthesized using cyclotron-produced ^{48}V, $^{48}VO(acac)_2$ has not. This work details the first method established to produce the radiotracer

$^{48}VO(acac)_2$ and the first imaging studies using this radiotracer. Additionally, ^{48}V is usually produced with a solid target system, limiting those facilities that can produce the isotope and excluding most facilities in a typical hospital setting. While a solid target system would be needed for routine production, developing a method to synthesize $^{48}VO(acac)_2$ via cyclotron without a solid target system allows us to explore the feasibility of producing this radioisotope and novel radiotracer. With this compound, studying the uptake of $^{48}VO(acac)_2$ via *in vitro* and *in vivo* studies will aid in developing a kinetic model of the radiotracer physiology, improving the understanding of the uptake of both the radiolabeled and non-radiolabeled compound. Establishing these methods and providing some preliminary results will facilitate future work in this area.

1.5 Organization of Dissertation

This dissertation explores the development, characterization, and use of a novel radiotracer for cancer imaging. The technical concepts that facilitate this work are explained in Chapter 2, including the functionality of PET systems; principles of cyclotron operation; motivation for using ^{48}V and the properties of this radioisotope; and background of research using $VO(acac)_2$ and current gaps in knowledge. Chapter 3 explores the production of ^{48}V via proton irradiation of natural titanium foils, including the description of the beamstop target system and the variable irradiation timelines and geometries that were used. Due to the inexact nature of this system, it is modelled in the Monte Carlo program TOPAS in Chapter 4, which explores factors such as target formation, placement, and geometry in terms of the overall yield produced. The novelty of this radiotracer required the development of characterization methods to confirm that the correct compound was synthesized. The process of developing high performance liquid chromatography methods, as well as a description of the method established, is described in Chapter 5. With these radioisotope generation and chemical characterization procedures established, Chapter 6 details the procedure to synthesize the

radiotracer $^{48}VO(acac)_2$, including alternative approaches attempted, difficulties encountered, and overall yields. The developed radiotracer was used in cellular and animal imaging studies, which are described along with their subsequent results in Chapter 7. This chapter also details interpretation of this imaging data using kinetic modelling, including obtaining parameters for distribution volume ratio to attempt to describe the system. Chapter 8 summarizes the results of this work and details future steps to develop this radiotracer and use it in imaging studies.

CHAPTER 2

BACKGROUND

A radiotracer consists of a radioisotope bound to or incorporated into a biological vector, which can be a compound known to target certain types of receptors or other biomarkers. The radioisotope and vector should be chosen such that the biological half-life (rate of uptake and clearance from the body) and physical half-life (rate of radioactive decay) are compatible. The radioisotope should have a long enough half-life such that it will remain bound to the vector while the physiological process is being observed, but will decay quickly enough so as to not impart excessive dose to the patient. An improperly paired radioisotope and vector combination can lead to excessive decay before sufficiently accumulating in the targeted tissue, failure to observe the physiological process on the imaging time frame, or retention in the body for too long, all of which would affect the quality of the data obtained, the information that can be interpreted from it, and the radiation dose to the subject.

Radiotracers are used to follow the uptake or function of a biological system. The radioactivity is used in "trace" amounts, providing sufficient signal to follow the function without disturbing the system studied. When used for imaging purposes, radiotracers should follow the below principles [20]:

1. The behavior of the radiotracer should be identical to that of the natural substance or differ in a known manner.

2. The mass of the radiotracer should not alter the physiological process studied.

3. The specific activity of the radiotracer should be high enough to fulfill the first two requirements.

4. Any radiation-induced effects should be negligible.

In choosing a radioisotope and vector pair to develop a radiotracer, these guidelines should be adhered to in order to produce a successful imaging tool.

2.1 History and Principles of SPECT and PET Imaging

Positron coincidence detection was first utilized in 1953, when a pair of sodium iodide detectors were used to observe the distribution of an arsenic-74 ($t_{1/2}$=17.8 d, decays via β+ emission [18]) source to find disruptions in the blood-brain barrier caused by a brain tumor [92]. Hal Anger invented the gamma camera in 1958; his methodology was incorporated into the first SPECT (single photon emission computed tomography) system described by David Kuhl in 1963 [48]. SPECT consists of detectors overlaid with metal collimators, allowing only radiation from a certain angle to be accepted while particles from other angles are absorbed in the collimator and rejected. This directional information is used to determine the position of the radiation source. After acquiring this information over many different positions, the data are used to reconstruct the radioactivity distribution and determine the location of the radioactivty within the phantom or body studied.

More collimator positions and higher resolution collimators result in better spatial distribution estimates and higher system sensitivity, respectively, as they are able to more accurately define the origin of the radiation sources. The clinical spatial resolution achievable with SPECT is around 9 mm [87]. The detection principle of SPECT is illustrated in Fig. 2.1A, showing a radioactive source (grey) in a subject (oval) and gamma-rays (arrows) that are either absorbed in the collimator (small rectangles) or allowed to pass through to the detector (large rectangles). This is one type of collimator, thought SPECT imaging employs several types of collimators for different purposes and imaging studies.

Sources used in SPECT (technicium-99m, iodine-123, etc.) decay via emission of gamma-rays, which are detected individually. With only a single photon emitted and no assumed correlation between emitted gamma-rays, SPECT does not utilize any coincidence detection. However, positron emission tomography (PET) radioisotopes decay differently. As PET radioisotopes, including ^{48}V, decay, they emit a positron. The positron travels a short distance (a few mm) through tissue, losing energy to local ionizations, before its energy

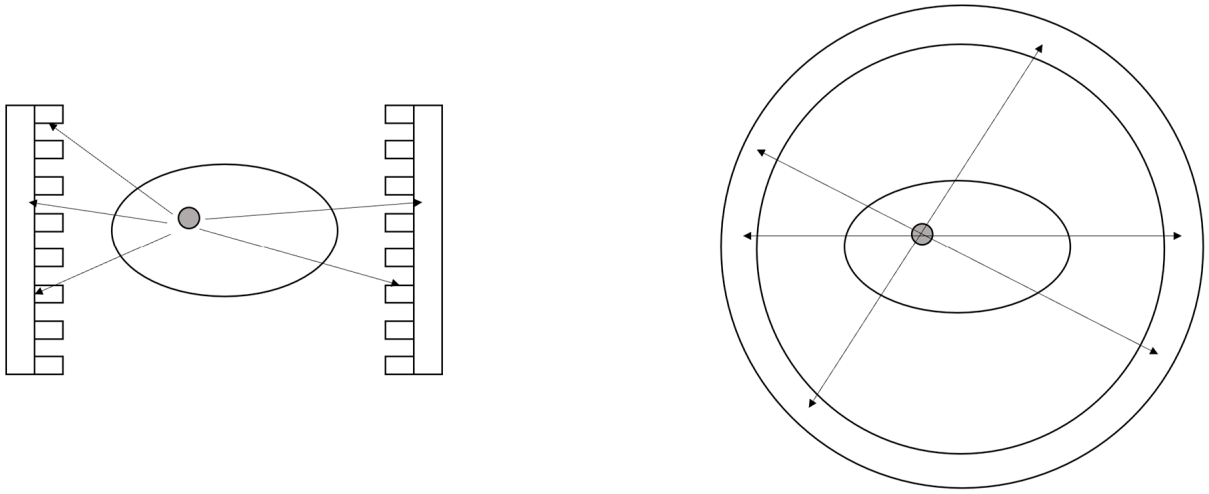

Figure 2.1: Depiction of SPECT imaging (A, left) and PET imaging (B, right) systems. The inner ellipse represents the profile of a patient, and the grey circle within represents a radiation emitting source. Adapted from Cherry et al. 2012.

becomes sufficiently low to interact with a nearby electron. This interaction results in the annihilation of the two particles, producing two 511 keV photons at approximately 180° from each other to conserve momentum [20]. This is depicted in Fig. 2.1B.

PET systems use the 511 keV gamma-rays to determine the location of the radiation, as opposed to the collimators used in SPECT. When x-ray computed tomography (CT) was introduced by Hounsfield [47], David Chesler applied the method to the positron camera by rotating it to record multiple views and back-projecting the data to obtain qualitative tomographic images [21]. The first quantitative imaging system was developed in 1974, consisting of a hexagonal array of NaI detectors protected by shielding. The system was designed to mitigate registration of random and scattered coincident events and minimize deadtime losses from gamma-rays [95]. Measurements of the initial dose and the radioactivity concentration, blood, and tissue allowed the biodistribution of the radiotracer to be quantified. Acquired over time, this data allowed the exchange kinetics of the radiotracer to be modelled to determine the rate of uptake, the retention, and the rate of release, providing insight into

the physiological processes or parameters, such as metabolic rates of the pathway studied. In the years since its initial publication, several improvements have been made to this system, focusing on the addition of CT to provide anatomical information, improvements in the scintillation material of the detector, increasing the solid angle covered by the detection system, and improving the timing resolution [100]. Today, PET systems can achieve a spatial resolution of 4 mm [87].

A typical, modern PET system consists of a ring of scintillation detectors coupled to photomultiplier tubes (PMT). When the 511 keV photons reach the system, they can be detected in two ways: they can undergo Compton scattering, depositing some energy in the scintillator via electron interactions and producing recoil photons; or, they can undergo a photoelectric interaction, producing a photoelectron that subsequently loses energy by interacting with the scintillation material and produces secondary particles. When energy is deposited in the scintillator, optical photons are emitted. The amount of light is proportional to the energy deposited; to quantify it, the scintillator is coupled to PMTs. The PMTs produce an electrical current when stimulated by the light. The front face of the PMT is the photocathode: it is coated with a material that ejects electrons when struck by photons in an appropriate energy range. These photoelectrons are attracted to a positively charged dynode, which emits secondary electrons when struck; the multiplication factor depends on the energy of the photoelectron. The secondary electrons are attracted to a second dynode with higher potential and produce more electrons; this process is repeated several times until the electrons are collected at a downstream anode [20]. This process is shown in Fig. 2.2.

When the energy deposition event is registered in the detector, it is given a time stamp. If two events occur within a coincidence timing window, typically 6-9 ns, then they are thought to be coincident; the interval accounts for differences in signal acquisition and for the photons to potentially traverse different distances and amounts of tissue before reaching the detector. Only coincident events are considered in the determining the spatial origin of the radiation;

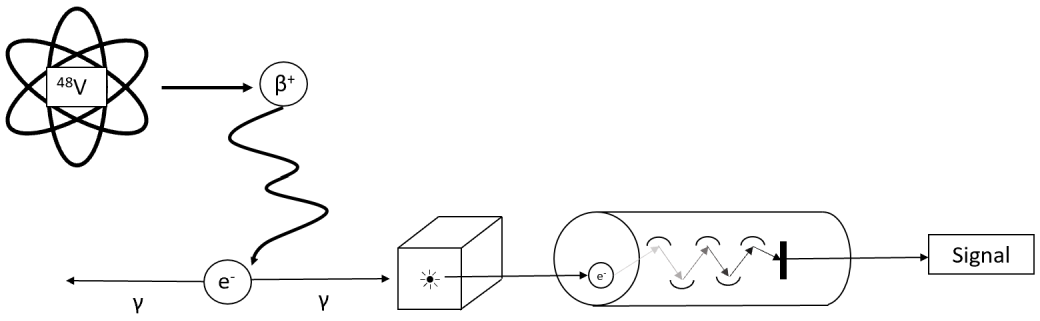

Figure 2.2: Positron emission and detection. The scintillator is represented as the box; the PMT is represented as the cylinder. Adapted from Cherry et al. 2012.

all other events (such as characteristic gamma-rays) without a coincident signal are discarded. In this way, modern PET systems do not require the collimators used in SPECT to determine the point of origin of the radiation, though some PET systems have previously used these mechanisms to reduce random and scatter events.

An annihilation gamma ray pair that makes it to the PET detectors and is detected in coincidence without undergoing a Compton interaction in the tissue is termed a "true" event. However, there are other events that can be detected as coincident that do not originate along the same line of response: "random" and "scatter" events. Random events consist of two annihilation events originating from separate events at different locations that are detected simultaneously; scatter events occur when one or both of the 511 keV photons emitted undergoes a scattering event, changing their direction from the original path before being detected. These events are shown in Fig. 2.3, where the true event originates from the grey sphere, the random event is depicted as originating from the red markers, and the scatter event is depicted as originating from the green marker.

Several factors influence the performance of PET systems: the spatial resolution, the sensitivity, and the noise-equivalent count rate. The radioisotope used most directly influences aspects of the spatial resolution. Some factors of spatial resolution are related to the detection system (detector size, reconstruction method, detector location), while others are specific

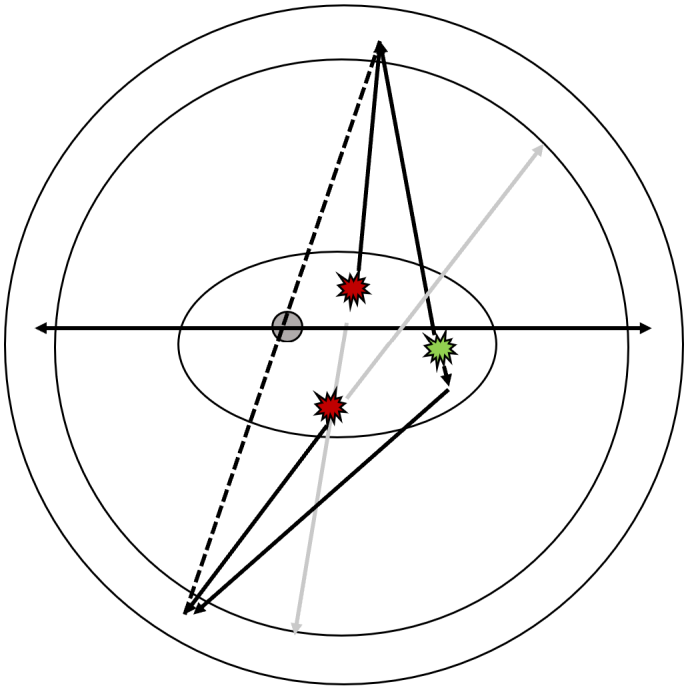

Figure 2.3: Depiction of true, random, and scatter events that can be detected in a PET detector. The event originating from the grey marker shows a "true" event; the event originating from the red markers shows a "random" event; and the event originating from the green marker shows a "scatter" event. The outer annulus represents the PET detector ring.

to the type of radiation used (positron range, noncollinearity). The factors stemming from radioisotope selection are described below.

The energy of the positron dictates how far it will travel from the radioisotope through the tissue before annihilating with an electron and producing photons that can be detected; this distance is known as the positron range. Imaging and reconstruction methods determine the location of the annihilation event, not the position of the original decay; therefore, the positron range introduces uncertainty in the location of the radioisotope. The value of the mean positron range is low for low-energy positrons (0.2 mm for fluorine-18 (^{18}F), 250 keV positron energy) and higher for high-energy positrons (2.6 mm for rubidium-82 (^{82}Rb), 1,481 keV positron energy) [94]. This range is influenced by the type of tissue or material traversed.

While positrons lose most of their energy before the annihilation event, they can still have some residual momentum. This results in a slight deviation from the 180° photon emission;

this effect is known as non-collinearity. Subsequently, the line of response does not lead back exactly to the point of annihilation. The error resulting from non-collinearity increases with increasing ring diameter [85][70].

2.2 History and Overview of Cyclotron Functionality

In 1919, Ernst Rutherford showed that an element could be transformed by artificial means by bombarding nitrogen gas with alpha particles from a radioactive source [83]. However, he recognized that the low number and energy of the alpha particles limited the amount of radioactivity that could be produced; he suggested the need for a device that could produce a large number of energetic particles [87]. Many types of particle accelerators emerged during this time, including the Cockcroft-Walton and Van de Graaf generators, the linear accelerator (though not a machine powerful enough to fulfill Rutherford's request), and the cyclotron.

The first cyclotron was introduced by Ernest O. Lawrence in the 1930's, built on the concepts that charged particles could be manipulated in a magnetic field and accelerated by an increase in voltage [87]. After adjusting the concepts with small prototypes [62] [63], Lawrence created a 27.5" cyclotron using repurposed magnets that was able to accelerate 5 MeV deuterons at a current of 0.3 μA [60]. Today, there are more than 1,300 operating cyclotrons in International Atomic Energy Agency (IAEA) member states with energies upwards of 520 MeV (TRIUMF) and currents as high as 1 mA (the TR-30/15) [3].

There are three principles that guide cyclotron functionality [87]:

1. A charged particle can be accelerated by an electric field
2. A charged particle in a magnetic field perpendicular to its motion will travel in a circular manner
3. The rotational frequency of the charged particle is independent of the radius of its motion

The body of a cyclotron consists of two or more hollow electrodes ("dees") with a gap between them placed between the poles of a strong dipole magnet. An ion source centered in the gap between the dees generates negative ions. A gas of neutral molecules is heated to a plasma, allowing ions to move freely. Slits in the ion source allow particles of the right energy and position to exit and continue on to orbit.

An alternating radiofrequency (RF) voltage is applied to the dees, providing a positive electric potential that accelerates the ions across symmetric gaps which are formed by the potential on the dees and respective grounded electrodes or structures on both sides of them. Within the dees, the ions see no accelerating force but move in a semicircle with a fixed radius according to the magnetic field therein and the ion's velocity. By the time the ions reach the gap again, the RF voltage has alternated the electric potential of the dees, becoming negative, causing the ions to accelerate across the gap again, this time repelling the negative ion. With their additional energy, the particles enter the next dee and have a larger radius of motion. Due to their increase in velocity, the particles traverse the path in the same amount of time as the path of a smaller radius in the previous dee. This mode of cyclotron operation is termed isochronous. The timing of the RF oscillation matches the time it takes for the particle to traverse the dee, known as the cyclotron resonance [87]. This process continues, causing the ion to spiral from the center of the dee outward. A diagram of this process can be seen in Fig. 2.4, where the red marker is the initial position of the ion, the arrows represent the particle motion, and the different colors denote the changing electric field polarity and that its direction has changed since the last acceleration of the particle. This figure uses the classical "D"-shaped dees. Modern machines with pie-shaped dees operate in a similar fashion.

The motion of the ion is dominated by centripetal force and Lorentz force, given by Eqns. 2.1 and 2.2, where m is the mass of the ion, v is the velocity, r is its radius of motion, q is its

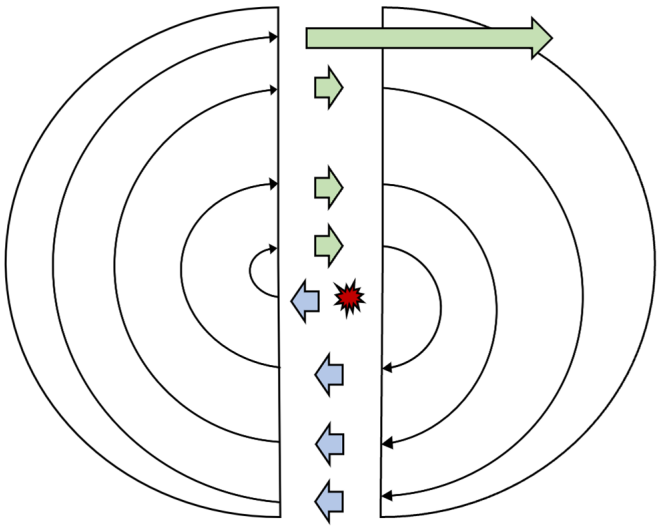

Figure 2.4: Path of motion for an ion in a cyclotron. The ion spirals outwards from the center, accelerating at the gap in the direction of the arrows. The semi-circles represent the dees.

charge, and B is the magnetic field.

$$F_c = \frac{mv^2}{r} \tag{2.1}$$

$$F_B = qv \times B \tag{2.2}$$

By equating these equations, they can be reorganized in the following manner.

$$\begin{aligned} \frac{mv^2}{r} &= qvB \\ \frac{m^2v^2}{r^2} &= q^2B^2 \\ mv^2 &= \frac{q^2B^2R^2}{m} \end{aligned}$$

Introducing the definition of kinetic energy given in Eqn. 2.3, expressions for the velocity

and energy of the particles can be derived.

$$E_k = \frac{1}{2}mv^2 \tag{2.3}$$

$$E_k = \frac{q^2B^2R^2}{2m} \tag{2.4}$$

The angular speed of the rotation and rotational frequency can be defined with Eqns. 2.5 and 2.5.

$$\omega = \frac{v}{r} = \frac{qB}{m} \tag{2.5}$$

$$f = \frac{w}{2\pi} = \frac{qB}{2\pi m} \tag{2.6}$$

In order to be extracted from the cyclotron, the negative ions are stripped of their electrons by traversing a thin, carbon stripper foil, creating a positive ion whose trajectory is opposite to the negative ion and is therefore deflected out of the orbit to a target or to the beamstop, a device that absorbs excess beam.

Targets can consist of liquid, gaseous, or solid material. The purpose of the associated targetry is to get the desired material into the pathway of the beam, keep it in place and intact during irradiation, and enable the material to be quickly removed for further processing [87]. The incident ions can undergo four modes of interaction with the targetry:

1. Inelastic collision with the target's atomic electrons.

2. Inelastic collisions with the nuclei of the target material.

3. Elastic collisions with the nuclei of the target material.

4. Elastic collisions with target's atomic electrons.

As the ion traverses the target, it loses energy to these processes. A large portion of this energy is dissipated as heat. A major challenge in target design is effective cooling. Heating

can cause reduction in target density, chemical reactions in the target material, and damage to the target or targetry. An efficient cooling system can be necessary to prevent target damage and to allow the use of higher currents [2]. Cooling is sometimes supplied by a solid target system, which can also remotely move a target into and out of a beam. However, these systems sometimes require external beamlines or equipment, which can be prohibitively expensive and require additional space that may be hard to accommodate in an existing facility.

The system described is maintained under a vacuum to minimize interactions between the accelerating ions and air particles. Cyclotrons accelerating negative ions (including the IBA Cyclone 18/9 cyclotron used herein) require a higher vacuum on the order of 10^{-7} Torr.

2.3 Properties of Vanadium-48

Vanadium-48 (^{48}V) is a positron-emitter, making it a potential candidate for use in PET imaging. It has a 16 day half-life [18], relatively longer than the half-lives of clinically available PET radioisotopes ^{18}F, ^{11}C, ^{15}O, ^{13}N, ^{64}Cu, ^{68}Ga, and ^{82}Rb, which vary from 1.26 minutes to 13 hours; the half-lives of each are shown in Table 2.1. The relatively short half-lives of these radioisotopes often require that they are produced on-site, distributed within a short distance, or produced via generator, limiting their utility to facilities with either production capabilities or within distribution ranges.

Radioisotope	Half-Life	Average Positron Energy
Fluorine-18	110 min.	250 keV
Carbon-11	20 min.	386 keV
Oxygen-15	2 min.	735 keV
Nitrogen-13	10 min.	492 keV
Copper-64	12.7 h	278 keV
Gallium-68	68 min.	830 keV
Rubidium-82	1.26 min.	1,481 keV

Table 2.1: Half-life and average positron energy of clinically available PET radioisotopes [18]

The half-life also limits the biological functions that can be studied: the labelling vector must be taken up or interact as intended while the radioisotope still has sufficient radioactivity. For example, monoclonal antibodies have slow pharmacokinetics due to their large molecular size; they must be monitored over hours, days, or longer to observe their uptake and therapeutic effects. Therefore, to relate the location of the monoclonal antibodies to any detected radiation, they must be conjugated to a radioisotope that will still emit radiation on this timescale [25]. In some cases, it is useful to monitor a treatment over a long period of time. Recently, zirconium-89 (^{89}Zr, $t_{1/2}$ = 3.3 days) has been used to monitor antibody treatment via PET 30 days post injection [6] and monitor breast cancer treatment [28]. The use of ^{48}V in lieu of ^{89}Zr could allow studies to be conducted over longer periods of time, or potentially yield higher quality images due to the subsequent higher count rate, both because of the longer half-life of ^{48}V. The relatively long half-life of ^{48}V could provide a high degree of flexibility in monitoring slow physiological processes and conducting longitudinal studies, as well as being accessible to many facilities with a central production location due to its slow decay.

^{48}V has an average positron energy of 290 keV [18]; based on this value, it could have comparable positron range to that of ^{18}F and ^{64}Cu and smaller positron range compared to that of radioisotopes ^{11}C, ^{13}N, ^{15}O, ^{68}Ga, and ^{82}Rb, all of which have higher average positron energies ranging from 386-1,481 keV [18]; the average positron energy of each is shown in Table 2.1. The emitted gamma-rays of ^{48}V (984 keV, 1,312 keV, and 2,240 keV, 100%, 98.2%, and 2.3% abundance, respectively) are vastly different from the 511 keV gamma-rays emitted by positron annihilation and are therefore easily discriminated from the window set for collecting the 511 keV photons. These high-energy gamma-rays are also characteristic, making them useful in verification of ^{48}V during the production and radiolabeling processes.

While useful in characterization, these high-energy gamma-rays could introduce additional image blurring or quantification errors due to downscatter and increase random coincident

events. Combined with the long half-life, they could also contribute to significant radiation absorbed doses to the subjects, depending on the biodistribution and biological half-life of the particular radiotracer in use. Although dosimetry calculations are not included in this work, use of this radioisotope in a clinical setting would require estimation of absorbed dose to organs as well as potential additional shielding considerations for the holding and exam rooms.

2.4 Utility of Vanadyl Acetylacetonate

Vanadyl chelates have previously been studied as insulin-mimetics with the potential to lower blood glucose levels in patients with diabetes mellitus [24] [27] [101]. Boden et al. found that patients treated with vanadyl sulfate showed 20% lower fasting glucose concentration and lower hepatic glucose output during high blood insulin levels, both of which were maintained during a subsequent placebo phase [11]. While that study used a different vanadyl compound than the $VO(acac)_2$ used herein, the vanadyl ion (shared by both compounds) is believed to be responsible for the effect: Nakai et al. demonstrated that vanadyl ions are incorporated into adipocytes (cells storing fat) and activate glucose transporters, promoting insulin-like action and suggesting that the vanadyl ion in particular is responsible [74]. Using diabetic and non-diabetic rats, Zhang et al. found similar findings with $VO(acac)_2$ *in vivo*: they concluded that $VO(acac)_2$ lowered plasma glucose levels and could also lower high triglyceride and cholesterol levels [105].

Despite its potential utility, the mechanisms of $VO(acac)_2$ uptake are not well understood. Studies in the 1990's, when $VO(acac)_2$ was considered to treat diabetes mellitus [11], could not establish whether the vanadyl chelates of interest accumulated in the cell or remained membrane-bound to induce their effects and the mechanism that provides the effect. Pandey et al. concluded that vanadyl sulfate, VS, enhances insulin receptor substrate-1 (IRS-1) phosphorylation but could not verify the mechanism behind it [77]. Phosphorylation of IRS-1

influences activation of phosphatidylinositol 3-kinase (PI3-K), which is an effector pathway of RAS (a family of genes) that regulates cell growth, cycle entry, survival, cytoskeleton reorganization, and metabolism. PI3-K is required for the stimulation of the ras/MAPK (mitogen-activated protein kinase) pathway, which helps regulate cell cycle, proliferation, growth, and death. Pandey et al. also found that VS activated ribosomal protein kinase p70s6k, involved in protein biosynthesis, and suggested it may also be regulated by PI3-K [77] [17]. Elberg et al. suggest that the effects of vanadium are mediated via protein tyrosine kinases (PTK), which are enzymes that carry out tyrosine phosphorylation. They hypothesize an intracellular vanadium pool that modulates cytosolic PTK (CytPTK) activity. Further, they conclude that this affect is dependent on the oxidation state of the vanadium – they observe that vanadate (oxidation state 5+) stimulates CytPTK and that the vanadyl (oxidation state 4+) has this effect when oxidized to vanadate via exposure to hydrogen peroxide in neutral pH, which can be generated *in situ* via various biological functions [31]. Among these papers, and several others, hypotheses have suggested how vanadyl chelates exert their insulin-mimetic effects, but do not draw a definitive conclusion, leaving many uncertainties about the mechanisms at work.

More recent studies have shed some light on the physiology of $VO(acac)_2$. Mustafi et al. observed passive diffusion of vanadium compounds across the lipid membrane into the intracellular space in red blood cells and Caco-2 colorectal cancer cells [71]. In a later paper, Mustafi et al. confirmed that $VO(acac)_2$ accumulates in the intracellular space: using ultra-high resolution x-ray fluorescence microscopy (XFM) with 0.3 micron resolution, they acquired images of colonic adenomas of tumor-bearing mice, comparing the distributions of phosphorus, vanadium, and sulfur; the phosphorous distribution was used to define the position of individual cell nuclei and the sulfur is associated with macromolecules in the cytoplasm [73]. They found that the vanadium accumulation did not overlap strongly with the phosphorus, but did overlap with the intracellular sulfur, indicating that the vanadium

remains in the intracellular space. Using x-ray absorption near edge structure (XANES), they showed that the accumulated vanadium remains in the 4+ oxidation state; in contrast, Elberg et al. had hypothesized that vanadyl (4+) was effective once reduced to vanadate (5+) [31].

The glucose metabolism pathway is of particular interest because of a certain class of cells that use large amounts of glucose, including cancer cells. Malignant cells show a high rate of glucose uptake and consumption [1]. *In vitro* studies by Mustafi et al. suggest that vanadium chelates, such as $VO(acac)_2$, are drawn to malignant cells due to their increased rate of glycolysis [71]. They found that colon cancer cells activated key mediators in glycolysis following uptake of vanadyl chelates; they subsequently draw the conclusion that the vanadyl was internalized into the cell.

This preferential uptake was exhibited *in vivo* as well: Mustafi et al. showed that $VO(acac)_2$ accumulated in xenograft prostate cancer tumors during MRI image acquisition over 3.5 hours, while levels of $VO(acac)_2$ in normal tissue after 20 minutes were determined to be negligible, leading to a two-fold intensity in signal from the cancer cells [72]. They argue that this difference in signal intensity is initially due to the presence of $VO(acac)_2$ in the blood in the time immediately after injection due to the vascular density of growing tumors; over the duration of the scan, the malignant tissues accumulate $VO(acac)_2$ due to the high rate of glycolysis associated with cancer cells, leading to enhanced uptake and larger signal intensity associated with the tumor. Similarly, a study using mice with colitis-induced colorectal tumors showed preferential accumulation of $VO(acac)_2$ *ex vivo* via x-ray fluorescence [73]. Compared to normal tissue, they found the concentration of vanadyl chelates to be twice as high in cancerous tissues; compared to normal colon, they also found intracellular hotspots to have a 6-fold concentration of vanadyl chelates.

These studies [72] [73] indicate that $VO(acac)_2$ could be used to differentiate cancerous tissues from normal, non-malignant tissues. In malignancies where inflammation is a precursor,

this selectivity could potentially aid cancer staging, enabling earlier detection of disease. Ulcerative colitis, a chronic inflammation of the bowel, is increasingly recognized as a component of colorectal cancer tumorigenesis [32]. Thus, $VO(acac)_2$ could potentially be used to identify when the tissue crosses the threshold from inflamed to malignant. In facilitating this differentiation, $VO(acac)_2$ could enable more accurate identification of colorectal cancer, allowing for better monitoring of disease progression and earlier treatment of malignancy. By labeling the compound to radioisotope ^{48}V, $^{48}VO(acac)_2$ has the potential to provide metabolic uptake information not easily accessible in other modalities, facilitating better understanding of disease and its progression.

CHAPTER 3

PRODUCTION OF VANADIUM-48 VIA BEAMSTOP HOLDER

3.1 Introduction

While not previously used clinically, vanadium-48 (^{48}V) has several prior applications and uses in medicine. Vanadium-48 has been investigated for use as a transmission source in PET scans in lieu of ^{68}Ge as a more cost-efficient alternative [42]. The natural titanium (^{nat}Ti) rod could be irradiated to form ^{48}V via the ^{48}Ti(p,n)^{48}V reaction, used, and then re-irradiated and re-used: ^{48}V decays to ^{48}Ti. In some foil stack experiments, the ^{48}Ti(p,n)^{48}V reaction has also been used as a monitor reaction [34]. Foil stack experiments use thin monitor foils to determine the beam flux and incident energy based on the activity generated therein via a known, well-defined excitation function. The flux and energy can then be extrapolated for subsequent foils of interest or targets of different materials [39]. The use of the ^{48}Ti(p,n)^{48}V reaction as a monitor reaction indicates that the cross section is fairly well-established and reliably consistent.

Vanadium-48 is often produced with natural titanium foils. Routes of production include: ^{nat}Ti(p,xn)^{48}V, ^{nat}Ti(d,xn)^{48}V, and ^{nat}Ti(α,x)^{48}V. The viable energy range for these reactions is 13-20 MeV; therefore, ^{48}V can be produced by a compact medical cyclotron [19] [58]. In addition to producing ^{48}V, several radionuclides are co-produced in these reactions. Natural titanium foils have been used to produce scandium radioisotopes ^{43}Sc and ^{44}Sc [58]; other co-produced radionuclides include ^{45}Ti, ^{47}V, ^{46}Sc, and ^{47}Sc.

Typically, solid targets are irradiated using a solid target system. Such a system cools the target, dissipating the heat generated during irradiation and allowing thicker targets to be used [35]. After irradiation, such a system could deposit the target in a lead shielding container, facilitating the handling of higher levels of radioactivity while mitigating the radiation dose to personnel. Some solid target systems are also able to be remotely mounted

and dismounted and even pneumatically transported from the vault housing the cyclotron to a hot cell where the chemistry is performed, thus removing manual handling altogether. A solid target system could also help ensure the target is uniformly irradiated by securing the target in place, preventing the target from rotating or otherwise moving during the irradiation.

The University of Chicago (UC) Cyclotron Facility does not have a solid target system. However, it does have an accessible beamstop, an aluminum port where excess beam is typically directed for testing purposes; a cross sectional view of the beamstop is shown in Fig. 3.1. Target materials can be molded into an appropriately-sized shape and placed in the

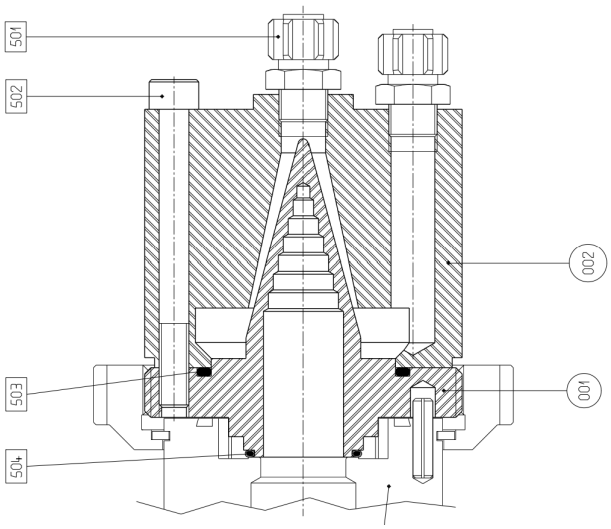

Figure 3.1: Cross sectional view of the beamstop depiction, courtesy of IBA. The beamstop is an aluminum port where excess beam is directed.

beamstop for irradiation. The beamstop is water-cooled, meaning that while it can cool the target to some degree, it cannot dissipate a large amount of heat in the manner a regular solid target system could. Additionally, the target must be manually loaded and extracted by hand.

In this chapter, methods are proposed to irradiate natural titanium foils in the beamstop of the cyclotron at the UC Cyclotron Facility. Two different target geometries are utilized in order to assess how yield can be maximized. To determine the efficacy of this beamstop target

system, theoretical yields are calculated to compare the assayed activity to the expected yield.

3.2 Methods of Target Irradiation and Yield Estimation

3.2.1 Experimental Irradiation

Thin, natural titanium foils (Grade 1 - ASTM B265, Goodfellow) of 99.6% purity and 12 μm (for targets 1-12) or 12.5 μm (targets 13-15) thickness were purchased from Goodfellow Cambridge, Ltd. (Huntington, England). Foils measured 25 mm x 25 mm or had a 25 mm diameter. The targets were placed in the beamstop of the IBA CYCLONE 18/9 cyclotron at the UC Cyclotron Facility as shown in Fig. 3.2. The beamstop is a simple water-cooled

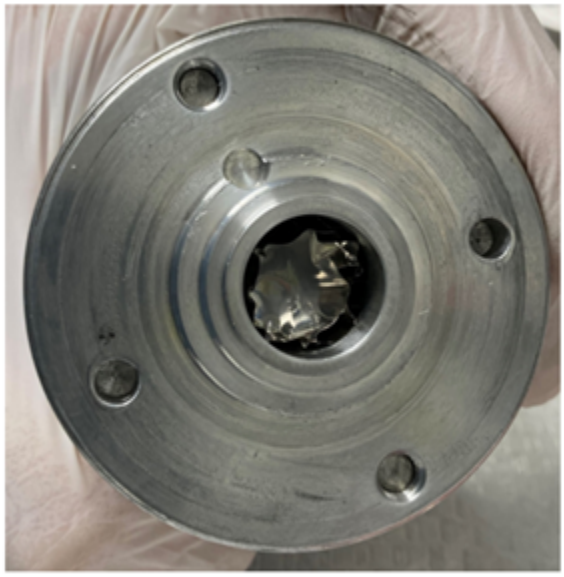

Figure 3.2: Foils placed in the beamstop for proton irradiation.

aluminum block with an internal cavity in the shape of a cone (see Fig. 3.1). A proton beam energy of 18 MeV was used to bombard the natural titanium target in the reaction ^{nat}Ti(p,n)^{48}V. In preliminary analyses, several currents (10, 20, 40 μA) were attempted to observe the effect of current on target material (such as whether the current scorched or

melted the target) and yield. No scorching was observed during these irradiations, so a 40 μA current (the maximum current assessed) was determined to be a balanced choice between current and heat dissipation.

Targets irradiated more than 10 hours were irradiated over multiple days with each session lasting for approximately 8 hours per day. If irradiated for more than 40 hours, targets were irradiated for five consecutive days and left to cool for a two-to-three-day weekend period. For all targets, the target was left in the beamstop holder after the last bombardment and allowed to decay over 2-3 days. This enabled the decay of short-lived radionuclide by-products. After the decay period, the beamstop was removed, and the target extracted and assayed via dose calibrator ion chamber (Capintec CRC-7 or CRC-15W, calibration constant 569) to measure the starting radioactivity for the synthesis.

3.2.2 Target Geometries

Foils were molded into two geometries to form the target: a cup or a sphere. To form the cup, the foil(s) were placed on top of a die press (shown in Fig. 3.3) and the sides folded down to form a cup, also shown in Fig. 3.3. The base of the die press was approximately

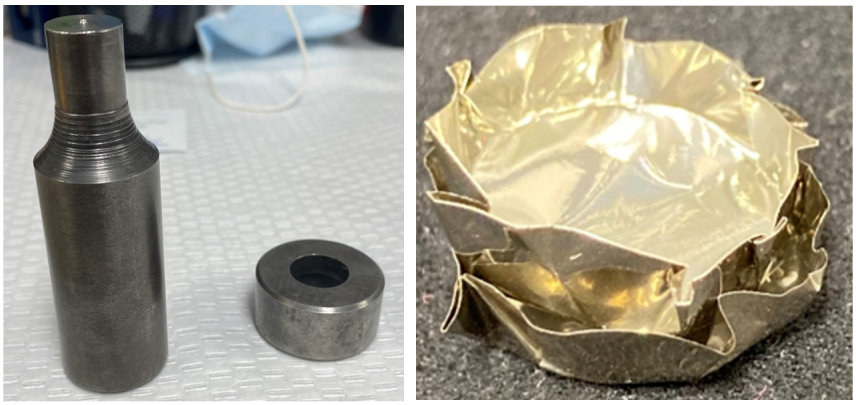

Figure 3.3: Left: Die press used to form the target. Foils were placed on top of the base (left side of left image) and the circular press (right side of left image) was placed on top of it to fold the sides down. Right: Cup shaped foils formed by the press.

17 mm wide, meaning that each side was approximately 4 mm high. Some targets used one

foil (targets 1-8, 14), while others (targets 9-13,15) used two. For some targets, foils were placed on top of each other to form the cup. For target 14, a foil was cut into two rectangular pieces and stacked on top of each other to form the cup; for the inner piece, the sides were approximately 4 mm on two sides and 0 mm on two sides.

To form the sphere, the foils were compressed together until they formed a compact sphere shape. The diameter of the sphere was not measured, but is estimated to be between 8 mm and 14 mm. The motivation for this geometry was to increase the effective thickness of the target, increasing the yield.

3.2.3 Calibration Methods

Gamma-ray spectroscopy was performed using a Captus 3000 Capintec 2" NaI(Tl) probe based well counter. ^{137}Cs was used to calibrate the spectrometer and calculate the energy resolution (full-width at half-max, FWHM), which was determined to be 7.0%. Linearity was corrected using a ^{152}Eu source. The efficiency of the system was calculated to be 3.5% at 662 keV. The ^{48}V foil was positioned perpendicular to the NaI(Tl) crystal and the distance was varied to maintain a dead time of 1% or less. Data were acquired from 2 to 10 minutes to collect sufficient statistics.

3.2.4 Theoretical Estimation

The estimated production yields of ^{48}V and several anticipated co-produced radionuclides ($^{47,48}V$, $^{43,44m,44g,46,47}Sc$, and ^{45}Ti) were determined using Eqn. 3.1 [58], in which N is the number of atomic nuclei per cm^3 in the material; σ is the cross section of the material in cm^2; ϕ is the particle flux across the area of beam incidence; λ is the decay constant; t_1 is the time irradiated; and t_2 is the time of decay.

$$A(t_2) = N\sigma\phi[1 - e^{(-\lambda t_1)}]e^{(-\lambda t_2)} \tag{3.1}$$

Yield estimates assumed a target comprised of a flat, natural titanium foil with thickness equivalent to two stacked foils (24 or 25 μm). The target was assumed to be thin enough that the average incident proton energy did not change significantly in traversing the target, and, therefore, the cross section was assumed to be constant. It is also assumed that the target area is irradiated evenly by the beam. Anticipated reactions are shown in Table 3.1; only those with a cross section larger than 1 mB are included in the yield estimation. The cross

Natural Titanium Isotopes	Abundance	Reaction	Product Half-Life	Decay Product
^{46}Ti	8%	^{46}Ti(p,α)^{43}Sc	3.9 h.	^{43}Ca (stable)
		^{46}Ti(p,γ)^{47}V	32.6 m.	^{47}Ti (stable)
		^{46}Ti(p,n)^{46g}V	422.5 ms.	^{46}Ti (stable)
		^{46}Ti(p,d)^{45}Ti	3.1 h.	^{45}Sc (stable)
^{47}Ti	7.3%	^{47}Ti(p,α)^{44m}Sc	58.6 h.	^{44}Ca (stable)
		^{47}Ti(p,n) ^{47}V	32.6 m.	^{47}Ti (stable)
		^{47}Ti(p,γ)^{48}V	16.0 d.	^{48}Ti (stable)
^{48}Ti	73.8%	^{48}Ti(p,2n)^{47}V	32.6 m.	^{47}Ti (stable)
		^{48}Ti(p,γ) ^{49}V	330 d.	^{49}Ti (stable)
		^{48}Ti(p,n)^{48}V	16.0 d.	^{48}Ti (stable)
^{49}Ti	5.5%	^{49}Ti(p,2n)^{48}V	16.0 d.	^{48}Ti (stable)
		^{49}Ti(p,α)$^{46m+g}$Sc	83.8 d.	^{46}Ti (stable)
		^{49}Ti(p,γ) ^{50}V	2x10^{1}7 y.	-
		^{49}Ti(p,n) ^{49}V	330 d.	^{49}Ti (stable)
^{50}Ti	5.4%	^{50}Ti(p,α)^{47}Sc	3.3 d.	^{47}Ti (stable)
		^{50}Ti(p,γ)^{51}V	Stable	-
		^{50}Ti(p,n)^{50}V	2x10^{1}7 y.	-

Table 3.1: Expected products of target bombardment. Listed are the isotopes of natural titanium; the percent abundance of each; the possible reactions of irradiating that isotope with 18 MeV protons and the resulting product; the half-life of the produced isotope; and the stable decay product. [18]

sections for these reactions were observed from the IAEA recommended data where applicable and Cervenak and Lebeda 2020 otherwise [19] [40]. Yield estimates were not included for the sphere geometry due to the inexact and inhomogeneous nature of the target.

3.3 Results

3.3.1 Experimental Yields

The radioactivity produced for each target irradiation is shown in Table 3.2. The early runs

Sample Number	Geometry	Time Irradiated	Current	Integrated Current	Radiation Yield	Theoretical Yield
1	Cup	0.5 hours	10 μA	5 μA-h	64 μCi	-
2	Cup	1 hour	10 μA	10 μA-h	81 μCi	-
3	Cup	1 hour	10 μA	10 μA-h	102 μCi	-
4	Cup	1 hour	20 μA	20 μA-h	171 μCi	-
5	Cup	4 hours	20 μA	80 μA-h	430 μCi	-
6	Cup	20 hours	20 μA	400 μA-h	1.1 mCi	-
7	Cup	10 hours	40 μA	400 μA-h	2.0 mCi	-
8	Cup	24 hours	40 μA	960 μA-h	8.5 mCi	-
9	Sphere	33.2 hours	40 μA	1330 μA-h	17.5 mCi	-
10	Sphere	65.3 hours	40 μA	2610 μA-h	34.8 mCi	-
11	Sphere	72.3 hours	40 μA	2890 μA-h	31.6 mCi	-
12	Cup	37.3 hours	40 μA	1492 μA-h	6.5 mCi	7.2 mCi
13	Cup	40.5 hours	40 μA	1620 μA-h	8.6 mCi	8.2 mCi
14	Cup	41.6 hours	40 μA	1664 μA-h	4.6 mCi	8.5 mCi
15	Cup	39.7 hours	40 μA	1586 μA-h	7.4 mCi	8.2 mCi

Table 3.2: Irradiation conditions for each bombardment. Shown are (from left) iteration number, target geometry, time irradiated, current, integrated current (the product of time irradiated and current), radiation yield, and theoretical calculated yield.

were considered preliminary and thus, the timeline of their irradiation and time between end of bombardment (EOB) and assay is unknown. The time between EOB and assay is known for targets 11-15, however. An example target irradiation schema, showing the exact times of proton bombardment and resulting yield, both assayed and decay corrected, is shown in Table 3.3 for target 14. The activity yield normalized to the integrated current is shown in Fig. 3.4; the activity in Fig. 3.4A is that at time of assay, not decay-corrected, while Fig. 3.4B shows the normalized activity using activity decay corrected to the EOB; only cup-shaped targets with known EOB-assay time are included.

While the targets in Fig. 3.4A did not have the same decay time between EOB and assay,

Day	Start Beam	End Beam	Current	Time irradiated [h]
Day 1	9:25	21:31	40 μA	12.1
Day 2	9:28	21:28	40 μA	12.0
Day 3	9:09	21:10	40 μA	12.0
Day 4	9:28	15:00	40 μA	5.5
Theoretical Activity at EOB: Est. 107.6 mCi Assayed activity: 4.6 mCi, 13:09 on Day 7				

Table 3.3: Timetable of irradiation of target 14, a 'cup' irradiated for a cumulative time of 41.65 h. The integrated current was thus 1667 μA-hr. The theoretical activity at EOB and the assayed activity 3 days post irradiation are shown in the bottom two rows of the table.

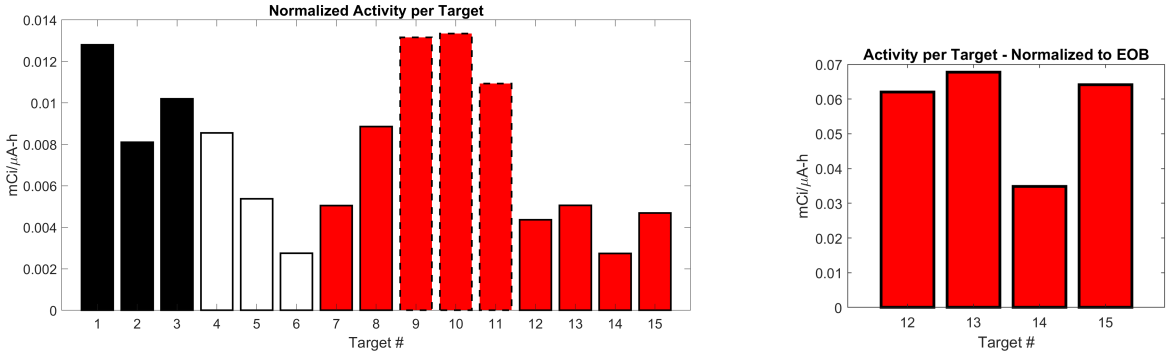

Figure 3.4: Left, A: Radioactivity yield from each target irradiation, normalized to the current and time irradiated. The black bars show targets irradiated at 10 μA; white shows 20 μA; and red shows 40 μA. The dotted line denotes a sphere target, while the solid lines denote a cup-shaped target. Right, B: Normalized activity of targets 12-15, decay corrected to EOB.

the low activity targets decayed for at least several hours, and higher activity targets for several days. The spheres tended to have a higher normalized activity, as did most targets with the 40 μA current. However, without the time between EOB and assay, a relationship between current and yield cannot be drawn.

Fig. 3.4B shows the decay corrected normalized activity. The average value was 0.057$\pm$0.015 mCi/μA-h; the standard deviation is 26% of the mean value (referred to as the coeffecient of variation). If target 14 is excluded (due to irregularities in target formation), the average normalized activity becomes 0.065$\pm$0.003 mCi/μA-h and the standard deviation is only 5% of the mean. This indicates that targets 12, 13 and 15 are in relatively good

agreement despite the irregularities of the beamstop target system.

3.3.2 Gamma-Ray Spectroscopy

The resulting gamma-ray spectroscopy from target 12 is shown in Fig. 3.5. This spectrum

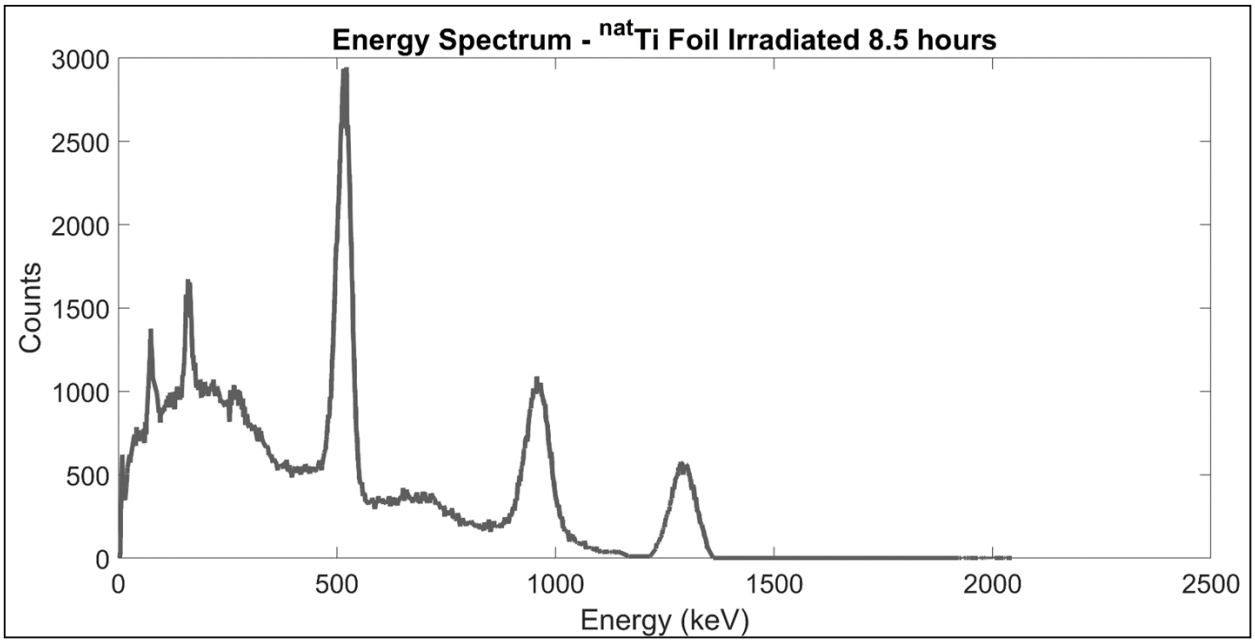

Figure 3.5: Gamma-ray spectrum of ^{nat}Ti foil irradiated 8 hours; 2 days post irradiation (target 12). Peaks correspond to the 511 keV positron annihilation peak, the 984 keV characteristic gamma-ray peak, and the 1,312 keV characteristic gamma-ray peak associated with ^{48}V. The low energy x-rays are likely backscatter due to the lead shielding of the detector [96].

was acquired after 8 hours of irradiation and 2 days of decay. The photopeaks correspond to the expected energies for ^{48}V: the position emission peak of 511 keV (first peak) and two characteristic gamma emission peaks of 984 keV (second peak) and 1,312 keV (third peak), respectively. Partially because of the limitations of the NaI(Tl) well counter available for this gamma-ray spectroscopy measurement, the third gamma peak of ^{48}V at 2,240 keV (only 2.3%) could not be observed. Some expected contaminants are shown in Table 3.1 and Table 3.4 for this compound. The potential contaminants include ^{44}Sc (271, 1,157 keV), ^{47}Sc (159 keV), and ^{46}Sc (889, 1,121 keV); none are visible, either through absence of a photopeak or

due to a photopeak in a similar energy region, and through absence of any apparent additive peaks. The low energy x-rays seen in Fig. 3.5 are backscatter of the γ-rays due to the lead shielding of the detector [18].

Isotope	^{48}V	^{47}Sc	^{44m}Sc	^{44g}Sc	^{43}Sc	^{45}Ti	^{47}V	^{46}Sc	Activity [mCi]
T.12 EOB	6.24%	0.47%	0.20%	2.48%	2.38%	10.23%	77.94%	0.04%	101.62
Assay	85.84%	5.71%	2.31%	1.52%	1.37%	2.53%	0.00%	0.60%	7.15
T.13 EOB	8.13%	0.82%	0.37%	2.55%	2.44%	10.30%	75.32%	0.05%	109.55
Assay	92.53%	5.08%	1.69%	0.00%	0.00%	0.00%	0.00%	0.63%	8.18
T.14 EOB	8.15%	0.86%	0.39%	2.33%	2.23%	9.34%	76.63%	0.05%	107.59
Assay	91.16%	5.99%	2.16%	0.00%	0.00%	0.00%	0.00%	0.60%	8.47
T.15 EOB	7.67%	0.82%	0.37%	2.59%	2.47%	10.32%	75.70%	0.05%	109.00
Assay	90.83%	6.20%	2.28%	0.00%	0.00%	0.00%	0.00%	0.59%	8.18

Table 3.4: Percent of the activity attributed to each isotope present at EOB and at the time of assay; the total (theoretical) radioactivity due to all isotopes listed is shown in the far right column.

3.3.3 Theoretical Yields

For the last four targets, the timeline of irradiation and time between EOB and assay are known; therefore, the theoretical yield can be calculated for these targets. While the timeline of target 11 was known, it was a sphere and therefore did not have uniform thickness, making a theoretical yield difficult to calculate for this geometry. Table 3.4 shows the total theoretical activity at EOB and at assay for these targets, as well as the fraction of each radioactivity assay that can be attributed to various isotopes. At EOB, the dominant radioisotope is ^{47}V for each target, followed by ^{45}Ti. Table 3.1 shows that these radioisotopes have half-lives of 33 minutes and 3 hours, respectively, meaning that both completely decay within 3 days. Additionally, ^{43}Sc and ^{44m}Sc completely decay with 3.33 days. For targets 13-15, the time decayed after EOB was long enough (90, 70, and 65 hours, respectively) that the fraction of these isotopes was negligible at the time of assay. However, target 12 only decayed 18 hours, so these radioisotopes were likely still present at the time of assay. As time progresses,

only the longer-lived radioisotopes ($^{46g,47}Sc$, ^{48}V) remain, making ^{48}V the predominate radioisotope present. However, it is not the longest lived radioisotope (^{46}Sc has a half-life of 2011 h., compared to 383 h. for ^{48}V), so the co-produced radionuclides will not disappear with time alone and further chemical separations are needed.

Comparing the measured and theoretical radioactivity yields, target 13 had the lowest error: the theoretical yield was calculated based on Eqn. 3.1 to be 8.2 mCi, an error of 5% compared to the actual measured yield of 8.6 mCi. Targets 12 and 15 had comparable discrepancies (9% each) between the measured and estimated yield; target 14 had the largest error of the "cup" geometry targets, with a 46% difference between the assayed (4.6 mCi) and estimated (8.5 mCi) yield; possible explanations of this error are described in more detail in Section 3.4. In general, differences between theoretical and measured yield could be attributed to several factors, including challenges in consistent and reproducible target preparation, placement, and orientation.

3.4 Discussion

This chapter describes a methodology to produce ^{48}V without a dedicated solid target system. While used only at the UC Cyclotron facility herein, these methods could be applied to any cyclotron facility with access to a similarly shaped beamstop. A true solid target system would undoubtedly increase yields but are expensive and can be difficult to justify without studies confirming the feasibility of ^{48}V production. The outlined methods could show feasibility and allow for investigations to occur for sites that are interested in producing ^{48}V. Eventually, development of a true solid target system at facilities could potentially increase the number of ^{48}V producers by making it more accessible and therefore, potentially encourage research and use of compounds associated with this radioisotope or any co-produced radionuclides.

Two target geometries were considered - a cup and a sphere - with either one or two foils. Both could be made easily out of 12-12.5 μm thick natural titanium foils. In general, the

spheres produced more radioactivity, though they also tended to be irradiated for longer periods of time. It is difficult to determine a trend without knowing the irradiation timeline and time between EOB and assay, though Fig. 3.4 indicates that the spheres tended to have higher yields. In comparing target 9 (33 h. irradiation) to targets 12-15 (37-42 h. irradiation), the sphere target produced approximately twice as much radioactivity. This is likely because the sphere targets are smaller and thicker, so a larger portion of the target is more likely to intercept the beam. Additionally, the beam loses more energy traversing a thick target. The cross section of the ^{48}Ti(p,n)^{48}V reaction increases with decreasing energy from the 18 MeV used until approximately 12 MeV [19], so the more the average beam energy decreases, the more likely the beam is to interact with the target and form ^{48}V ions.

However, the sphere geometry has significant drawbacks in the radiotracer synthesis, to be discussed further in Chapter 6. For this reason, the cup geometry was determined to be more efficient for irradiations 12-15. Two foils (or thickness equivalent thereof) were used for these targets in an attempt to increase the effective thickness. In general, it can be expected that increasing the thickness of the target will increase the yield, not only due to the increased amount of material but also the effect of lowering the energy and increasing the cross section. Thicker targets would also require more effective cooling compared to thin targets. The energy lost in two stacked 12.5 μm-thick foils would be approximately 2.3 MeV, resulting in an 92 watt heat deposition; in contrast, an 8 mm diameter target would absorb the beam entirely, resulting in a 720 watt heat deposition. This increase in heat deposition could result in scorching or melting the foils, making them harder to process chemically in later steps.

While the ideal irradiation timeline takes place over 5 days, only three targets actually followed this scheme: targets 13-15. Target 11 was irradiated over 16 days and target 12 was irradiated over 8 days. The larger durations could contribute to more variability in the actual fraction of ^{48}V. Of the targets irradiated for similar times, most had similar normalized activity, resulting in an average of 0.065$\pm$0.003 mCi/μA-h and a standard deviation of 5% of

the mean.

Compared to the theoretical yield, the experimental yield of target 12 was 10% lower than expected, the experimental yield of target 13 was 5% higher than expected, the experimental yield of target 14 was 46% lower than expected, and the experimental yield of target 15 was 9% lower than expected. This is partially due to irregularities in the irradiation conditions. In addition to the elongated timeline, the irradiation for target 12 also encountered some problems with the stripper foil, which would decrease the amount of beam on target and result in lower yield. For target 14, there was some variability in geometry: in lieu of using two foils, one foil was cut in half and the two halves were overlaid and pressed into the target. Therefore, the effective thickness on the side of the target in some places was 12.5 μm, not 25 μm. This variability would lead to producing lower activity than anticipated, perhaps explaining the large difference between the experimental and theoretical activities for this target. Target 15 had visible scorching and one of the two foils was partially destroyed and could not be retrieved, indicating some loss of activity. However, it is unclear if portions of the lost foil were fused onto the retrieved foil; the activity of the foil was higher than what would be expected for one foil alone.

3.5 Conclusion

This chapter demonstrated the feasibility of using a beamstop as a target holder for thin natural titanium foils in order to produce ^{48}V. While not an ideal setup, this methodology opens the field of potential users by providing a mechanism to create ^{48}V or co-produced radionculides without solid targetry, which may not be a feasible addition to some facilities. A cup geometry was determined to be optimal, due to a sufficient level of activity produced and implications in the chemical synthesis, to be addressed in Chapter 6. An ideal timeline for irradiation maximizes the time of beam-on-target over as few days as possible, while allowing a period post irradiation for short-lived isotopes to decay. While not part of this

work, depending on the cyclotron and its set-up, these long irradiations could be accomplished while operating the accelerator in "dual-beam" mode (assuming that the machine supports this functionality) so that production of other isotopes is not impacted adversely by long irradiations to produce ^{48}V. Ultimately, this process creates a target that is >85% ^{48}V in terms of radioactivity.

CHAPTER 4

SIMULATION OF BEAMSTOP TARGET HOLDER VIA TOPAS

4.1 Introduction

The previous chapter details how natural titanium targets were irradiated experimentally, including a description of the beamstop target holder used for target irradiation at the University of Chicago (UC) Cyclotron Facility. However, this system was far from ideal; solid targets are typically irradiated via a solid target system that controls factors including target cooling, beam distribution, and target handling. Due to the inexact nature of the irradiation using the beamstop target holder, several components could affect the overall yield, including: target placement in the beamstop, which could introduce an angle altering the effective thickness; beam distribution, which could affect the yield of the target; and target formation, which could affect the amount of material interacting with the beam. In order to limit exposure to those handling these targets and plan for subsequent experiments using the target, it would be beneficial to estimate the radioactivity yield and observe how the aforementioned factors could affect the amount of radioactivity produced. Estimating these target and irradiation irregularities and their impact could also facilitate improvements in the beamstop target system and overall yields.

In this chapter, the irradiation of natural titanium foils is simulated via TOPAS, the TOol for PArticle Simulation, a Geant4-based Monte Carlo program [80]. The simulated yields in TOPAS are compared to theoretical yields calculated using the accepted cross section data for this reaction [19] [40] [61]. These values are compared to the experimental yields of 12 or 12.5 μm-thick foil-based targets bombarded in the beamstop with 18 MeV protons at the UC Cyclotron Facility. Simulations will also seek to shed light on several beam characteristics, including the beam spot size, which are not currently known for this particular cyclotron.

TOPAS is a Geant4-based Monte Carlo program. It was originally developed for proton

and heavy ion simulations but has expanded to include all types of particles simulated in Geant4. This program operates as a 'wrapper' for Geant4 – it has similar or the same functionalities but presents a user-friendly platform. While Geant4 runs on files compiled in $C++$, TOPAS runs on text files, making the program accessible to users with various levels of coding experience. TOPAS was used here due to this accessibility and nesting file structure; simulations are run by executing a text file containing relevant TOPAS commands and a given text file can also call other text files.

The goal of these simulations was to simulate the cyclotron beam and targets irradiated experimentally, including a cup-shaped target and a sphere-shaped target, as described in detail in Section 3.2.2. The parameters for the 'beam' simulations are described in Section 4.2.1; the targets simulated are described in Section 4.2.3. Utilizing the nesting file structure in TOPAS, the same simulation can be run with different parameters or objects substituted in nested files; here, a "cyclotron" file is run that calls a "target" file. This structure makes it easy for users to share files; the "cyclotron" file here could be shared and another user could easily incorporate a simulation file for their own target. An example text file for the cyclotron and target is shown in the appendix. Functionally, TOPAS derives its physics lists from Geant4, providing the same underlying operating mechanisms.

4.2 Methods

For all TOPAS simulations, ten iterations of the simulation were conducted with 10 different seed numbers. The results are summed over all 10 seed numbers. The number of incident particles (protons) varied from 10^7 – 10^9 per simulation and is chosen per scenario to maintain a reasonable simulation time. Unless specified, the default TOPAS physics list was used. The physics list determines what model or process dictates a particle's interactions and movement in different energy regimes; the physics lists used and their differences are detailed in Section 4.2.2. All simulations were conducted on the UC Research Computing Center computing

cluster. Example "cyclotron" and "target" files are provided in the appendix.

4.2.1 Simulating Cyclotron Beam Parameters

The starting parameters for the beam simulation were based on Tamburella and Giles 2008, in which the spot size of a 2-3 μA beam was measured on paper for the same model of cyclotron used in this study (an IBA CYCLONE 18/9 cyclotron) [93]. The current used herein was substantially higher (40 μA), so a more dispersed beam would be expected. While the spot size (beam diameter) of the cyclotron used experimentally at the UC Cyclotron Facility could not be observed, values reported in the literature range from 10 mm – 15 mm [26] [78]. Therefore, several beam sizes were assessed in the simulations.

In the TOPAS simulations, the beam was described as a bivariate 2D gaussian distribution emission source; it can be mathematically described using Eqn. 4.1.

$$P(x,y) = \frac{1}{2\pi\sigma_x\sigma_y\sqrt{1-\rho^2}} exp\left(-\frac{1}{2(1-\rho^2)}\left[\left(\frac{x-\mu_x}{\sigma_x}\right)^2 \right.\right.$$

$$\left.\left. -2\rho\left(\frac{x-\mu_x}{\sigma_x}\right)\left(\frac{y-\mu_y}{\sigma_y}\right) + \left(\frac{y-\mu_y}{\sigma_y}\right)^2\right]\right) \tag{4.1}$$

In simulation, the proton beam source is described in terms of emittance. The beam was adjusted in terms of parameters σ, the spread in particle position, σ', the spread in momentum direction, and correlation, the correlation of σ and σ'. A LYSO (lutetium-yttrium oxyorthosilicate) detector was simulated at the target plane, with dimensions of 10 cm x 10 cm x 0.2 cm segmented into 1000 x 1000 x 1 bins. The energy deposited per bin was counted and the resulting intensity images analyzed in MATLAB [69]. The middle 10 bins were averaged together to obtain a 2D depiction of the beam. A Gaussian fit was applied to the function using the MATLAB fit function and Eqn. 4.2, where x is the input data of energy deposited per bin and a, b, and σ are fitted coefficients. This is demonstrated in

Fig. 4.1, where the blue 'data' points are the energy per bin and the red 'fitted curve' is the Gaussian fit to this distribution. The σ term was converted to FWHM using Eqn. 4.3. The beam parameters were adjusted until the resulting beam FWHM corresponded with that found in the literature [26] [78].

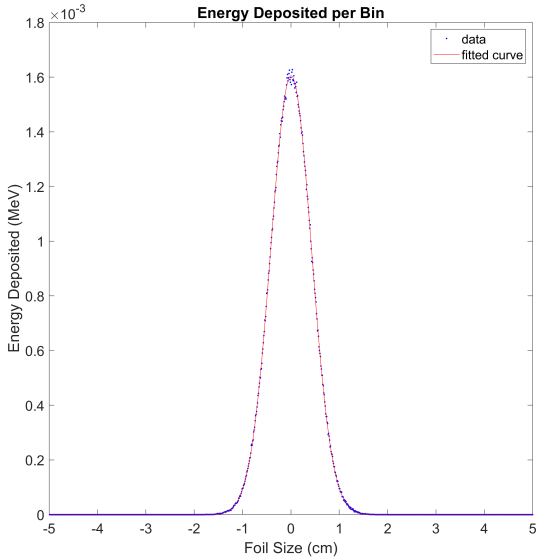

Figure 4.1: Beam profile of simulated 18 MeV proton beam on LYSO detector. The blue points show the energy deposited per bin normalized to 10^7 incident protons; the red line is the Gaussian fit to that data. Emittance parameters: $\sigma = 0.1$, $\sigma' = 0.001$, correlation = 0.1.

$$f(x) = ae\frac{(x-b)^2}{2\sigma^2} \tag{4.2}$$

$$FWHM = 2\sqrt{2ln(2)}\sigma \tag{4.3}$$

4.2.2 Determining the Physics List by Cross Section Analysis

The cross section was measured using a simulated stack of thin natural titanium (^{nat}Ti) foils; natural titanium is 73.7% titanium-48 (^{48}Ti). The purpose was to determine which physics list provided best approximates the recommended cross section for the ^{nat}Ti(p,n)^{48}V reaction in the 7-20 MeV energy range. An image of the irradiated foils is shown in Fig. 4.2, with the blue foil on the far right being the thickest, first incident foil. The foil thicknesses were

adjusted using CSDA (continuous slowing down approximation) range tables [7] such that 1 MeV was lost per foil; the starting energy of the beam was 20 MeV. The foil specifications are given in Table 4.1. Each foil had a diameter of 4 cm and was separated from adjacent foils by 1 cm. The number of ^{48}V ions generated per foil was counted using the OriginCount scorer in TOPAS and converted to cross section using Eqn. 4.4. N_T is the number of ions counted in the simulation; A is the atomic mass; N_A is Avogadro's number; N_P is the number of incident protons; ρ is the target density; and t is the target thickness. While not used experimentally, in some simulations, a diffuser was added at the front of the foil stack in the form of a thin 0.193 mm aluminum foil. In these simulations, the beam energy was increased to 21 MeV so that 1 MeV was lost in the diffuser.

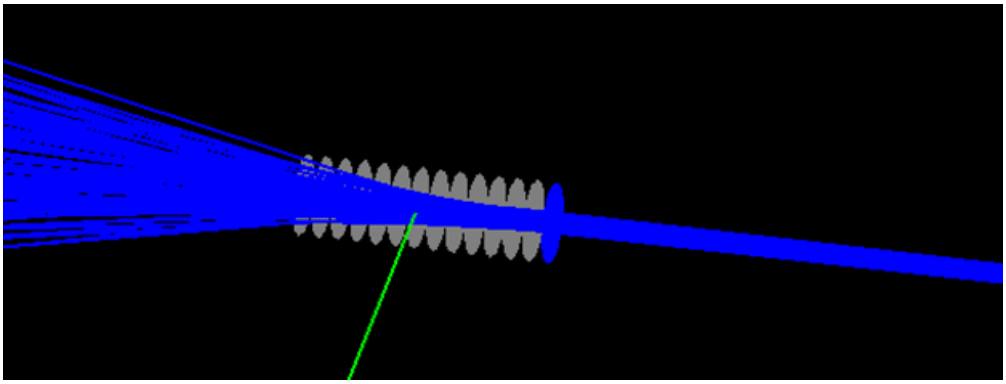

Figure 4.2: Simulated foil stack with 1000 incident 20 MeV protons (trajectory shown as blue lines).

$$\sigma = \frac{N_T A}{N_A N_p \rho t} \tag{4.4}$$

Several physics lists were assessed to determine an appropriate list for this study. Many Geant4 physics lists (used by TOPAS) are not well-suited for low energy and light target nuclei and have been shown to be inaccurate in these scenarios [81]. To determine their utility, each list was used to measure the cross section of the ^{nat}Ti(p,n)^{48}V reaction from 7-20

Geometry	Dimensions [mm]	Volume [mm^3]	Density [g/cm^3]	Material
Foil Stack	Diameter: 40		4.5	Natural Titanium
	Thickness:			
	0.121	152.1		
	0.121	152.1		
	0.114	143.3		
	0.108	135.7		
	0.108	135.7		
	0.095	119.4		
	0.095	119.4		
	0.089	111.8		
	0.082	103.0		
	0.082	103.0		
	0.072	90.5		
	0.066	82.9		
	0.06	75.4		
	0.054	67.9		
Foil Stack with Diffuser	Above plus:		2.7	Aluminum
	Diameter: 40			
	Thickness:			
	0.193	242.5		
Cup of 2 Foils	Diameter: 15 or 17		4.5	Natural Titanium
	Thickness:			
	0.024	15.0		
	0.025	15.6		
Sphere of 2 Foils	Diameter:			Natural Titanium
	8	268	0.20	
	10	524	0.10	
	12	905	0.059	
	14	1437	0.0372	

Table 4.1: Description of target geometries simulated in TOPAS in terms of their dimensions, volume, density, and material.

MeV; the resulting cross section was compared to experimental results [40] and theoretical calculations [57]. An energy range of 7-20 MeV was observed because it is the range around the experimentally used proton energy of 18 MeV. Observing such a wide range allows an assessment of whether any discrepancies are present with the physics list in general or just at a specified energy.

TOPAS offers the option for modular or reference physics lists. Modular lists specify a particular physics module or list per process or energy regime, allowing users to construct and customize their own physics list. In contrast, reference physics lists describe all processes by a specific model per energy regime and cannot be adjusted. In this study, only reference physics lists were used to prevent the exclusion of any processes. The physics lists assessed were: QGSP BERT HP; QGSP BIC HP; QGSP INCLXX; QGSP INCLXX HP; QBBC; FTF BIC; FTFP INCLXX HP; FTFP BERT; and the TOPAS default physics list. 'QGSP' uses the quark gluon string (QGS) model for particle interactions above 6 GeV; 'BIC' refers to the Binary Cascade Model, used below 20 MeV; 'BERT' refers to the Bertini Cascade Model, used below 10 GeV; 'HP' refers to the High Precision Neutron Model, used below 20 MeV; 'INCLXX' refers to the Liege Intranuclear Cascade model for particle reactions below 3 GeV; 'QBBC' uses the QGS, Binary Cascade, and Bertini Cascade models, as well as CHIPS, which describes photo-nuclear and EM-nuclear interaction processes; 'FTF' referes to FriTjoF, the diffractive string excitation model and an alternative to the QGS model. The QBBC list is recommended for medical physics simulations [97].

4.2.3 Simulating Target Irradiation

Targets were simulated to mimic the cup and sphere geometries that were experimentally irradiated, described in Section 3.2.2. The cup was simulated as a cup with base diameter and side height cumulatively equal to the diameter of the foil. The thickness of the base and sides was equivalent to the thickness of two foils. The 'side' and 'base' of the foil were scored separately to observe the number of ^{48}V ions generated in each. To simulate the sphere, a diameter of 8-14 mm and mass equivalence of two foils was assumed; the density of the target was adjusted accordingly to reflect the volume and mass specified. The specifications of each target are detailed in Table 4.1. Simulated target irradiation used the beam parameters determined to be optimal in Section 4.2.1, the physics lists determined to be optimal in

Section 4.2.2, and 10^8 protons per simulation, limited by time constraints posed by the computing cluster used. The number of ^{48}V ions counted as being generated in the target was then converted to radioactivity using Eqn. 4.5. N_T is the number of ions counted in the simulation; I is the current; N_P is the number of incident protons used in the simulation; λ is the decay constant of ^{48}V; and t is the time irradiated. To simulate variations in target placement within the beamstop, simulations were also done where the target was rotated or moved along the z-axis closer to the beam (denoted by a positive z unit) or farther from the beam (denoted by a negative z unit).

$$A(t) = \frac{N_T I(1 - e^{-\lambda t})}{N_P} \tag{4.5}$$

For comparison, the theoretical radioactivity was also calculated using Eqn. 3.1 and cross section values from the IAEA where available or Cervenak and Lebeda 2020 otherwise [19] [40].

4.3 Results

4.3.1 Effect of Emittance Parameters

Fig. 4.2 shows an example profile of an 18 MeV proton beam on the simulated LYSO detector; 10^7 protons were used, and the output is normalized to the energy deposited per particle. Fig. 4.3 shows the effect of changing σ, σ', and correlation on the FWHM. While simulations with larger values of σ' (such as 0.1 and 1) were conducted, the energy deposited was disperse across the detector and a Gaussian peak was not visible. The emittance parameters outlined previously by Tamburella and Giles suggest a beam with FWHM closer to 2-3 mm for the IBA 18/9 Cyclone, although other publications found a spot size closer to 10-15 mm [26] [78] [93]. Additionally, this study herein used higher current experimentally (40 μA) compared to the 2-3 μA used by Tamburella and Giles. Therefore, a wider beam was determined to be

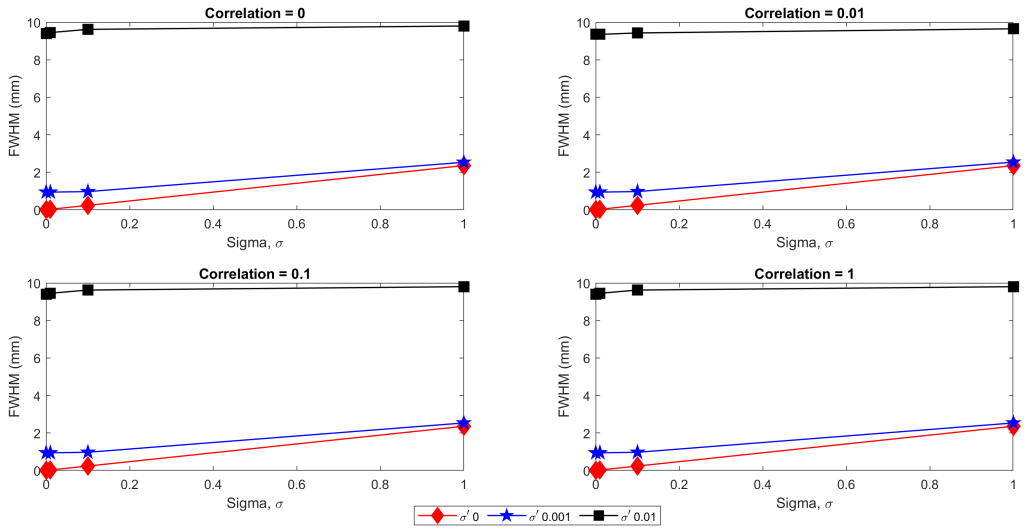

Figure 4.3: Variation of FWHM (mm) with σ and σ' for different values of correlation. While the energy deposited per detector was also observed for larger σ' values of 0.1 and 1, the energy deposition was low across the entire detector and a Gaussian peak was not discernible. Therefore, the results for these parameters are not shown.

more realistic. Parameters that generated a FWHM of approximately 10 mm were chosen: σ=0.1, σ'=0.001, correlation=0.1 generated a FWHM of 9.92 mm. The beam profile resulting from these parameters is shown in Fig. 4.1.

4.3.2 Beam Profile Across Foil Stack

The foil stack described in Section 4.2.2 was simulated using the beam parameters established in Section 4.3.1. Fig. 4.4 shows how the FWHM of the beam profile changes with successive foils, from a FWHM of 0.99 cm at the first foil to a FWHM of 1.74 cm at the last (14th) foil. While the beam size nearly doubles as it traverses the foil stack, it is still smaller than the width of the foil (2 cm). The figure also shows how the number of incident protons changes as the beam traverses the foil. For 10^7 incident protons, >99.99±0.0001% strike the first foil (9999871±11 protons) and 94.22±0.005% (9822478±481 protons) strike the last foil, a 5% decrease in the number of incident protons.

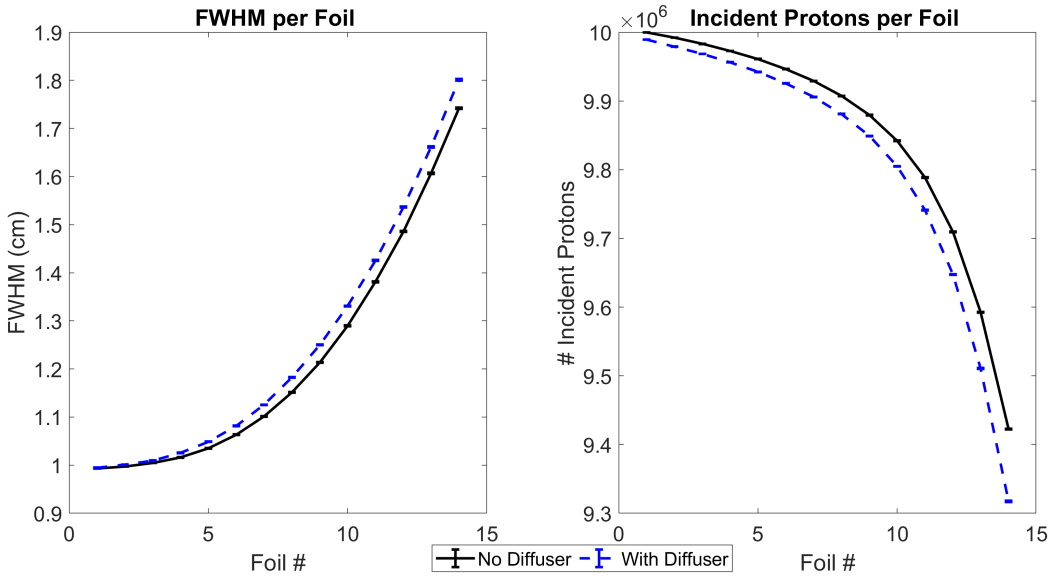

Figure 4.4: Left: FWHM of 10^7 protons incident on natural titanium foils with (blue) or without (black) a diffuser; Right: Number of incident protons with (blue) or without (black) a diffuser. When the diffuser was added, the incident energy was increased to 21 MeV. Emittance parameters: $\sigma = 0.1$, $\sigma' = 0.001$, correlation = 0.1.

Effect of Diffuser

While a diffuser foil was not used experimentally, one or more intermediary foils are often used in foil stack experiments to monitor the reaction and energy [55]; for a diverging beam, these can also have the effect of acting as a diffuser. Therefore, a thin 0.193 mm aluminum foil was added in simulation to observe the effect of such a foil on beam distribution and yield across the foil stack. The incident proton energy was increased to 21 MeV and the thickness of the aluminum foil was chosen such that 1 MeV average proton energy was lost traversing the foil. Fig. 4.4 shows the FWHM per foil and the number of incident protons on the foils. Introducing the diffuser widens the FWHM somewhat, and the effect is more pronounced as the beam traverses the foil stack: while the diffuser only widens the FWHM by 0.2% at the first foil, it widens it by 3.4% at the last foil. Similarly, the number of incident protons is somewhat deceased due to the diffuser: foil 1 saw 0.1% fewer protons compared to the foil 1 without the diffuser, while foil 14 saw 1% fewer protons. In both cases, the FWHM is still

smaller than the size of the foil, so most of the beam strikes the foil.

4.3.3 Determining the Physics List

Fig. 4.5 shows the cross section using each physics list with the beam parameters determined in Section 4.3.1, and 10^9 incident protons. The cross sections were calculated using Eqn. 4.4.

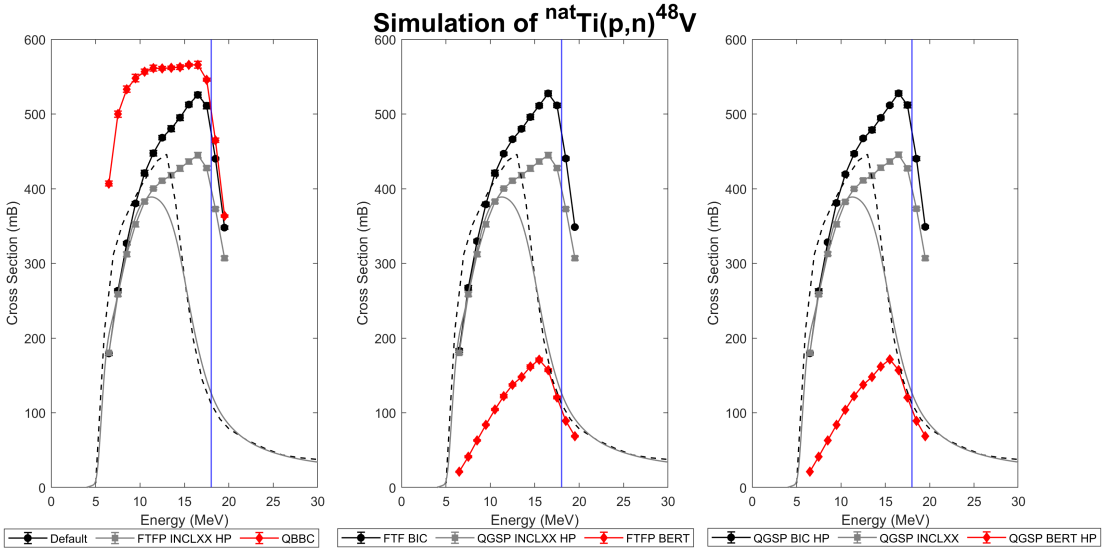

Figure 4.5: Cross sections using various physics lists. For comparison, the cross section from TENDL is shown in a dashed grey line and the recommended cross section from the IAEA is shown with a solid grey line in each plot. While certain physics lists produce cross sections that agree with the TENDL and experimental data in certain energy regions, there is no physics list that agrees with both in all of the energy regions studied [40][57].

For comparison, the experimental cross section recommended by the IAEA (solid grey line) and the cross section from TENDL based on theoretical calculation (dashed grey line) are also shown in each plot [40] [57].

In Fig. 4.5A (left), the Default physics list agrees best with the IAEA recommended cross section in the region of 7.5-9.5 MeV, varying between the two lists from 1.9-5.0%; the FTFP INCLXX HP physics list agrees well in the region of 7.5 – 11.5 MeV, varying between the two lists from 0.1-2.7%; and the QBBC physics list does not agree particularly well (>45% difference) for any energy.

In Fig. 4.5B (middle), the FTF BIC physics list agrees best with the IAEA recommended cross section in the region of 7.5-9.5 MeV, varying between the two lists from 3.4-4.7%; the QGSP INCLXX HP physics list agrees well in the region of 7.5 – 11.5 MeV, varying between the two lists from 0.1-2.7%; and the FTFP BERT physics list agrees somewhat in the region of 16.5-18.5 MeV, varying between the two lists from 16.3-20.7%.

In Fig. 4.5C (right), the QGSP BIC HP physics list agrees best with the IAEA recommended cross section in the region of 7.5-10.5 MeV, varying between the two lists from 1.6-5.2%; the QGSP INCLXX physics list agrees well in the region of 7.5-10.5 MeV, varying between the two lists from 0.1-2.7%; and the QGSP BERT HP physics list agrees somewhat in the region of 16.5-18.5 MeV, varying between the two lists from 16.4-20.7%.

In general, Fig. 4.5 demonstrates that the cross sections stemming from these physics lists are influenced primarily by the cascade model used (BERT - the Bertini Cascade Model, BIC - the Binary Cascade Model, or INCLXX - the Liege Intranuclear Cascade model); those with the same cascade model have the same general shape and similar values. To quantify the difference between different physics lists using the same cascade model, the standard deviation amongst the lists with the same cascade model at a given energy point was calculated, then summed over all energy values. The cumulative normalized standard deviation between physics lists was 0.013 for those using BERT (two physics lists), 0.035 for those using BIC (three physics lists), and 0.0067 for those using INCLXX (three physics lists). These models dominate the interaction in the energy range studied, while other models included in the physics list likely affect interactions in higher (>1 GeV) energy ranges [97].

The inclusion of the HP (high precision neutron model) in the physics list did not appear to be very impactful at this energy range; for the QGSP INCLXX and QGSP INCLXX HP physics lists, the greatest percent difference at any energy between physics lists using that model was 0.12% at 12.5 MeV; the difference was within the standard deviation at that energy.

The cross section is not expected to change substantially as the beam traverses the target because a thin target is used; therefore, a physics list that corresponds well with experimental results around 18 MeV (the energy of the incident protons) is logical. While the simulated cross section using the Bertini Cascade model (FTFP BERT, QGSP BERT HP) underestimated the cross section by approximately 18% in this energy region, it was the closest of the physics lists studied. Because these lists only differ at higher energies, either could be applicable; QGSP BERT HP was used because it had smaller standard deviation in this energy range.

4.3.4 Simulating Target Irradiation

The targets used in the simulations are described in Table 4.1. To reflect variations in geometry in forming the target, the "sphere" geometry was simulated with varying diameters (8 mm, 10 mm, 12 mm, 14 mm) and the "cup" geometry was simulated with varying base size (15 mm, 17 mm). Targets are placed in the beamstop by hand; therefore, there is likely to be some variation in their exact placement within the beamstop. Additionally, a target could shift when exposed to the vacuum of the cyclotron. For both geometries, they were therefore simulated 2 cm closer to and 2 cm farther way from the point of origin. The "cup" geometry was also simulated with various angular offsets; this was not simulated with the "spheres" because they were simulated to be homogeneous.

The number of ^{48}V ions generated in TOPAS was counted per target; the results are shown in Tables 4.2 and 4.3. Using Eqn. 4.5, these results were calculated as a radioactivity assuming 8 hours of irradiation for 5 days (cumulative 40 hours of irradiation), 2 days of decay, and assay the following day; this is done to represent the irradiation schema used experimentally. The activities are shown in Fig. 4.6 for both cup and sphere targets. All TOPAS results are due to ^{48}V only; this would account for 92% of the radioactivity at the time of assay.

Target Translation	Cup Geometry			
	24 μm thick 15 mm base	24 μm thick 17 mm base	25 μm thick 15 mm base	25 μm thick 17 mm base
TransZ = 0 cm	12954 ± 344	13327±256	13781 ± 305	13874±266
TransZ = 2 cm	13016 ± 391	13412±319	13885 ± 301	13976±319
TransZ = -2 cm	12836 ± 309	13355±296	13765 ± 295	13914±309
Rotation = 10°	16100 ± 311	15142±346	20879 ± 527	15807±350
Rotation = 15°	16201 ± 500	15338±332	20947 ± 491	16088±363

Table 4.2: Counts scored in TOPAS using the Origin Count scorer, which counts the number of ^{48}V ions generated in a volume. The targets are two stacked foils of either 24 μm or 25 μm cumulative thickness on the base and have a base width of either 15 mm or 17 mm, reflecting the variability in target formation.

Target Translation	Sphere Geometry			
	8 mm diameter	10 mm diameter	12 mm diameter	14 mm diameter
TransZ = 0 cm	73403 ± 796	61184 ± 993	50973 ± 812	43389 ± 752
TransZ = 2 cm	73931 ± 766	61587 ± 987	51346 ± 805	43615 ± 730
TransZ = -2 cm	72886 ± 792	60729 ± 961	50682 ± 793	43167 ± 756

Table 4.3: Counts scored in TOPAS. The target is a sphere consisting of the mass equivalent to 2 foils and with various diameters

Effect of Translation Along Z Axis

For the cup-shaped targets, moving the target closer to the beam (TransZ = 2 cm) resulted in less than 1% increased ions generated: for the 24 μm thick target with 15 mm base, this translation resulted in a 0.48% increase; for the 24 μm thick target with 17 mm base, a 0.64% increase; for the for the 25 μm thick target with 15 mm base, a 0.75% increase; and for the 25 μm thick target with 17 mm base, a 0.74% increase.

Similarly, moving the cup-shaped targets farther away (TransZ = -2 cm) resulted in less than 1% decreased ions generated: for the 24 μm thick target with 15 mm base, this translation resulted in a 0.91% decrease; for the 24 μm thick target with 17 mm base, a 0.21% increase; for the for the 25 μm thick target with 15 mm base, a 0.12% decrease; and for the 25 μm thick target with 17 mm base, a 0.29% increase. This indicates that for the

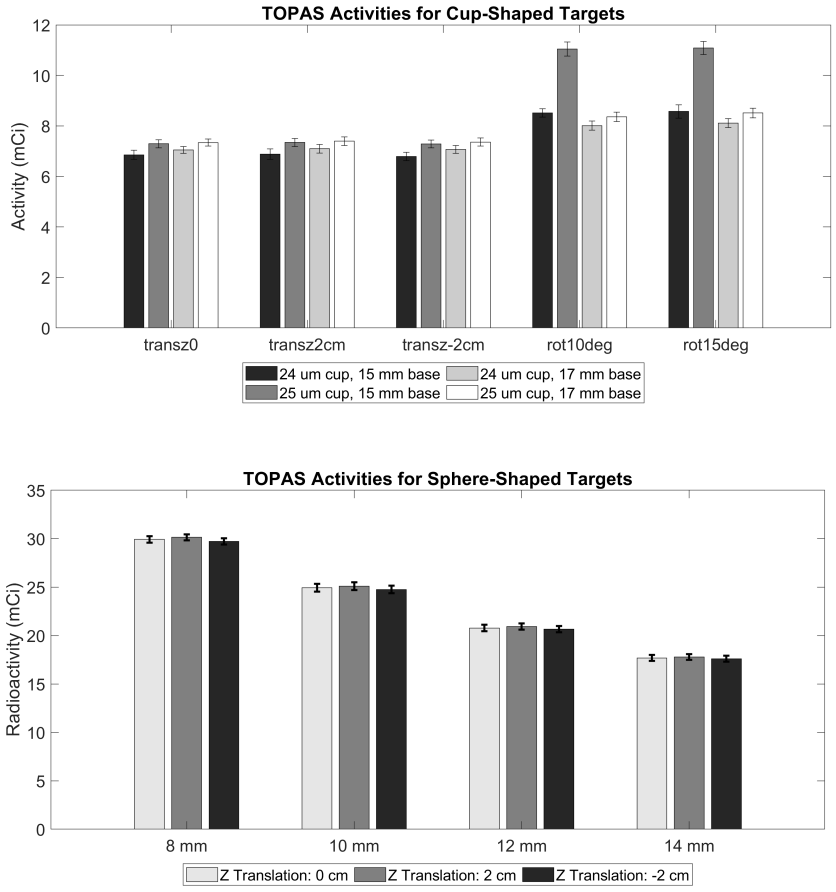

Figure 4.6: (A- Top) Activities from TOPAS for cup-shaped targets of 24 μm or 25 μm thickness and 15 mm or 17 mm base. (B – Bottom) Activities from TOPAS for sphere-shaped targets of 8 mm, 10 mm, 12 mm, or 14 mm diameter.

cup geometries, placing the target at different translations along the beamstop (such as if it becomes stuck or moves due to the vacuum) will not drastically impact the yield. This is because the beam is narrow enough that when directly incident on the target, it is primarily striking the base of the cup; for all of the targets at 0 cm translation, more than 83% of the ions generated were created in the base of the cup as opposed to the rim.

The sphere targets saw less than 1% variation in ions generated due to translation within the beamstop. For a 8 mm diameter target, a translation of 2 cm closer to and farther from the beam resulted in a 0.72% increase and 0.70% decrease, respectively; for a 10 mm diameter target, a translation of 2 cm closer to and farther from the beam resulted in a 0.66% increase

and 0.74% decrease, respectively; for a 12 mm diameter target, a translation of 2 cm closer to and farther from the beam resulted in a 0.73% increase and 0.57% decrease, respectively; and for a 14 mm diameter target, a translation of 2 cm closer to and farther from the beam resulted in a 0.52% increase and 0.52% decrease, respectively. The small variation could be due to the fraction of the beam striking the target; the beam size grows larger with distance to the target.

Effect of Angular Offset

Rotation increased the ions generated for all targets, with the larger increases seen in the targets with the smaller bases: for the 24 μm thick target with 15 mm base, 10° rotation produced a 24% increase and 15° rotation also produced a 25% increase; for the 24 μm thick target with 17 mm base, 10° rotation produced a 14% increase and 15° rotation produced a 15% increase. For the 25 μm thick target with 15 mm base, both 10° and 15° rotation produced a 52% increase; and for the 25 μm thick target with 17 mm base, 10° rotation produced a 14% increase and 15° rotation produced a 16% increase. This indicates that any irregularity in positioning the target with respect to angular offset can substantially affect the yield: with angular offset, the beam is more likely to strike the rim of the cup. Additionally, the effective thickness of the base of the target would also increase due to the angle.

Effect of Variation in Geometry

The targets were molded by hand using a die press; therefore, some variation was expected between targets. For a 24 μm-thick target, variation between 15 mm and 17 mm resulted in 2.8-4.0% difference for -2, 0, and 2 cm translation. When the target is rotated, the percent difference increased somewhat: there was a 6% difference between the 15 mm and 17 mm base targets for a 10° rotation, and a 5% difference for a 15° rotation. For the 25 μm-thick target, variation between 15 mm and 17 mm resulted in 0.7-1.0% difference for -2, 0, and 2

cm translation; 10° generated a 28% difference, and 15° generated a 26% difference. The percent difference between base sizes for target rotation was larger for the 25 μm-thick target compared to the 24 μm-thick target; this difference is likely due to the increased mass associated with the 25 μm-thick target.

Varying the sphere geometry resulted in differences in counts generated between the least and most compact targets. Decreasing the diameter from 10 mm to 8 mm resulted in a 20% increase for all displacements (-2, 0, 2 cm translation); decreasing from 12 mm to 8 mm resulted in a 44% increase for all displacements (-2, 0, 2 cm translation); and decreasing the diameter from 14 mm to 8 mm resulted in a 69% increase for all displacements (-2, 0, 2 cm translation). This indicates that the more compact the sphere, the more radioactivity that can be generated. This is because the density of the target is increased as the foils are more compacted together and a larger portion of the target is irradiated by a less disperse, more concentrated beam.

4.3.5 Comparison of Experimental, Theoretical, and Simulated Yields

Figs. 4.7 and 4.8 shows a comparison between experimental, theoretical, and simulated TOPAS yields. The TOPAS yields are normalized to the fraction of ^{48}V estimated to be present at the time of assay because only the ^{48}V generated is simulated; for all targets, ^{48}V accounts for 88-95% of the assayed radioactivity, as described in Table 3.4 in Section 3.3.3. Due to the discrepancy seen between the TOPAS and IAEA cross sections, detailed in Section 4.2.2, the targets are also normalized to the amount the QGSP BERT HP lists underestimates the cross section by, 16%.

With these adjustments, the TOPAS yields were compared to assayed yields for each target. Target 11 used two 12 μm foils; this was the only amount of mass simulated for this type of target. Target 12 was a 24 μm-thick target (two 12 μm foils), while targets 13 and 14 were 25 μm-thick targets (equivalent of two 12.5 μm foils); only these thicknesses were

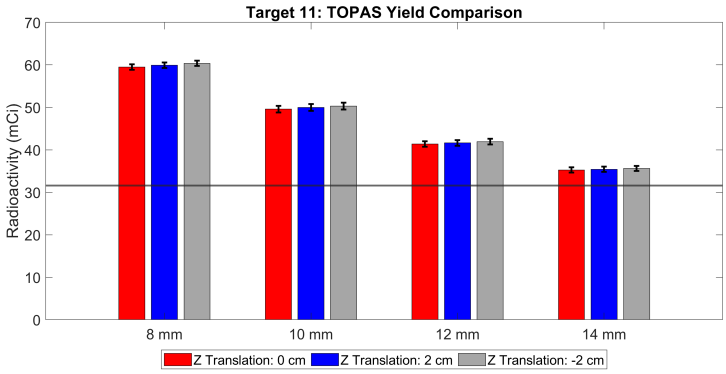

Figure 4.7: Comparison between assayed and calculated TOPAS yields for sphere-shaped targets of 8, 10, 12, and 14 mm diameters at different positions along the z-axis. The solid line is the assayed radioactivity, 31.6 mCi 67.75 hours after end of beam.

considered for each target. In general, the TOPAS simulated targets without rotation agreed with the assayed yield within a margin of error for targets 12 and 15; the simulation results with rotation agreed with the assayed or theoretical yield within a margin of error for target 13.

Target 11

All TOPAS simulations overestimated the yield compared to the assayed radioactivity of 31.6 mCi. For the 8 mm diameter, all translations provided a 88-91% overestimation of the yield; for the 10 mm diameter, all translations provided a 57-59% overestimation; for the 12 mm diameter, all translations provided a 31-33% overestimation; and for the 14 mm diameter, all translations provided a 12-13% overestimation. This last, largest diameter provided the closest values between experimental and simulation results.

Target 12

Compared to the assayed yield of 6.5 mCi, the TOPAS simulations were closest for a 15 mm base and translation of 2 cm (0.38% underestimate) and was comparable for all other

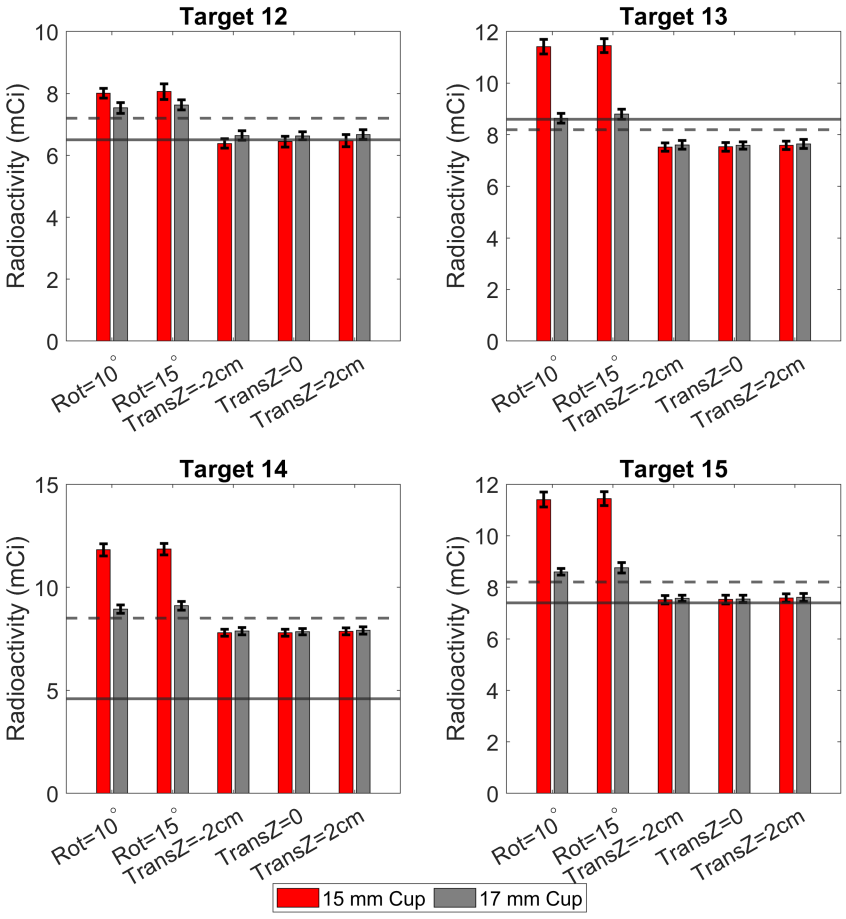

Figure 4.8: Comparison between assayed (solid horizontal line), theoretical (dashed horizontal line), and TOPAS (bars) yields for cup-shaped targets with a 15 mm base (red bars) and a 17 mm base (grey bars). The bars show the variation in radioactivity due to translation from -2 to 2 cm and from rotation of 10° and 15°. Error bars show one standard deviation of the TOPAS simulated radioactivity.

translations (0.4-1.8% error for a 15 mm base, 2.0-2.6% error for a 17 mm base). The simulations of target rotation were farther from the assayed value: for the 15 mm base, a 10° rotation simulation provided a 23% overestimation compared to the experimentally assayed radioactivity, while the 15° rotation simulation provided a 24% overestimation; for a 17 mm base, a 10° rotation simulation provided a 16% overestimation, while the 15° rotation simulation provided a 17% overestimation.

Target 13

Compared to the assayed yield of 8.6 mCi, the TOPAS simulations were closest for a 17 mm base and 10° rotation (0.48% overestimate); translation with this base provided a 11-12% underestimate. The 15 mm base had higher error for all targets: translation provided a 12-13% underestimate, while rotation provided a 33% overestimate for both a 10° and 15° rotation.

Target 14

All TOPAS simulations overestimated the yield substantially compared to the assayed radioactivity of 4.6 mCi. This is partially due to the target formation, detailed in Section 4.4. For the 15 mm base, translation resulted in 70-72% overestimation; rotation resulted in 159% overestimation for both 10° and 15° rotation. For the 17 mm base, translation resulted in 72-73% overestimation and rotation provided a 96-99% overestimation.

Target 15

Compared to the assayed yield of 7.4 mCi, the TOPAS simulations were closest for a 15 mm base and no rotation (2% overestimation for all translations); 10-15° rotation with this base provided a 54-55% overestimate. The 17 mm base had similarly small error for the translation (6-7% overestimation) and rotation (21-23% overestimation).

4.4 Discussion

4.4.1 Physics List

Section 4.2.2 demonstrates that no one physics list matches the accepted cross section well across the 7-20 MeV energy range studied. In the energy range observed, the IAEA and TENDL cross sections matched well with each other; Fig. 4.5 shows a high degree of

overlap between these two datasets. Ideally, the TOPAS simulated cross sections should also correspond with these results. The cross sections simulated using most physics lists do not match the IAEA and TENDL cross sections around 18 MeV. These physics lists are likely intended for higher energy simulations and seem to encounter errors when extrapolated to the lower energies used herein. While the FTFP BERT and QGSP BERT HP (the list used herein) physics lists matched IAEA results the best around 18 MeV (the energy used experimentally) of the physics lists studied, the error was still quite large at 16.3-20.7% for both physics lists across the energy region of interest (16.5-18.5 MeV). Additionally, the error becomes larger at lower energies, making it difficult to use this physics list for simulations of thicker targets where the average proton energy is likely to decrease, such as simulations with the sphere shaped targets. These results indicate that the simulations would benefit from a physics list intended for low-energy simulations. TOPAS does allow users to create their own physics list, opening the possibility for adaption to this energy regime. Notably, the physics list recommended [97] for medical physics simulations, QBBC, had very poor agreement with the IAEA cross section values in the energy regime observed herein (perhaps the worst of any physics list used herein); it had >45% difference for all energies 7-20 MeV.

There are several Geant4 physics lists intended to improve computational performance that are not included in TOPAS. Simulations of foil stacks took approximately 1 hour to simulate 10^9 protons with 10 different seed numbers across four nodes. The introduction of a faster physics list could decrease the simulation time or allow more particles to be simulated in a comparable amount of time. There are other measures that could be taken to speed up the simulation, such as killing secondary particles not involved in the reaction of interest, limiting the number of steps a particle can take, or increasing the energy production cut threshold. These methods were not pursued in this work because the computational time was determined to be reasonable.

4.4.2 Target Simulations

In all simulations, only the quantity of ^{48}V produced was studied. However, ^{48}V is only one product from irradiating this target. This was done because ^{48}V is the radioisotope of interest for further studies by this group; a primary purpose of these simulations was to determine what quantity of ^{48}V was being produced. Further simulations in future work could look at the amount of co-produced radionuclides in order to get a more comprehensive estimate of the target radioactivity. The TOPAS results were normalized to the estimated fraction of ^{48}V present at time of assay for each target in order to compare the results to the experimental assays.

In general, TOPAS simulations demonstrated an increase in ions generated whenever the target was translated or rotated. This is largely because a different portion of the beam was being intercepted; in effect, the target is seeing different emittance parameters at -2 or -2 cm compared to the target at 0 cm. For target rotations, a different amount of the beam is likely irradiating the edge of the cup compared to the base. In comparing the 15 mm and 17 mm base targets, the 17 mm targets recorded higher numbers of ions generated when the target was not rotated, and the 15 mm targets had higher recorded ions generated when the target was rotated. The 17 mm base saw smaller variations between translation and rotation of the target, likely due to the smaller amount of the edge of the cup compared to the base. Due to the increase from rotating the target, it may be advantageous to purposefully tilt the target in experimental irradiation in order to increase the radioactivity generated.

Of the cup-shaped targets, target 14 had the highest deviation between simulated and assayed results. This is likely due to irregularities in target formation for this target; instead of placing two foils on top of each other, a foil was cut in two pieces and nested, making the base thickness effectively that of two foils, but leaving a smaller thickness on the sides. This was done in order to reduce the amount of target material that would have to be dissolved in the chemical separation. For a target with no rotation, the sides should not receive substantial

irradiation; indeed, a proper solid target system would only irradiate a flat foil, comparable to the cup bottom. Future work could simulate the effect of this irregular cup geometry on ^{48}V ions generated, though this formation likely will not be used again.

The sphere simulations showed at least a 12% overestimation compared to the assayed radioactivity of 31.6 mCi. This is partially attributed to the homogeneous nature of the simulated target compared to the inhomogeneous nature of the real target: the sphere targets in practice were simply crumpled foils, leading to large spaces and gaps in the target. However, the target was simulated as homogeneous spheres, likely increasing the amount of target intercepted by the beam. Adding void spaces into the target is another aspect that could be considered in future work to make simulations more realistic and better approximate the experimental yield.

4.5 Conclusions

This study showed that TOPAS simulations can be a powerful tool in both predicting target yields and assessing irradiation conditions to determine the efficacy of a cyclotron beamstop target holder. Ultimately, the irradiation and target formation conditions provide a wide range of potential irregularities that are difficult to fully capture and replicate in simulation. This is complicated by the lack of appropriate physics list at this energy regime. Despite this difficulty, this tool can help to explore the conditions that may lead to yield irregularities and serve as a guide to explore methods that may increase radioactivity yields.

CHAPTER 5

DEVELOPMENT OF HIGH-PERFORMANCE LIQUID CHROMATOGRAPHY METHODS FOR CHARACTERIZATION OF VANADYL ACETYLACETONATE

5.1 Introduction

Vanadyl acetylacetonate produced on a bulk scale has a vibrant blue color. This distinct color makes it easy to visually confirm the product synthesized. Visual confirmation of blue to green color is one element of a certificate of analysis for commercially produced $VO(acac)_2$, in addition to form (powder, crystal, or chunk), infrared spectrum, and titration by $KMnO_4$ to determine the fraction of vanadium present [4]. Unfortunately, these measures do not lend themselves to radiotracer production: 10 mCi of $^{48}VO(acac)_2$ (comparable to the radioactivity produced herein) would have the equivalent mass of 2x10^{-13} g. With such a small quantity of material produced, the color would not be visible. The consistency of the material would also not be discernible and may be altered due to the small mass; with so little material, the $VO(acac)_2$ may not be able to crystallize. Subsequently, the infrared (IR) spectrum would be weak with such a small, dilute sample; additionally, IR-viewing capabilities were not available for this study. Finally, the amount of $KMnO_4$ that would be permissible for a titration would likely be prohibitively small, making it difficult to carry out and prone to error.

In addition to the aforementioned measures, $VO(acac)_2$ can also be confirmed via ultraviolet (UV) absorption spectra, where it has been shown to have a maximum absorption around a 320 nm wavelength [46]. Often, an absorption wavelength of 254 nm is used in characterizing biological samples; historically, this wavelength was used because it is the strongest in mercury lamps, previously a common optical source [29]. This wavelength remains commonly used due to its ability to detect biological matter, such as nucleotides [8],

as well as polynuclear aromatic hydrocarbons including fluorinated and benzene compounds [53]. However, modern chromatography systems, such as the one used herein, usually contain UV lamps that allow for different wavelengths to be used in the absorption process.

Chromatography separates a sample containing a mixture into components, either to separate out or quantify the constituents [43]. In this work, reversed-phase high-performance liquid chromatography (HPLC) is used. The HPLC column used herein contains silica on which long-chain C-18 molecules are chemically immobilized and act as the "stationary phase", which bind or interact with non-polar molecules while allowing polar molecules to pass through more quickly. A polar "mobile phase" passes through the column. Molecules are sorted based on their affinity to the stationary phase: those with a higher affinity, or attraction, to the stationary phase are eluted from the column at a later time point. This affinity is determined by the substance's polarity: for reversed-phase HPLC, more polar solutes are eluted first. The length of time the sample spends in the column before proceeding is the retention time. The polarity of the mobile phase affects the retention time: more polar mobile phases lead to longer retention times [38]. The polarity index of some common mobile phases includes ethanol ($P' = 4.3$), acetonitrile ($P' = 5.8$), and water ($P' = 10.2$). For mobile phases which include a combination of solutions, their polarity is weighted against their volume fraction to determine the overall polarity of the mobile phase. Sometimes the polarity of a mobile phase is appropriate for early-eluting solutes but may lead to long retention times for later-eluting solutes. In this case, the composition of the mobile phase can be gradually adjusted so that it becomes less polar, a process called gradient elution [38].

UV detection is often used in HPLC analysis. As the sample components are eluted from the column, they go through a clear flow cell, which is irradiated with UV light. The sample absorbs part of the light according to the Beer-Lambert Law and the remainder is detected; the fraction absorbed by the sample is determined by comparing the initial and final UV intensity [23]. The UV intensity peak can be correlated with the retention time to identify a

compound; under the same mobile and stationary phase conditions, a compound should have a similar retention time across systems (subject to other conditions related to the HPLC, retention time may vary between systems).

Radiotracers are often characterized via HPLC with UV and radiation signal detection. HPLC analysis of a non-radiolabeled standard, a substance known to be the desired compound, yields a UV peak at a certain retention time. While the radiotracer may not be visible via UV spectrum due to the small mass present, it has the same retention time as the standard compound and is visible via radiation detector. Therefore, a radiation peak should be present at approximately the same time as the UV peak, with a time delay of a few seconds expected as the compound travels between the UV and radiation detector systems. The chemical identity of a radiotracer is again confirmed by co-injection of the cold reference standard with the radiotracer. In that way, the associated cold mass peak area of the radiotracer is increased significantly by the addition of the reference standard.

In this section, methods were developed to characterize vanadyl acetylacetonate ($VO(acac)_2$) via HPLC. While several methods exist to characterize $VO(acac)_2$, no HPLC methods were found in the literature to characterize this compound. HPLC characterization is useful in radiotracer production, where bulk-scale analyses cannot be used. Methods were first developed to characterize non-radiolabeled $VO(acac)_2$. Then, the established method was applied to characterize $^{48}VO(acac)_2$, as detailed in Section 6.3.4. For comparison, HPLC analysis using the same mobile phases were repeated with a sample of acetylacetone in order to find a mobile phase that would separate the two compounds, both of which could be present in the radiotracer production.

5.2 Method Development

Analyses were carried out on one of two HPLC systems at the University of Chicago Cyclotron Facility. Both systems were Agilent 1260 Infinity II HPLC systems. While retention time

can vary slightly across HPLC systems because of the slight difference in path lengths, even with the same column, mobile phase, and other conditions, results between the two systems were found to be consistent and are therefore not discussed herein.

Initially, two samples were prepared: a sample of 7 mg of $VO(acac)_2$ dissolved in 3.5 mL of 100% EtOH for a concentration of 2 mg/mL. In some cases, fresh samples (prepared at the time of use) of $VO(acac)_2$ were compared to older samples (date of preparation <1 week). For comparison, a sample of 50 μL acetylacetone in 900 μL EtOH was prepared; after preliminary assessments, it was diluted 10 times to display a similar peak amplitude to $VO(acac)_2$ for a final sample concentration of acetylacetone of 5.4 mg/mL. Unless specified, commercially available acetylacetone was used.

An injection volume of 5 μL was used consistently for both samples unless otherwise noted; this volume corresponds to a mass of 0.027 mg of acetylacetone or 0.01 mg of $VO(acac)_2$ per injection. Two organic solvents were considered as mobile phases: EtOH and acetonitrile (MeCN). The proportion of the mobile phase and water was altered in a systematic way and the resulting UV spectrum observed. Both isocratic (fixed composition) and gradient (varying composition) elution profiles were considered for the mobile phase. In addition to the mobile phase, an acidifier was sometimes added in the form of 0.1% trifluoroacetic acid (TFA); this was added to MeCN and water, but not to EtOH as the solvent itself can provide the required H^+ ions (protons) for better peak resolution. The flow rate was varied from 1.0 mL/min. – 1.5 mL/min. across different HPLC assays but was constant within one assay; the flow rate did not change as a function of time. The duration of the HPLC changed for some analyses but was generally 15 minutes long per assay. Finally, two wavelengths were considered: 254 nm and 320 nm. Many methods were assessed using the 254 nm wavelength before reading that the 320 nm was the optimal wavelength for $VO(acac)_2$ [46].

5.2.1 Acetylacetone Cleaning Procedure

In some cases, cleaned acetylacetone was used in lieu of acetylacetonate straight from the bottle. This was done to remove any potential contaminant hydrolysis products, primarily acetic acid, that may have formed while the compound was stored. Acetylacetone was added to a separatory funnel along with 4% $NaHCO_3$. The solution was shaken vigorously for several minutes with the occasional release of gas formed during the process. The solutions were then allowed to separate. The aqueous bottom part of the solution (likely containing acetic acid) was discarded. Brine was added to the remaining organic phase, which was again shaken vigorously, and again allowed to stand for separation. The bottom portion of the solution (containing trace $NaHCO_3$) was discarded. To the remainder was added Na_2SO_4 to remove any water; the solution was swirled repeatedly, then left for approximately 3 hours. The solution was filtered with a fritted glass filter and the filtrate collected.

5.3 Results

A summary of all HPLC combinations is shown in Table 5.1. Each condition consisted of a fractional mobile phase in water. For example, a 40-60% MeCN mobile phase would correspondingly be 60-40% water. Where one percentage is given (for example, 30% EtOH), an isocratic elution profile is used; a range of percentages (such as 40-60% MeCN) indicates a gradient elution profile. An example gradient profile for the 40-60% MeCN mobile phase is shown in Fig. 5.1. The elution profiles of several mobile phases are shown in Fig. 5.2 and described in more detail below.

5.3.1 Ethanol Mobile Phase

Two HPLC methods were attempted using EtOH as the mobile phase: one using an isocratic 30% EtOH profile and one using an isocratic 40% EtOH profile. 0.1% TFA was added to

Mobile Phase	Flow Rate [mL/min]	0.1% TFA?	Wavelength [nm]	Total Time [min.]
30% EtOH	1.0	n/a	254	15
40% EtOH	1.0	n/a	254	15
0-40% MeCN	1.5	Y	254	15
10-50% MeCN	1.5	Y	254	15
10-90% MeCN	1.0	Y	254	15
20-60% MeCN	1.5	Y	254	15
30-70% MeCN	1.2	Y	254	15
40-60% MeCN	1.0	Y	254	15
	1.2	Y	254	15
	1.5	Y	254	15
	1.5	Y	320	15
	1.2	N	254	15
	1.2	N	320	15
50-70% MeCN	1.2	N	254	15
	1.5	N	254	15

Table 5.1: HPLC conditions assessed. Conditions were varied in terms of the mobile phase and fraction of each solvent present; flow rate of the mobile phase; whether there was 0.1% TFA present in the volume of the mobile phase; the wavelength used; and the total time for the HPLC conditions.

the water but not the EtOH. The 254 nm wavelength and a 1.0 mL/min. flow rate was used. Both methods had a very broad peak with a large spike at 4:43 and 4:06, respectively. This mobile phase was not selected due to the broad peaks seen in both HPLC assays.

5.3.2 Acetonitrile Mobile Phase

0-40% MeCN

With a flow rate of 1.5 mL/min. and 0.1% TFA added, at 254 nm both $VO(acac)_2$ and acetylacetone have a retention time of 11:01 with a broad tail prior to the sharp peak. Additionally, acetylacetone also has a peak at 13:01. This method was determined to not be optimal due to the wide tail seen.

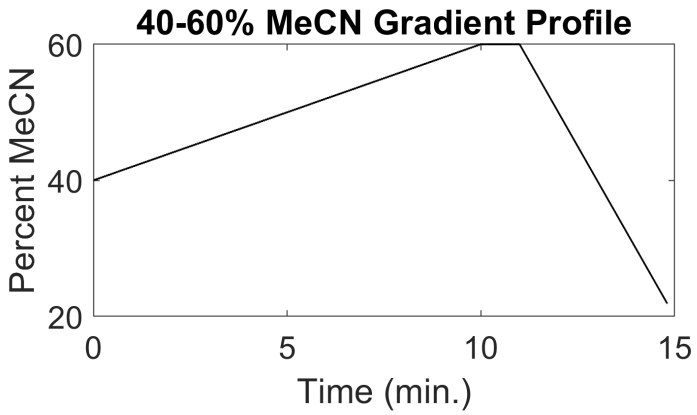

Figure 5.1: Gradient profile of the 40-60% MeCN in 0.1% TFA mobile phase.

10-50% MeCN

With a flow rate of 1.5 mL/min. and 0.1% TFA added, at 254 nm both $VO(acac)_2$ and acetylacetone have a retention time of 8:45 with a broad tail prior to the sharp peak. Additionally, several smaller peaks were seen within the tail. $VO(acac)_2$ also has a distinct peak visible at 1:44 and acetylacetone also has a peak at 10:30. This method was determined to not be optimal due to the wide tail seen.

10-90% MeCN

With a flow rate of 1.0 mL/min. and 0.1% TFA added, at 254 nm $VO(acac)_2$ had a retention time of 10:19 with another peak visible in the tail at 2:23. Due to the broad peak, this method was not investigated further in terms of other flow rates or compared to the HPLC of acetylacetone.

20-60% MeCN

With a flow rate of 1.5 mL/min. and 0.1% TFA added, at 254 nm both $VO(acac)_2$ and acetylacetone have a retention time of 6:50 with a shallow tail prior to the sharp peak. While this method was an improvement over previous methods, it was adjusted to achieve a smaller

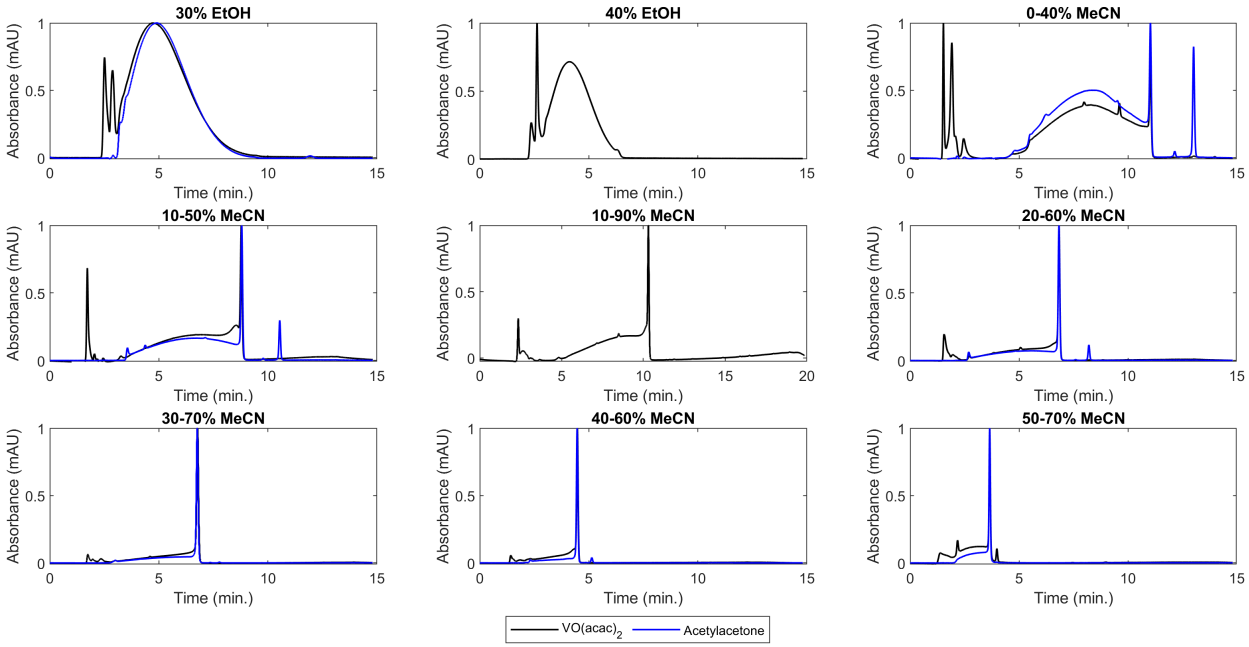

Figure 5.2: HPLC elution profiles of several mobile phases assessed, normalized to the maximum UV intensity. The black line is the profile from the $VO(acac)_2$ HPLC; the blue line is the profile from the acetylacetone HPLC.

tail and higher peak amplitude.

30-70% MeCN

With a flow rate of 1.2 mL/min. and 0.1% TFA added, at 254 nm both $VO(acac)_2$ and acetylacetone have a retention time of 6:46 with a shallow tail prior to the sharp peak. This method was suitable for further analysis, but was adjusted to ensure a method with the sharpest peak and smallest possible tail was chosen.

40-60% MeCN

This mobile phase was observed with and without 0.1% TFA added; with a flow rate of 1.0, 1.2, and 1.5 mL/min.; and using 254 nm and 320 nm wavelengths. The effect of each method is detailed below. For a flow rate of 1.5 mL/min. and 0.1% TFA added at 254 nm, both $VO(acac)_2$ and acetylacetone have a retention time of 4:28.

50-70% MeCN

A 254 nm wavelength was used to observe this HPLC method; flow rate was 1.2 mL/min. or 1.5 mL/min. over 15 minutes and assessed both $VO(acac)_2$ and acetylacetone. For a flow rate of 1.2 mL/min, a large peak was seen for both $VO(acac)_2$ and acetylacetone that had a retention time of 4:35 with a secondary peak at 4:59; there was a large tail preceding the first retention peak. For a flow rate of 1.5 mL/min, a large peak was seen for both $VO(acac)_2$ and acetylacetone that had a retention time of 3:39. While $VO(acac)_2$ had another smaller peak at 3:59, the acetylacetone had no further peaks visible. This mobile phase was not considered further due to the large tail visible prior to the retention peak.

5.3.3 Effect of Flow Rate

HPLC analyses (mobile phase 40-60% MeCN in 0.1% TFA, 254 nm wavelength) of the same sample (2 mg $VO(acac)_2$ per mL EtOH) were repeated at three different flow rates: 1.0 mL/min., 1.2 mL/min., and 1.5 mL/min. The results can be seen in Fig. 5.3A. The retention time for a flow rate of 1.0 mL/min. was 6:38; for 1.2 mL/min., the retention time was 5:33; and for 1.5 mL/min., the retention time was 4:29. As the flow rate increased, the retention time decreased.

5.3.4 Effect of Wavelength

HPLC analyses (mobile phase 40-60% MeCN in 0.1% TFA, 1.5 mL/min) of the same sample (2 mg $VO(acac)_2$ per mL EtOH) were done simultaneously with two different wavelengths: 254 nm and 320 nm. The results can be seen in Fig. 5.3B. At 320 nm, the retention time is 1:28 and the absorbance peak is sharp. At 254 nm, the retention time is 4:28 and the peak has a tail. The amplitude of the absorbance is much greater at 254 nm compared to 320 nm (approximately a 6-fold increase).

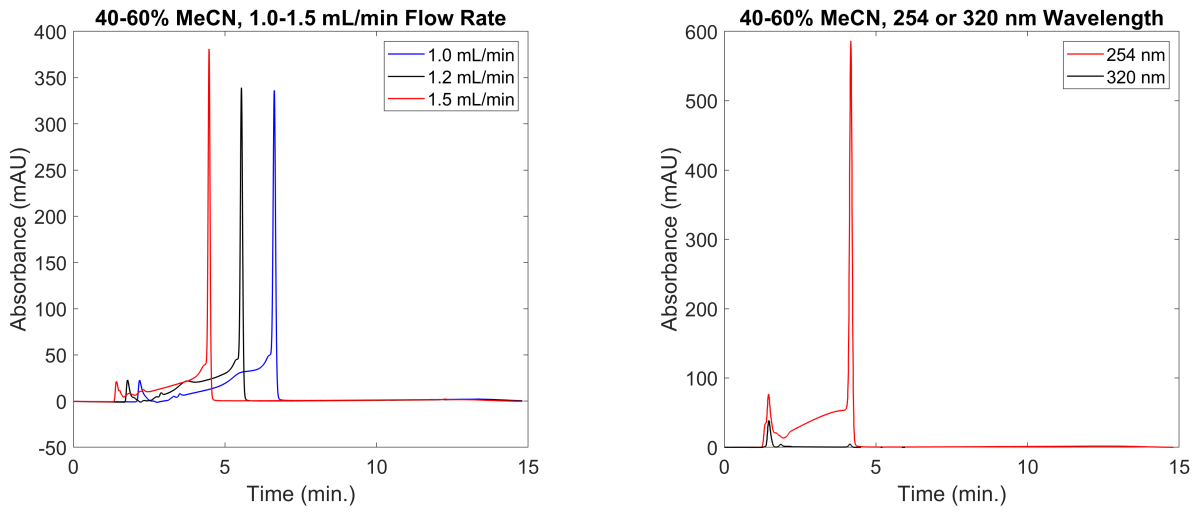

Figure 5.3: Left, A: Effect of 1.0-1.5 mL/min. flow rate on retention time; Right, B: Effect of wavelength on retention time.

5.3.5 Effect of Trifluoroacetic Acid

Without TFA, HPLC analyses (mobile phase 40-60% MeCN, 1.2 mL/min. flow rate) of the same sample (2 mg $VO(acac)_2$ per mL EtOH) were repeated with and without 0.1% TFA in the mobile phase. The results can be seen in Fig. 5.4. With TFA, the retention time for $VO(acac)_2$ was 1:28 at 254 nm and 4:28 at 320 nm. Without 0.1% TFA in the mobile phase, the retention time for $VO(acac)_2$ was 1:26 at 254 nm (with another peak visible at 5:38) and 1:26 at 320 nm.

5.3.6 Effect of Time

HPLC analyses (mobile phase 40-60% MeCN in 0.1% TFA, 320 nm wavelength, 1.5 mL/min) of the same sample (2 mg $VO(acac)_2$ per mL EtOH) were repeated over the course of a week to observe how the retention times associated with $VO(acac)_2$ change with time; this is shown in Fig. 5.5. In all three diagrams, a distinct peak is present at 1:28 min. As time progresses, the amplitude of that peak decreases, from 114 mAU on the first day after sample preparation, to 39 mAU on the fourth day after sample preparation, to 22 mAU a week

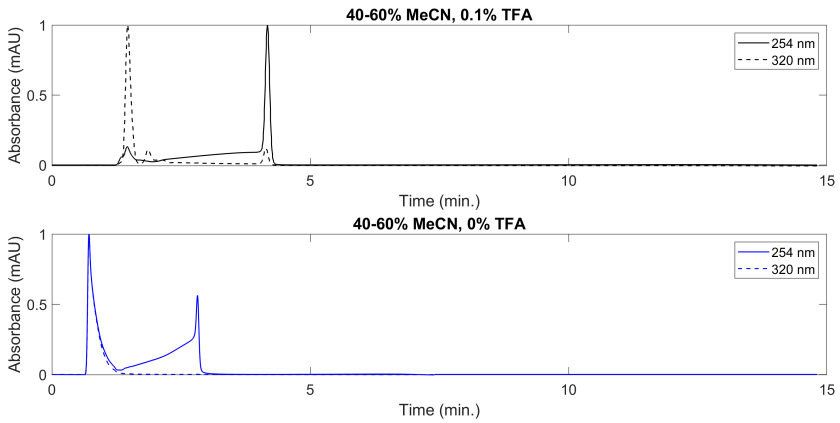

Figure 5.4: Top: HPLC of $VO(acac)_2$ with 0.1% TFA present in the mobile phase for 254 and 320 nm wavelengths; Bottom: HPLC of $VO(acac)_2$ with 0% TFA present in the mobile phase for 254 and 320 nm wavelengths. Both diagrams are normalized to the maximum absorbance.

after sample preparation. Additionally, secondary peaks begin to emerge with increasing amplitude. This indicates that the compound is not stable in EtOH and either dissociates or forms a colloid with impurities in the solution.

5.4 Discussion

The mobile phase that was chosen for further use was 40-60% MeCN with 0.1% TFA. In looking at Fig. 5.2, this was one of two methods that did not have a substantial tail present; both 30-70% and 40-60% MeCN with 0.1% TFA had tails that were small. Of these two latter mobile phases, 40-60% MeCN had a smaller, shorter tail and was thus chosen for further analysis. In general, the retention times of the acetylacetone were the same or very similar to those of the $VO(acac)_2$. The goal of the HPLC analysis was to develop a methodology that could be used to identify $^{48}VO(acac)_2$, which is formed by refluxing with acetylacetone (discussed in more detail in Chapter 6) and which vanadyl is chelated with to form $^{48}VO(acac)_2$. Therefore, it is important to identify a method that can differentiate between $VO(acac)_2$ and acetylacetone.

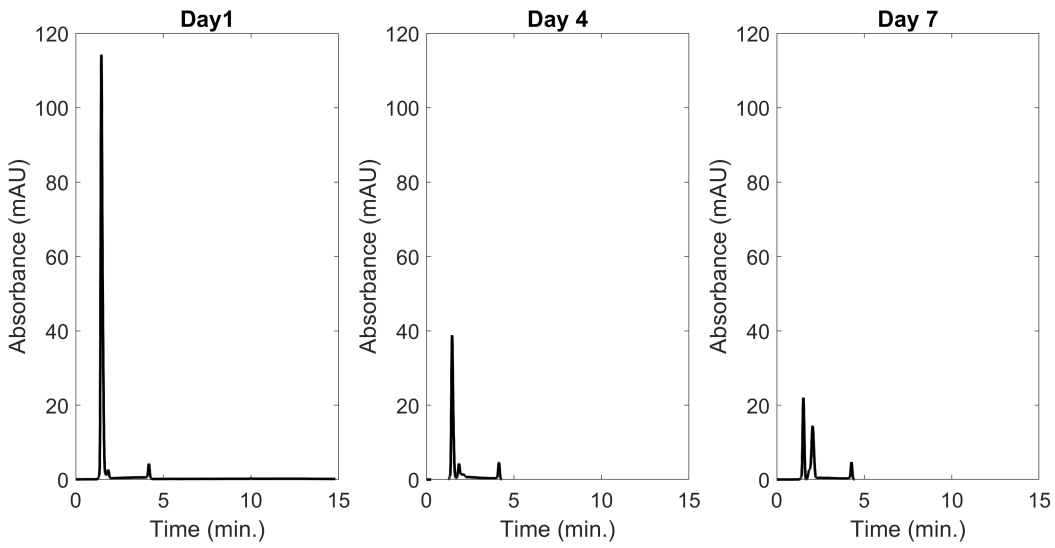

Figure 5.5: HPLC analysis of a $VO(acac)_2$ sample repeated over a week.

Of the three flow rates assessed for this mobile phase, 1.2 mL/min. was chosen for further use. In comparison, a flow rate of 1.0 mL/min. had a slightly later retention time but a slightly larger tail, while a flow rate of 1.5 mL/min. had a slightly quicker retention time and a slightly smaller tail. A smaller tail and a longer retention time are considered desirable: a smaller or no tail indicates that the compound is fully eluted by that mobile phase, while a longer retention time mitigates the possibility that the peak observed is associated with a free ion, a possibility for very short retention times (approximately 1:30 or quicker). In this sense, the 1.2 mL/min. was a compromise between the shorter tail of the 1.5 mL/min. flow rate and the longer retention time of the 1.0 mL/min. flow rate.

While $VO(acac)_2$ was visible at both 320 nm and 254 nm, acetylacetone was not visible at 320 nm. Therefore, it was determined that this wavelength could be used to identify peaks associated uniquely with $VO(acac)_2$. Notably, the amplitude of the absorbance of $VO(acac)_2$ was much greater at 254 nm compared to 320 nm (approximately a 6-fold increase), indicating that the compound more readily absorbed the 254 nm wavelength. This could be due to the amount and type of bonds present in the compound.

In general, the use of TFA resulted in sharper peaks. This is because TFA has a low

pH (2.1), helping to ensure that the analyte is fully protonated. Consistency in protonation ensures that the compound moves through the column at the same time, resulting in sharper, taller peaks as a larger portion of the compound behaves similarly [76].

An analysis of compound stability over time was pursued because of a qualitative observation that the peaks observed in the HPLC changed over time in terms of their shape and amplitude. Fig. 5.5 confirms this observation: over the course of a week, the amplitude of the main peak decreases by a factor of 5, while other peaks at later retention times become more prominent. This indicates that the compound is not completely stable in EtOH. Future work can analyze the peaks with different analyses at each time point to determine the composition of the compound over time via other modalities, such as mass spectrometry, that might be sensitive to the oxidation state of the vanadium, which can be an indicator of the state of the compound.

While a reversed-phase HPLC was used here, future work could analyze $VO(acac)_2$ via normal phase HPLC. Because the retention time of $VO(acac)_2$ was very short at 320 nm, a normal phase HPLC would likely have a longer retention time, allowing better differentiation between the compound and any potential free ions present in the solution.

5.5 Conclusions

A mobile phase of 40-60% MeCN in 0.1% TFA with a flow rate of 1.2 mL/min. and 320 nm wavelength was determined to be the best method to observe $VO(acac)_2$. While other methods provided visibility for the compound, this is the only method found that is able to differentiate between $VO(acac)_2$ and acetylacetone. This differentiation is important due to the presence of acetylacetone in the synthesized radiotracer solution, to be discussed further in Chapter 6. Due to the changing absorbance amplitude seen in the HPLC analysis of $VO(acac)_2$, it is theorized that the compound may not be stable in EtOH. Further work is needed to understand the compound stability over time and determine how the compound

changes.

CHAPTER 6

COMPOUND SYNTHESIS OF VANADIUM-48-LABELED VANADYL ACETYLACETONATE

6.1 Introduction

Non-radiolabeled vanadyl acetylacetonate ($VO(acac)_2$) is typically produced on the macroscale. Its methods of synthesis are well-established [82] [102]. However, alternative methodologies are needed for producing a substance on the radiotracer scale, where the quantity of material produced is on the level of femtograms instead of grams. Established methods often require multiple transfers of material into multiple vessels throughout the process, each of which results in the loss of material. In radiotracer synthesis, this can translate to substantial loss of radioactivity. Additionally, some macroscale methods require processes not feasible on the femtoscale, including compound crystallization for separation, which may not be possible with the small amount of material produced; removal via scratching a fritted filter, which would be difficult to do if extracting radiotracer quantities of material; or visual observation of a color change to proceed, which would not be feasible with so little material. Desirable radiotracer production methods should use as few transfers and vessels as possible while employing methods that do not require visual cues or other bulk properties.

Although a method for synthesizing $^{48}VO(acac)_2$ has not previously been established, studies producing other ^{48}V-labeled compounds are present in the literature. Several authors [33] [86] [51] [91] have prepared no-carrier-added ^{48}V from natural titanium targets. To do so, they dissolve the targets in a concentrated acid such as HF [86] or H_2SO_4 [33]; lower molarity acids are also sometimes used (2M H_2SO_4 [51], 6M H_2SO_4 [104]). The ^{48}V is then separated using an anion- or cation-exchange column such as Chelex-100, AG 50W-X8, or Dowex 1; cation exchange columns bind the positively-charged, transition metal vanadium ions while allowing other materials to pass, while anion exchange columns bind negatively

charged ions and allow the positively charged vanadium ions to pass. In the former case, the vanadium can then be selectively eluted. In these studies, the objective is to separate the ^{48}V from the target and co-produced radionuclides without any further radiolabeling.

While the radiotracer can be used in this state [44] as elemental ^{48}V, it is usually labeled in order to study a certain physiological process. Many studies have observed the movement of ^{48}V-labeled compounds *in vivo*. ^{48}V-labeled-pentavanadate has been used to observe how vanadium crosses the placenta in rats [30]. Various ^{48}V-labeled compounds were used to observe the effect of oxidation state and chemical formation on the metabolic pathway of vanadium in rats and binding in the blood [84]. ^{48}V-vanadyl-pheophorbide has been studied as a cancer imaging agent to be used in conjunction with photodynamic therapy [50]. ^{48}V-labeled-bis(maltolato)oxovanadium(IV) and ^{48}V-labeled-vanadyl sulfate were used to observe the biodistribution of each compound, which could potentially be used to lower insulin levels [89]. These studies demonstrate that no-carrier-added ^{48}V can be radiolabeled and effectively used for physiological studies.

As detailed in Chapter 1, $^{48}VO(acac)_2$ is a radiotracer of interest for its potential use in cancer detection [67] [72] [73], as well as being a potential tool to shed light on the physiology of non-radiolabeled $VO(acac)_2$ [66]. Producing this radiotracer requires separating ^{48}V as no-carrier-added ^{48}V-vanadyl and chelating it with acetylacetonate.

A key material to separating the ^{48}V is an appropriate cation or anion exchange resin. Based on the literature, two exchanges resins were assessed.

Chelex-100

Chelex-100 is a weak acid cation exchange resin with high bond strength [10]. Notably, it has a high affinity for transition metals; scandium, vanadium, and titanium are transition metals while calcium and sodium (two potential decay products and contaminants) are not. The Chelex-100 ions bind preferentially to polyvalent cations over monovalent cations. It functions

in basic, neutral, and weakly acidic solutions. At low pH (around pH = 4), it becomes an anion exchanger. When used for cation exchange, the quantity of the exchange varies with a function of pH: exchange is low if the pH of the solution is below 2, increases for pH 2-4, and is optimal for pH above 4. The resin was prepared using the column method in which the resin is regenerated by incubating it in a solution with pH 3-4 for some time, then is poured into a column. The sample solution is then passed through the column to concentrate transition ions. The desired transition ion (vanadium) is eluted with a counterion of higher selectivity than the bound metal (ammonia); the eluent is chosen so that the vanadium is selectively eluted, leaving other transition ions potentially present in the solution (titanium, scandium) bound on the column. A 100-200 mesh size was used. The mesh size is a measure of the number of openings in the resin bed per square inch. The mesh size is a tradeoff between flow rate (more rapid for 200-400 mesh) and selectivity (higher for 50-100 mesh).

AG 50W-X8

AG 50W-X8 is a strong acid cation exchange resin with sulphonic acid functional groups; cations introduced into the column bond to the negatively charged functional group (AG 50W-X8, BioRad). Analytes are eluted with a neutral or basic pH solution. The resin functions over pH 2-12. While the AG 50W-X8 resin is similar to the Chelex-100 (both have a styrene divinylbenzene copolymer lattice, though with different functional groups), AG 50W-X8 has a higher resin capacity (1.4 meg/mL compared to 0.4 meq/mL for Chelex-100). The column was prepared following the instructions for an unknown solution because the concentrations of each ion were unknown. Similar to the Chelex-100, a 100-200 mesh size was used, as recommended in the literature [104].

6.2 Methods of Radioisotope Separation and Chemical Synthesis

6.2.1 Method 1

The procedure for the Method 1 synthesis of $^{48}VO(acac)_2$ was adapted from the literature [12] [14] [15]. The flow diagram of this synthesis is provided in Fig. 6.1. Five iterations of this synthesis were done. Below is a summary of each iteration. For Method 1, adjustments were made per iteration in order to increase yields and decrease the presence of impurities; the differences between each iteration are described at the end of the section. All commercial reagents and solvents were purchased from Sigma-Aldrich (St. Louis, MO, USA), Fisher Scientific (Waltham, MA, USA), or Acros Organics (Geel, Belgium) and used without further processing unless specified.

The synthesis began with an irradiated natural titanium foil target (produced as detailed in Chapter 3) in the form of a crumpled sphere or a cup. The target was weighed, then placed in a PFA (perfluoroalkoxy alkanes) beaker. The target was not ablated, broken apart, or dissociated before dissolution. The PFA beaker containing the target was placed in a 170°C oil bath. The target was dissolved in H_2SO_4
(6 M, 1.2 mL). Additional H_2SO_4 (6 M) or small amounts (100 μL) of concentrated HF were added if the target did not dissolve within 4 hours.

After the foils were dissolved, the acid was neutralized with 1.01 g Na_2CO_3 and 0.0196 g $NaNO_3$. This is equal to the mols of H_2SO_4 and half the mols of HF for Na_2CO_3; the amount of $NaNO_3$ is determined at a 43:1 ratio to the mols of Na_2CO_3. The mixture was transferred to a platinum crucible and fused at 790°C for four hours. Once cool, the solid was transferred with water to a centrifuge tube and centrifuged at 5,000 rpm for 10 minutes. The supernatant, a clear liquid, was decanted and adjusted to pH 3-4 with 3 M HCl. Chelex-100 (3 g) was prepared by the slurry method with 10 mL of 0.9% (g/v) sodium chloride solution adjusted to pH 3-4 with concentrated HCl. Typically, the amount

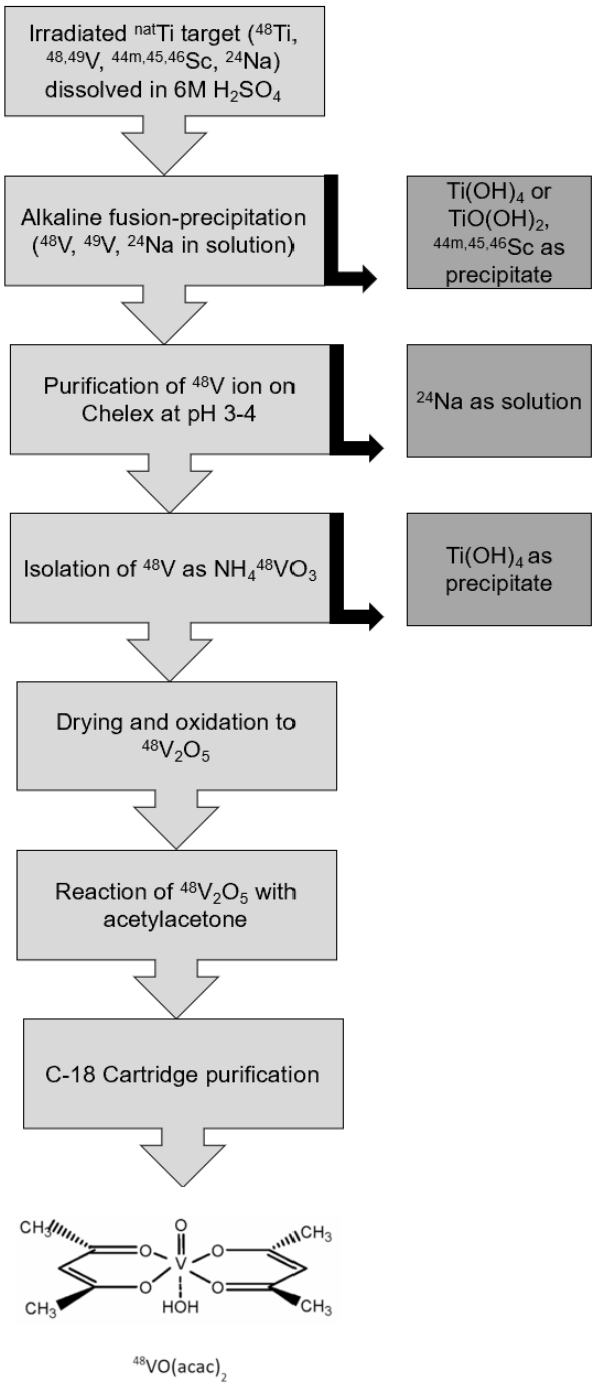

Figure 6.1: Diagram of Method 1 $^{48}VO(acac)_2$ synthesis procedure [12] [15].

of Chelex-100 resin used is determined based on the resin capacity (0.4 meq/mL). While the amount of each metal in the solution was unknown, the mass of resin needed was estimated

assuming the majority of the mass was titanium and based on the mass of the entire target, even though part of it was precipitated out in a previous step. The slurry was poured into a polypropylene column (15 cm long, 0.8 cm wide) with a frit, then conditioned with two full column volumes of the 0.9% NaCl solution. The pH adjusted supernatant containing ^{48}V was passed through the column. Vandium-48 was eluted from the column with ammonia (20%) as $NH_4\ ^{48}VO_3$ in approximately 1 mL aliquots [12].

The 1-2 aliquots with highest radioactivity were transferred to a platinum crucible and dried under an argon stream for 24 hours; the total amount used is limited by the volume of the platinum crucible. The resulting residue was converted to $^{48}V_2O_5$ by heating at 300°C for four hours [14]. The $^{48}V_2O_5$ was then converted to $^{48}VO(acac)_2$ by refluxing in the presence of acetylacetone (1-1.5 mL) for at least 24 hours [15].

Method 1: Variations

Foil Dissolution - Oil Bath: While the 170°C oil bath resulted in the most efficient dissolution, it required a high thermal stability oil that was not available for iterations 1-4. Therefore, an oil with a lower flash point was used in a 130°C oil bath for these earlier iterations.

Foil Dissolution – Acids: Initially, concentrated H_2SO_4 and HF were used (following Bonardi et al.) for iterations 1-3. In an effort to speed dissolution, 6 M H_2SO_4 was used in higher quantity for iterations 4-5. Additionally, the quantities of acid changed per iteration (specified in results); correspondingly, the quantities of Na_2CO_3 and $NaNO_3$ used varied due to their specified proportions.

Foil Dissolution - Time and Geometry: Iterations 1-3 used a sphere-shaped target, while iterations 4-5 used a cup-shaped target. Without the use of large amounts of HF (as in iteration 1), the target dissolution was slow for the sphere geometry, requiring 4-5 days for complete dissolution. Due to the long dissolution time imposed by the sphere target geometry, later iterations returned to the cup target geomtry. When sufficient acid was used to dissolve

the cup geometry (as in iteration 5), complete dissolution occured within a day.

pH Adjustment: Several concentrations of HCl were used, ranging from 0.01 M HCl to 3 M HCl. While the lower molarity HCl would be more likely to ensure the sample stayed within the desired pH range, they adjusted the pH too slowly, resulting in unnecessary radiation exposure. The amount of 3 M HCl added varied during the pH adjustment to avoid making the sample too acidic.

Reflux: The time of reflux varied between 48-72 hours.

6.2.2 Method 2

Method 2 for synthesis of $^{48}VO(acac)_2$ was adapted from the literature [104] [82]. A flow diagram of the synthesis is shown in Fig. 6.2. Two iterations of this synthesis were done.

As in Method 1, the synthesis began with irradiated natural titanium foils in the form of a cup. The foil was weighed and placed in a PFA beaker. The beaker was placed over a 140°C oil bath and the target was dissolved in 2 mL 6 M H_2SO_4.

A column was prepared by adding 50 mL of water to 3.0 g of AG 50W-X8 cation exchange resin, mesh size 100-200 μm. The slurry was poured into a polypropylene column (15 cm long, 0.8 cm wide) with a frit, then the column was conditioned with 20 mL of 3 M HCl. The target solution was diluted to 30 mL by adding 28 mL of water; the final molarity was 0.4 M. The target solution was passed slowly down the side of the column so as to not disturb the resin bed. After all solution was loaded onto the column, it was washed with 5 mL of water, then eluted with a 1% H_2O_2 0.01 M HNO_3 solution into aliquots of approximately 1 mL.

The vanadium is believed to be eluted from the column as V^{5+} vanadate. In order to form $VO(acac)_2$, the solution must be reduced to V^{4+} vanadyl. The sample was reduced by adding 100 μL concentrated H_2SO_4 to the eluted sample and heating overnight. The next day, 20 mL EtOH, 10 mL water, and 1 mL of 0.2 M H_2SO_4 were added and the sample was set to reflux overnight for iteration 1; in a separate synthesis for iteration 2, these quantities

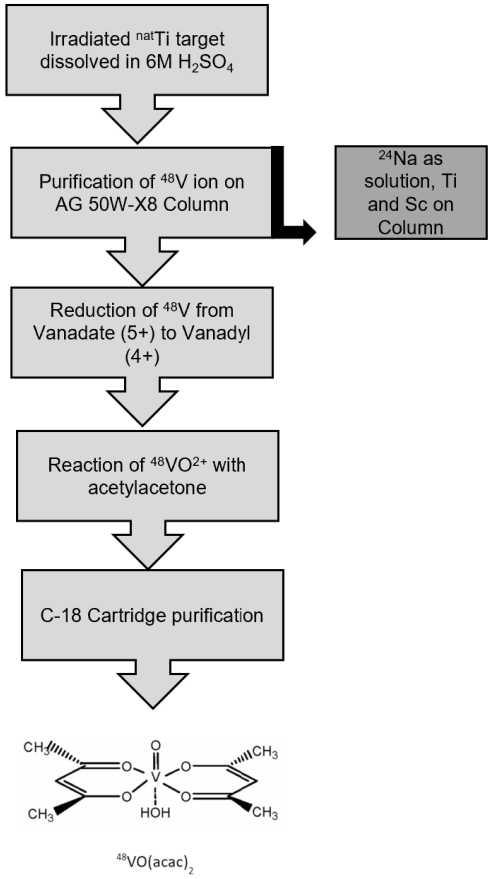

Figure 6.2: Diagram of Method 2 synthesis procedure [104].

were decreased to 1 mL EtOH, 0.5 mL water, and 0.05 mL 0.2 M H_2SO_4. The following day, 0.5 mL acetylacetone was added while shaking. After an hour, 0.8 g of Na_2CO_3 dissolved in 5 mL water was added to neutralize the solution.

6.2.3 Compound Purification

In preliminary assessments, non-radiolabeled $VO(acac)_2$ was qualitatively observed to bind to a C-18 cartridge: the blue compound could be seen when concentrated on the cartridge and could also be seen eluted from the cartridge, with no blue hue remaining after elution (Sep-Pak C18 Plus Short Cartridge; Waters Corp. Milford, MA) and could be eluted with ethanol (EtOH). Thus, it was applied to the radioactive analog. The collected compound

was allowed to cool after heating during reflux in the final step of the synthesis. Just prior to use, a C-18 cartridge was conditioned by passing 5 mL EtOH, a syringe volume (5 mL) of air, 5 mL water, and another syringe volume of air. The cooled radiotracer solution was passed through the conditioned C-18 cartridge and $^{48}VO(acac)_2$ was eluted in 400 μL EtOH as the desired, final compound.

6.2.4 Vanadium-48-Labeled Vanadyl Acetylacetonate Compound Characterization

Radioactive $^{48}VO(acac)_2$ was characterized by gamma-ray spectroscopy using the aforementioned NaI(Tl) detector (calibration methods outlined in Section 3.2.3). Methods were developed to analyze the radioactive compound via reverse-phase high performance liquid chromatography (HPLC) using non-radioactive $VO(acac)_2$ (purchased from Sigma Aldrich), outlined in Section 5.3. A 40-60% acetonitrile (MeCN)-water mobile phase with 0.1% (v:v) trifluoroacetic acid (TFA) was used for HPLC characterization.

For Method 1, iteration 4, samples from various steps along Method 1 were sent for inductively coupled plasma mass spectrometry (ICP-MS) analysis to determine the contaminant profile and efficacy of various separation procedures.

For Method 2, iteration 2, thin layer chromatography (TLC) was done using 0.1 M sodium citrate and 1:1 methanol-1 M ammonium acetate.

6.3 Results

This is the first attempt to synthesize $^{48}VO(acac)_2$ using the aforementioned procedures. Several experiments were performed to develop these methods.

6.3.1 Method 1

The step-wise yields are summarized in Table 6.1 and the fractional yield for each step is shown in Table 6.2. The overall yield was 16.50 ± 3.94% (n=5).

	Method 1					Method 2	
	I1 [mCi]	I2 [mCi]	I3 [mCi]	I4 [mCi]	I5 [mCi]	I1 [mCi]	I2 [mCi]
Starting Activity	11.7	21.6	31.6	6.5	8.6	4.6	7.4
Transferred to oven	10.6	15.6	25.8	3.7	7.5	N/A	N/A
Transferred to centrifuge	7.5	12.8	10.5	5.7	6.6	N/A	N/A
Transferred to column	7.0	11.3	9.5	4.2	5.8	2.9	4.5
Eluted from column	3.8	6.7	5.6	2.5	3.9	2.7	4.2
Transferred to oven	3.2	5.2	5.3	1.2	3.1	N/A	N/A
Set to reflux	1.3	4.0	4.9	0.8	2.3	N/A	
Extracted from RBF	1.0	1.2	3.6	0.4	1.0	N/A	3.8
Filtrate	N/A	N/A	1.7	0.2	0.5	N/A	0.8
Final Activity	1.0	1.2	1.5	0.2	0.5	N/A	0.8
Time of Synthesis	21 days	25 days	28 days	35 days	13 days	4 days	4 days

Table 6.1: Step-wise radioactivity yield summary of the chemical synthesis, not decay corrected. RBF: Round-bottom flask.

The oil bath conditions and dissolution acids are detailed below. A volume of 1.5 mL 6 M H_2SO_4 combined with an oil bath of 170°C dissolved the target quickest: 1.5 mL 6 M H_2SO_4 was added to the target during Iteration 5 in increments, resulting in complete dissolution within 24 hours. While the target from Iteration 1 also dissolved very quickly, it required a large volume of concentrated HF, which is not desirable to work with. Because of the slow decay of the radioisotope ($t_{1/2}$= 16 days), it was deemed desirable to use less HF compared to the potential gain in radioactivity.

	Method 1					Method 2	
	I1	I2	I3	I4	I5	I1	I2
Transferred to oven	97.8%	98.0%	96.5%	89.0%	92.2%	N/A	N/A
Transferred to centrifuge	94.9%	98.2%	85.4%	92.7%	87.3%	N/A	N/A
Transferred to column	95.2%	98.0%	90.5%	73.8%	86.6%	65.5%	65.0%
Eluted from column	53.9%	59.0%	64.5%	83.2%	67.8%	95.8%	97.6%
Transferred to oven	96.2%	88.9%	98.3%	97.5%	86.7%	N/A	N/A
Set to reflux	48.0%	94.0%	95.5%	76.3%	84.4%	N/A	N/A
Extracted from RBF	95.1%	37.3%	90.6%	56.2%	81.7%	N/A	98.4%
Filtrate	N/A	N/A	41.9%	62.4%	44.3%	N/A	19.9%
Final Activity	22.4%	17.3%	17.1%	13.2%	12.5%	-	12.4%

Table 6.2: Step-wise radioactivity percent yield summary of the chemical synthesis.

Oil Bath:

While the higher grade oil was rated for 180°C, it began to smoke at high temperatures: after initially heating the oil to 180°C during Iteration 5, smoking was observed. The temperature was then decreased to 160°C. After some time, the heat was increased to 170°C and the smoking was observed again. As the smoking was minimal, the oil bath was left at this temperature. After approximately four hours, the heat was increased to 180°C. Smoking could be due to impurities in the oil or debris on the heat plate. Due to the smoking, the temperature was maintained at 140°C for Method 2, Iteration 1.

Foil Dissolution – Acid Quantity and Concentration

Iteration 1: 100 μL concentrated H_2SO_4 and 400 μL concentrated HF were used for target dissolution, the latter of which was added drop-wise. Dissolution was observed to be fairly immediate, likely due to the large amount of HF used.

- Resulting mass of Na_2CO_3 was 1.59 g; mass of $NaNO_3$ was 30 mg.
- Target dissolution time: <1 day

Iteration 2: While Iteration 1 had a target quick dissolution time, it required the use of large amounts of HF, which is extremely corrosive and difficult to work with. Therefore, in subsequent iterations, an effort was made to mitigate the amount of HF required. For this iteration, 300 μL concentrated H_2SO_4 and 200 μL concentrated HF were added initially and left to dissolve the target over the weekend; an additional 50 μL concentrated HF was added on day 4 of synthesis and the target ablated with a pipette tip. On day 5 of synthesis, an additional 100 μL concentrated HF was added over 4 hours until target was dissolved. Total volume: 300 μL concentrated H_2SO_4 and 350 μL concentrated HF.

- Resulting mass of Na_2CO_3 was 1.66 g; mass of $NaNO_3$ was 31 mg.
- Target dissolution time: appx. 4 days.

Iteration 3: Initially, 300 μL concentrated H_2SO_4 and 30 μL concentrated HF were added to the foil. On day 3 of synthesis, an additional 100 μL concentrated H_2SO_4 was added and the foil was broken up with a spatula tip.

- Resulting mass of Na_2CO_3 was 0.88 g; mass of $NaNO_3$ was 16 mg.
- Target dissolution time: appx. 5 days.

Iteration 4: 600 μL 6 M H_2SO_4 was added to the foil. On day 4 of synthesis, an additional 600 μL 6 M H_2SO_4 was added and the foil broken apart with a pipette tip. The foil still was not completely dissolved on day 5 of synthesis, so an additional 100 μL concentrated HF was added. Subsequently, the foil dissolved by the following day.

- Resulting mass of Na_2CO_3 was 1.06 g; mass of $NaNO_3$ was 20 mg.
- Target dissolution time: appx. 6 days.

Iteration 5: It was theorized that a higher heat oil bath would speed the target dissolution, so the use of the 6 M H_2SO_4 was maintained but the oil bath temperature was increased to 160°. 1.5 mL 6 M H_2SO_4 was added to the foil: 1.2 mL was added initially, followed by 0.3 mL 4 hours later. The next day (after approximately 24 hours of heating), the foil was observed to have retained its shape and the acid evaporated. An addition of 1 mL of water caused the solution to bubble substantially and the target to dissociate.

- Resulting mass of Na_2CO_3 was 0.95 g; mass of $NaNO_3$ was 18 mg.
- Target dissolution time: <1 day.

Fusion

In all Method 1 iterations, most of the dissolved foil was transferred to the oven (94.7 ± 3.9%), limited only by what could be extracted from the PFA beaker; this percent is the average percent transferred across all Method 1 iterations and the error is one standard deviation of these values. Generally, the Na_2CO_3 and $NaNO_3$ added to the target solution made it solid enough to transfer easily with minimal residue left behind.

Heating was largely consistent through the iterations, with a few variables in the duration of heating.

Iteration 1: The sample was heated at 790°C for 1.5 hours. After heating, it was observed to still be free-flowing, so was heated an additional few hours.

Iteration 2-4: The sample was heated at 800°C for 4 hours.

Iteration 5: The sample was first heated at 200°C to boil off excess water, then heated at 800°C for 4 hours.

The amount of material that could be extracted from the platinum crucible for centrifugation was relatively high (91.7 ± 5.3%), limited by an effort to minimize scratching of the platinum crucible that could potentially increase contaminants. The vast majority of the radioactivity could be transferred easily with water; some additional radioactivity could be

transferred with scratching using a pipette tip, but additional material from these efforts was generally low. After centrifugation, 88.7 ± 9.6% of the sample was extracted as the supernatant, indicating that a portion of the radioactivity was trapped in the precipitate.

Fig. 6.3 shows the elution profile of the material extracted from the Chelex-100 column; the radioactivity extracted per aliquot is normalized to the radioactivity introduced to the column. During column elution, 6-10 aliquots were collected, with elution ceasing a few

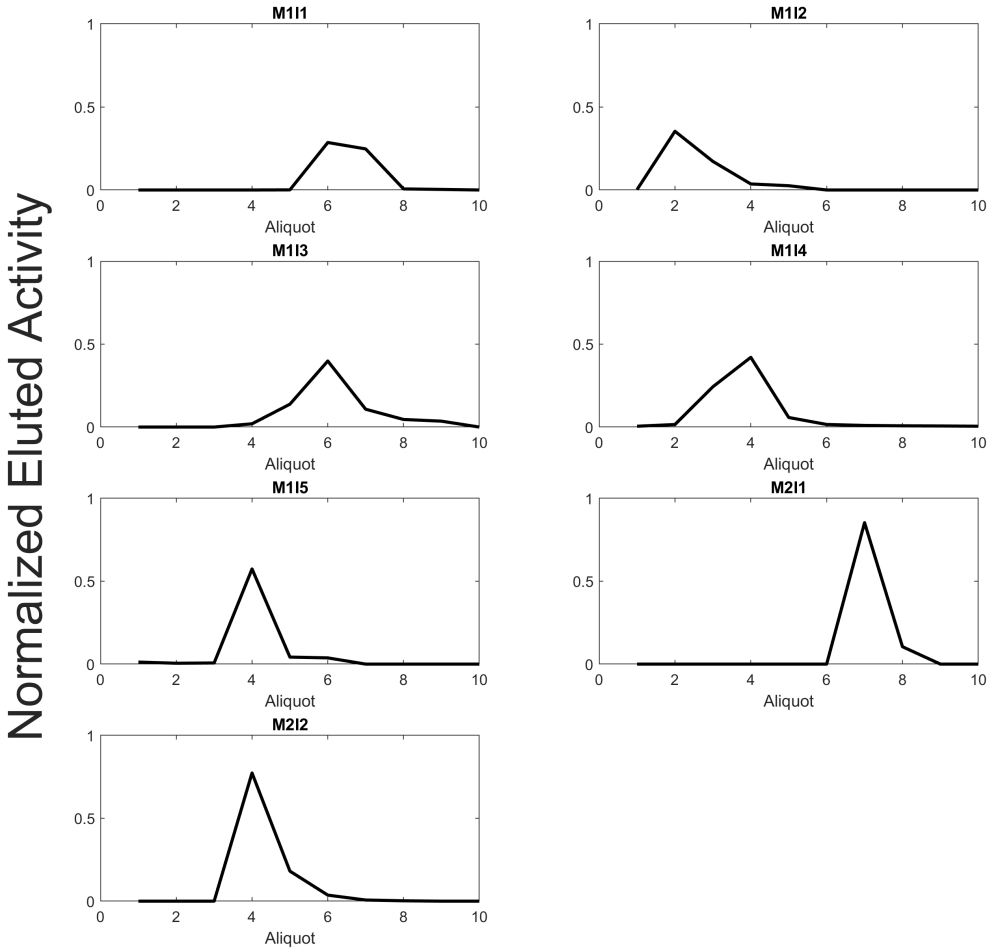

Figure 6.3: Elution profile from Chelex-100 column (Method 1, M1) or AG 50W-x8 column (Method 2, M2) normalized to total radioactivity eluted.

samples after maximum radioactivity. The Chelex-100 column elution yield was 65.6 ± 11.1%, limited both by the selective nature of the column and the number of aliquots collected. The collected volume was typically 1 mL per aliquot. In Iteration 1, a substantial amount

of radioactivity (1.9 mCi) was observed to pass through the Chelex-100 column unbound. Another column was created to see if the radioactivity could be recovered. The starting radioactivity 3 days later was 1.61 mCi. An additional 1.04 mCi was recovered in 7 aliquots; 0.44 mCi remained bound to the second column. In general, relatively low amounts of radioactivity were retained on the column (2-4%) and the amount of radioactivity passing through unbound varied widely (5-27%).

Of the aliquots collected, only the 1-2 samples with highest radioactivity were used to mitigate contaminants and due to the limited volume of the platinum crucible used. After the product was transferred to and baked in the oven, the extracted fraction from the platinum crucible was 79.6 ± 19.3%. This product was then set to reflux. As above, the yield at this point in the procedure is somewhat limited because of the need to restrict scratching of the platinum crucible in order to avoid introducing contaminants. After refluxing, 72.2 ± 24.6% of the radioactivity was removed from the round bottom flask; the residual radioactivity was embedded in or on the flask and could not be easily removed.

After passing the solution through the C-18 cartridge, 47.8 ± 3.7% (n=2) of the radioactivity was eluted in 400 μL of EtOH. Additionally, 19.9 ± 4.9% of the radioactivity passed through the cartridge with the load solution; 12.8 ± 7.8% remained trapped in the cartridge and could not be eluted; and the residual radioactivity was retained in the syringe transferring the radioactivity and could not be further recovered.

In general, some of the lowest step-wise yields of the overall synthesis occurred when ^{48}V was eluted as $NH_4^{48}VO_3$, when the $^{48}VO(acac)_2$ was transferred from the round-bottom flask, and when passing through the C-18 cartridge. In these instances, the loss is partially due to the selective manner in which the compound is transferred in an effort to maximize purity and mitigate potential contaminants.

The length of synthesis varied substantially, from 13 days to 35 days. Due to time required between steps, and time lapsed over the weekend, 13 days was determined to be the minimum

time required for this synthesis. The process could be elongated by many factors, including staff availability, target dissolution time, and difficulties in sample filtration.

6.3.2 Method 2

Due to the length of time required for Method 1, Method 2 was pursued as a quicker alternative.

Target Dissolution

Iteration 1: 2 mL of 6 M H_2SO_4 was added and the target place over a 140°C oil bath. Foils were initially thought to have dissolved in 45 minutes and were only heated for 3.5 h. Upon closer inspection the following day, there were still chunks present in the acid solution. The beaker and transferred target were assayed and the fraction dissolved determined to be 65.5%.

- Target dissolution time: N/A

Iteration 2: 2 mL of 6 M H_2SO_4 was added and the target place over a 150°C oil bath. After 22 hours of dissolution, the foils were observed to be intact and were stirred with a pipette tip in an attempt to break the target into smaller pieces. This was repeated several times over the course of 3-4 hours. At appx. 26 hours of dissolution, the target was observed to be broken into small pieces and pipetted up and down with 2 mL of added water in an attempt to break up the chunks further. The target solution was used in this manner, with pieces left undissolved. The fraction dissolved was determined to be 65.0%. The slower dissolution compared to Iteration 1 is believed to be attributed to scorching or oxidation of the target, not visible for previous targets. The liquid portion of the target solution was used for the next step and the chunks were selectively avoided.

- Target dissolution time: >22 hrs (did not completely dissolve)

Column Separation

The target solution was diluted to 0.4 M and the column conditioned before the target solution was poured into the column. The column resin was orange; as the target solution was passed through, a dark blue/purple band formed at the top. The liquid exiting the column was assayed: no radioactivity passed through unbound. As the eluting solution interacted with the column, it changed from purple to red.

Iteration 1: At first, the bottom layer was still orange, but the red band moved down the column as the eluting solution was passed. The eluted material was clear, with no color tinge. Once the purple band changed completely to red, the solution was collected in 3 mL aliquots (aliquot 7-9); only two aliquots (7,8) had any radioactivity. Overall, 95.8% of the radioactivity was recovered in this step. To reduce the volume, the solution was evaporated with N_2 gas flow and a 50°C oil bath.

Iteration 2: When the column was conditioned with 5 mL water, the eluted solution was grey for this iteration, unlike in Iteration 1 in which it was clear. The purple/red layer did not progress all of the way down the column and instead remained in the top half of the column. The solution was collected in aliquots; 5 of them (4-8) had some radioactivity, while the last aliquot (9) did not, indicating the column was completely eluted. The recovery for this step was 97.64%. The solution was evaporated with N_2 gas flow overnight.

Vanadate Reduction and $^{48}VO(acac)_2$ Formation

Iteration 1: Following 16 hours, the column eluate was shown to have completely evaporated. Subsequently, 20 mL of EtOH, 10 mL of water, and 1 mL of 0.2 M H_2SO_4 was added to the solution and set to reflux overnight. The following day, 2 mL of acetylacetone was added to the sample, then stirred for 40 minutes. The solution was neutralized with a sodium carbonate solution of 28 mg in 175 μL water and allowed to sit for 40 minutes. The sample was filtered via fritted glass filter. Of the approximately 2.3 mCi filtered, only 45 μCi (<2%)

stayed on the frit; the remaining radioactivity passed through and filtration was unsuccessful.
Iteration 2: Following 16 hours, the column eluate was observed to have evaporated completely. Subsequently, 1 mL of EtOH, 0.5 mL of water, and 0.05 mL of 0.2 M H_2SO_4 was added to the solution and set to reflux overnight. After reflux, most of the liquid was observed to have evaporated. The remainder was attempted to be evaporated with vacuum suction, then a N_2 gas flow. Condensation was still visible after several hours, and it was theorized that the liquid visible was sulfuric acid. After several hours of N_2 gas flow, 0.5 mL acetylacetone was added. The RBF was gently shook for several minutes, then left to sit for 30 minutes with gentle shaking approximately every 10 minutes. After 30 minutes, the solution was put under N_2 gas flow in an attempt to evaporate the acetylacetone. The sample was neutralized with a 1 mL solution of 18 mg Na_2CO_3 in 1 mL water. The sample was allowed to sit for 30 minutes.

6.3.3 Sample Filtration

Iteration 1: Filtration via C-18 cartridge was attempted but, due to the large volume of EtOH, it was unsuccessful: 2.12 mCi of the compound passed through, with only 53 μCi (<3%) bound to the cartridge. A fraction of the radioactivity was eluted in two volumes of 300 μL EtOH for a final radioactivity of 35 μCi in 600 μL of EtOH, which was too low of a concentration to use in any further studies. The primary solution had 20 mL EtOH in 33.2 mL of liquid for an EtOH concentration of 60%. In general, the C-18 cartridge only binds the sample if the EtOH concentration is very low (<3%). This step should have been repeated with a lower concentration of EtOH, but the volume would have been prohibitively large (670 mL).
Iteration 2: A C-18 cartridge was conditioned with 6 mL EtOH, followed by 10 mL water. 2.92 mCi passed through, unbound; 0.89 mCi was trapped on the cartridge and subsequently, 0.77 mCi was eluted in 400 μL of EtOH; 0.061 mCi was left in the RBF. The yield of this

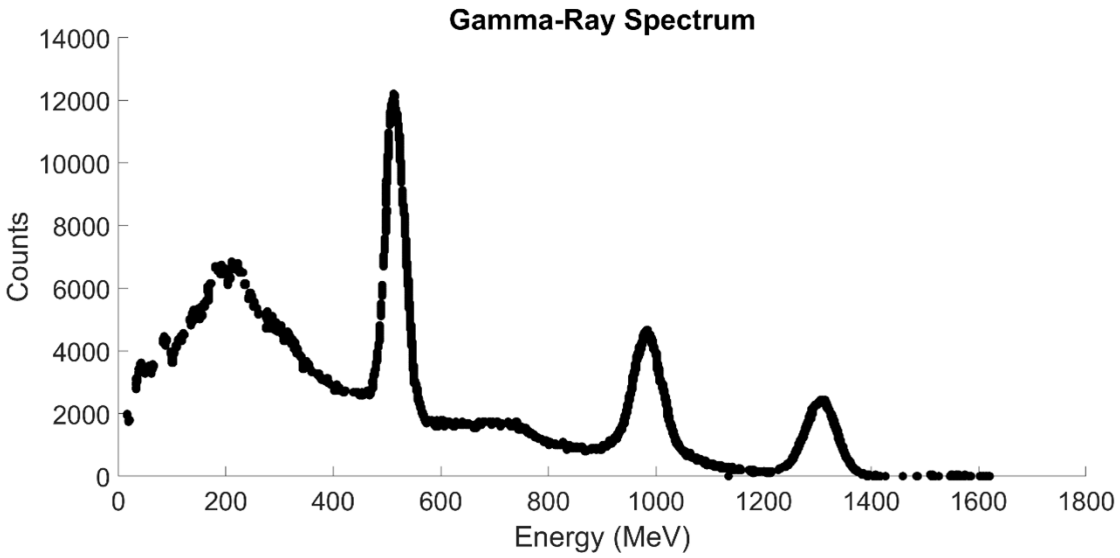

Figure 6.4: Energy spectrum from $^{48}VO(acac)_2$ assay after Method 1, iteration 3 synthesis. Peaks correspond to the expected gamma energies of 511 keV, 984 keV, and 1,312 keV [18]. A NaI(Tl) spectroscopy system was used.

filtration was 19.89%. The eluted sample was evaporated to dryness and reconstituted in 400 μL of saline.

Overall, the synthesis took 4 days. Reductions in the quantity of EtOH in the vanadate reduction step greatly increased the yield.

6.3.4 Vanadium-48-Labeled Vanadyl Acetylacetonate Compound Characterization

Gamma-Ray Spectroscopy

Fig. 6.4 shows the energy spectrum of the radiotracer after chemical separation and synthesis (target 11 from Method 1, iteration 3); this can be compared to Fig. 3.5, which shows the energy spectrum of a foil before chemical separation (target 12 from Method 1 Iteration 4). Note the two gamma-ray spectrums result from two different targets. The photopeaks in Fig. 6.4 correspond to the expected energies for ^{48}V: the positron emission peak of 511 KeV

(first peak) and the two characteristic gamma emission peaks of 984 KeV (second peak) and 1,312 KeV (third peak), respectively. Partially because of the limitations of the NaI(Tl) well counter, the only assay device available for this gamma-ray spectroscopy measurement, the third characteristic gamma peak of ^{48}V at 2,240 Kev (only 2.3%), or any potential remaining radionuclide by-products (all <1% at this time due to decay alone for this iteration) could not be observed [18]. Low-energy peaks, due to backscatter from the lead, are visible in the spectrum but are not visible in the digital version shown herein.

Estimates of the Remaining Contaminants

Tables 6.3 and 6.4 show the expected contaminants that could remain in the $^{48}VO(acac)_2$ radiotracer solution at the end of synthesis (EOS) compared to the radioisotopes present when assayed at the start of synthesis (SOS). Based on the decay of the isotopes and synthesis

			Radioisotope				
		A [mCi]	^{48}V	^{47}Sc	^{44m}Sc	^{44g}Sc	^{43}Sc
$t_{1/2}$ [h] →			383.4	83.8	58.6	4.0	3.9
CS [mB]→			126.7	3.4	1.2	3.5	3.4
M1,I4	A SOS [mCi]	7.2	6.2	0.4	0.2	0.1	0.1
	Fraction [%]		85.8	5.7	2.3	1.5	1.4
	A EOS [mCi]	1.4	1.3	0.0	0.0	0.0	0.0
	Fraction [%]		97.4	0.02	0.0	0.0	0.0
M1,I5	A SOS [mCi]	8.2	7.6	0.4	0.1	4.2E-07	3.0E-07
	Fraction [%]		92.5	5.1	1.7	0.0	0.0
	A EOS [mCi]	4.3	4.3	0.03	0.003	0.0	0.0
	Fraction [%]		98.2	0.6	0.08	0.0	0.0
M2,I1	A SOS [mCi]	8.5	7.7	0.5	0.2	1.2E-05	9.0E-06
	Fraction [%]		91.2	6.0	2.2	0.0	0.0
	A EOS [mCi]	6.8	6.5	0.2	0.06	0.0	0.0
	Fraction [%]		95.2	3.3	0.9	0.0	0.0

Table 6.3: Half-life, cross section (CS) at 18 MeV, and estimated fraction and radioactivity (A) of ^{48}V and $^{43,44m,44g,47}Sc$ radioisotopes present at SOS and EOS for Method 1, Iterations 4,5 and Method 2, Iteration 1. All values under the 'Radioisotope' column are calculated using Eqn. 3.1.

timeline, the most active contaminant at EOS would be ^{46}Sc for Method 1 Iterations 4 and 5;

			Radioisotope			
		A [mCi]	^{45}Ti	^{47}V	^{46g}Sc	^{48}Sc
$t_{1/2}$ [h]→			3.1	0.5	2011.0	43.7
σ [mB]→			13.5	85.6	3.8	0.05
M1,I4	A@SOS [mCi]	7.2	0.2	0.0	0.04	0.01
	Fraction [%]		2.5	0.0	0.6	0.1
	A@EOS [mCi]	1.4	0.0	0.0	0.03	0.0
	Fraction [%]		0.0	0.0	2.3	0.0
M1,I5	A@SOS [mCi]	8.2	$1.4\text{x}10^{-8}$	0.0	0.05	0.005
	Fraction [%]		0.0	0.0	0.6	0.06
	A@EOS [mCi]	4.3	0.0	0.0	0.05	$3.6\text{x}10^{-5}$
	Fraction [%]		0.0	0.0	1.1	0.0
M2,I1	A@SOS [mCi]	8.5	1.4^{-6}	0.0	0.05	0.01
	Fraction [%]		0.0	0.0	0.6	0.09
	A@EOS [mCi]	6.8	0.0	0.0	0.05	0.0
	Fraction [%]		0.0	0.0	0.7	0.02

Table 6.4: Half-life, cross section at 18 MeV, and estimated fraction and radioactivity (A) of ^{45}Ti, ^{47}V, and $^{46g,48}Sc$ isotopes present at the SOS and EOS for Method 1 Iterations 4,5 and Method 2 Iteration 1. All values under the 'Radioisotope' column are calculated using Eqn. 3.1.

without separation procedures, it would account for 1.1-2.3% of the observed radioactivity and has 889 keV and 1,121 keV gamma-ray emissions. ^{47}Sc would also be present at 0.02-0.6% of the radioactivity and emits a 159 keV gamma-ray. For the short, 4-day synthesis of Method 2, Iteration 1, ^{47}Sc would be the most prominent contaminant (3.3%), followed by ^{44m}Sc (0.9%), emitting a 272 keV gamma-ray, then finally ^{46}Sc (0.7%) [18]. These values are the fraction of each radioisotope due to decay only and assume no chemical separation.

Of these potential contaminants, none are visible in Fig. 6.4, either through absence of a photopeak or due to a photopeak in a similar energy region, and through absence of any apparent additive peaks (due to the accuracy and resolution of the counting system used). This result indicates that the radioisotope separation steps were effective. Other contaminants would include titanium isotopes; these isotopes are mainly non-radioactive and would not appear in the gamma-ray spectrum, with the exception of short-lived ^{45}Ti, which would have mostly decayed by the end of synthesis (as indicated in Tables 6.3 and 6.4).

In general, Tables 6.3 and 6.4 shows the estimated upper limit of the relative abundance of the radioisotopes remaining in the final compound after the end of synthesis. It is shown that ^{48}V is at least 95-98% of the total radioactivity; in reality, since there were multiple steps to reduce remaining contaminants, the actual amount of ^{48}V is likely greater than 99%.

HPLC Characterization

Method 1: The HPLC procedure was developed using 40-60% MeCN-water and 0.1% TFA over 15 minutes as described in Chapter 5. $VO(acac)_2$ is best detected spectrophotometrically at 320 nm [46]. Fig. 6.5A shows that the retention time for the commercial $VO(acac)_2$ is 1:50. The HPLC of radioactive $^{48}VO(acac)_2$ exhibited a retention time of 1:48, corresponding to the

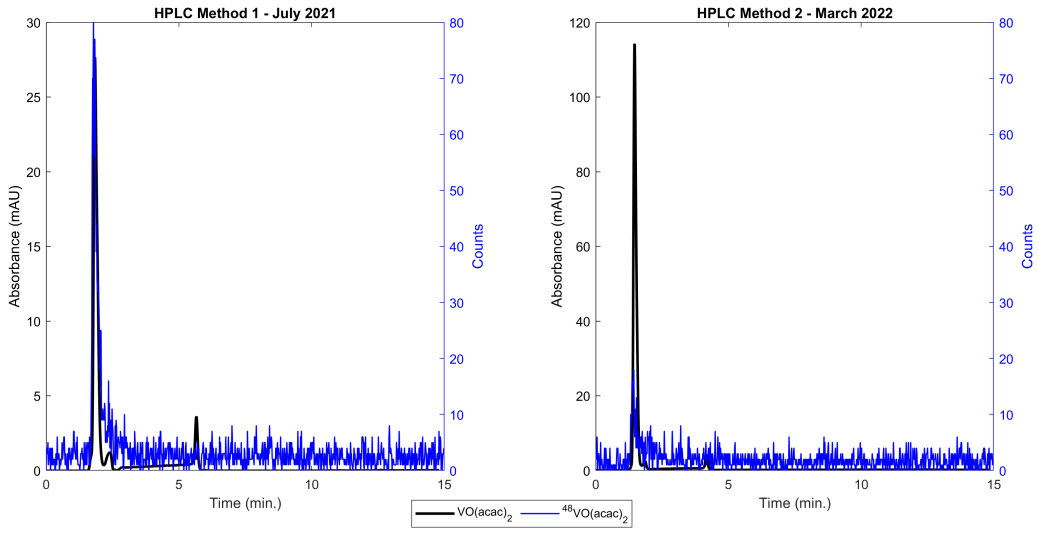

Figure 6.5: HPLC of $^{48}VO(acac)_2$ (blue line) and non-radioactive $VO(acac)_2$ (black line, 320 nm). Left, A: $^{48}VO(acac)_2$ synthesized using Method 1; Right, B: $^{48}VO(acac)_2$ synthesized using Method 2. The vanadyl complexes were dissolved in 100% ethanol and a 40-60% MeCN-water in 0.1% TFA mobile phase was used.

$VO(acac)_2$ absorption peak at 320 nm. No other peaks indicating radioactivity were observed. The corresponding retention times, as well as the absence of other peaks of radioactivity, indicate that $^{48}VO(acac)_2$ was synthesized.

Method 2: As in Method 1, an HPLC procedure using 40-60% MeCN in 0.1% TFA was

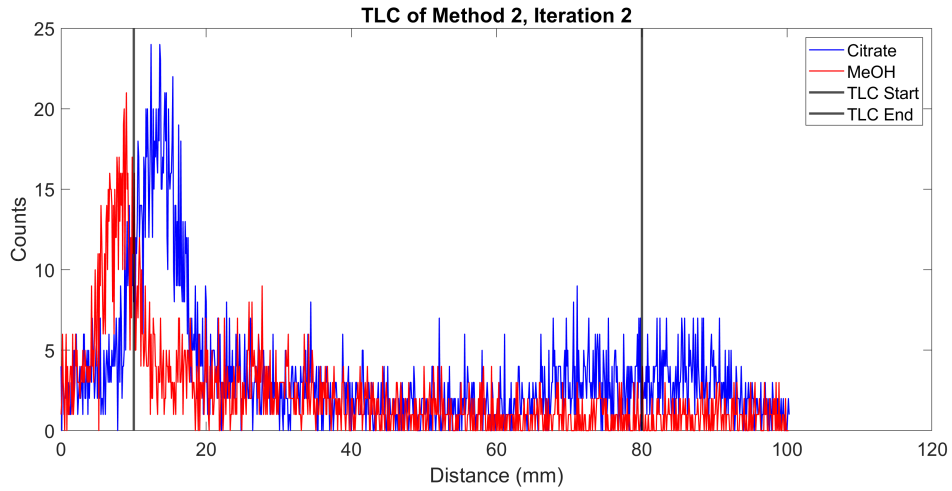

Figure 6.6: TLC of $^{48}VO(acac)_2$ in 0.1 M sodium citrate (blue) and 1:1 methanol-1 M ammonium acetate (red) from Method 2, Iteration 2. Black lines denote where the radiotracer started (origin, at left) and how far the mobile phase was allowed to progress (solvent front, at right).

used; here, a 1.5 mL/min. flow rate was used. A spike sample was prepared in which the radiotracer is mixed with the cold, standard compound to observe if the retention time for the UV and radiation signals are the same given the same column conditions. Fig. 6.5B shows the resulting HPLC. The retention time for the $^{48}VO(acac)_2$ was 1:26 and for $VO(acac)_2$ was 1:28.

TLC Characterization

TLC was done with $^{48}VO(acac)_2$; the results are shown in Fig. 6.6. Un-reacted ^{48}V should not be mobile in 1:1 methanol-1 M ammonium acetate or should move in 0.1 M sodium citrate. However, as seen in Fig. 6.6, results of this radiotracer study were therefore inconclusive: if the compound was mobile in 50% methanol, then it should not be mobile in citrate, or vice versa, for free ^{48}V.

ICP-MS Profile

Table 6.5 shows the isotopic results of ICP-MS analysis of several samples taken during the synthesis of Method 1 Iteration 4. Samples had to decay before assay so they could

Sample name	Ca [μg]	Ti [μg]	V [μg]	Fe [μg]	Co [μg]	Pt [μg]
1. Dissolved foil	3.03	3.24	$2.82\text{x}10^{-3}$	1.82	$2.30\text{x}10^{-3}$	$<1.95\text{x}10^{-4}$
2. V48 in water	1.34	0.11	$2.09\text{x}10^{-3}$	<0.04	$<1.16\text{x}10^{-4}$	$1.19\text{x}10^{-3}$
3. Chelex Column wash	2.39	0.04	$2.79\text{x}10^{-3}$	<0.04	$<2.62\text{x}10^{-4}$	$1.01\text{x}10^{-3}$
4. Chelex column eluate (0.5 MCl)	2.31	$<3.34\text{x}10^{-3}$	$2.99\text{x}10^{-3}$	<0.08	$<2.40\text{x}10^{-4}$	$<7.47\text{x}10^{-4}$
5. Before C18 Cartridge	4.07	$<3.34\text{x}10^{-3}$	0.02	<0.12	$8.14\text{x}10^{-3}$	$1.71\text{x}10^{-3}$
6. C-18 Column Wash	3.50	$<1.67\text{x}10^{-3}$	$1.45\text{x}10^{-3}$	<0.04	$4.33\text{x}10^{-4}$	$<2.71\text{x}10^{-4}$
7. After C-18 Cartridge	3.80	$<3.34\text{x}10^{-3}$	0.02	<0.08	0.02	$2.91\text{x}10^{-3}$

Table 6.5: Amount of ^{48}V and other contaminants in the solution at various stages of synthesis.

be handled; the time between end of synthesis and assay was 3 months and 3 weeks. The amounts of each isotope are relative; the exact concentration could not be calculated.

Sample 1 is the profile of the dissolved foil. The predominate products are calcium, which is a decay product of ^{43}Sc and $^{44m+g}Sc$, and titanium, which in addition to being the original material of the foil is a decay product of all activated vanadium isotopes, $^{46m+g}Sc$, and ^{47}Sc. Iron is also present at approximately half the amount of calcium and titanium; this could potentially be contributed to some contaminant in the foil or to a tool used to handle the foil, such as the tweezers used to remove the foils from the beamstop. Iron could also be an impurity of the platinum crucible used. Vanadium is present at approximately 1000x less than the calcium or iron; stable vanadium is also a decay product, as detailed in Table 3.1.

Sample 2 is the profile of the supernatant extracted after centrifugation that was then

introduced to the Chelex-100 column; in theory, this step should separate titanium hydroxides and scandium isotopes in the precipitate. As in Sample 1, the predominante material is calcium, indicating the separation of scandium isotopes (which would have decayed to calcium) was not completely effective. The quantity of titanium (reduced by a factor of 30 compared to Sample 1) was substantially lower, while the amount of vanadium was relatively stable (reduced by a factor of 1.3). The quantity of Iron was also much lower (reduced by >45x).

In looking at samples 2-4, the amount of vanadium increases, while the amount of titanium decreases substantially: the amount of vanadium is being maintained as the amount of titanium is being filtered out due to the Chelex-100 column. The column does not appear to be as effective in separating the calcium, which saw some increase in the samples.

Samples 5-7 are the profile of the sample before, during, and after filtration with a C-18 cartridge. The amount of titanium and vanadium before and after the cartridge stays the same, indicating that the titanium was unaffected by the filter. The amount of calcium is relatively constant.

Overall, the predominant contaminant present is calcium, introduced only as a byproduct of short-lived scandium isotopes. Future work should focus on means to separate out calcium more effectively. In preparing the final solution, a precipitate was often present; this could be due to the calcium, which is known to form precipitates in some solutions .

6.4 Discussion

6.4.1 Method 1

While the earlier iterations had higher overall yields, they also had fewer filtration measures. These measures tended to decrease the radioactivity by approximately half (49.5 ± 11.2%). Although HPLC or ICP-MS analyses were not done for these earlier samples, filtration typically removes impurities or unbound radioisotopes, resulting in a radiotracer with higher specific

radioactivity and fewer contaminants. Particularly, the C-18 cartridge binds $VO(acac)_2$ and allows many other materials to pass, including unbound vanadium. Therefore, the eluted product is likely to have a higher purity and specific activity. In some iterations (Method 1 Iteration 3, Method 2 Iteration 1), a fritted glass filter was attempted; such a filter can be used in production of non-radiolabeled $VO(acac)_2$ [82] [15]. However, the filter did not trap the radioactivity, most likely because of the small quantity of the compound, which was unable to crystallize and form a larger structure that could be trapped on the frit. Additionally, in Method 1 Iteration 2, an OnGuard II M cartridge was used for purification; this cartridge has a high selectivity for transition metals (such as vanadium) and can be used to concentrate or remove transition metals [88]. However, no radioactivity was bound to the cartridge. Of the filters used herein, the C-18 cartridge was found to be the most effective. Future studies could explore the low yield of the C-18 cartridge; namely, the profile of the compound that is trapped to the cartridge compared to the compound that can be eluted. Additionally, alternative filtration cartridges could be considered that do not require such a limited concentration of EtOH, as it is a useful solvent in extracting the compound from the round-bottom flask and forming the compound in the alternative synthesis outlined in Method 2.

The target was dissolved in the least time when using excessive concentrated HF (Iteration 1) and a larger volume of 6 M H_2SO_4 (Iteration 5). While the dissolution via HF was effective, there was some concern that its use could affect the downstream chemistry, preventing compound chelation and potentially facilitating precipitates in the solution. As demonstrated in iterations 2-4, the concentrated H_2SO_4 alone was not sufficient to dissolve the target within a reasonable timeframe. The 6 M H_2SO_4 is thought to be more effective due to the volume of acid used – by using 1.5 mL of liquid compared to 0.3 mL (as with the concentrated H_2SO_4), a larger portion of the target is in contact with the acid. In Iteration 4, a lower volume of the 6M H_2SO_4 was used (increments of 0.6 mL) and subsequently resulted in a

dissolution time of 6 days. This latter iteration indicates that the quicker dissolution time can be attributed to the increased volume more than the lower molarity. Dissolution was also undoubtedly helped by the addition of higher heat, as used in Iteration 5 and (to a lesser extent) Method 2, Iteration 1. Both syntheses had higher oil bath temperatures (170°C and 140°C, respectively) and had relatively short dissolution times: the Iteration 5 target dissolved completely within a day, while the Method 2, Iteration 1 target was 2/3 dissolved within 4 hours.

In general, the target fusion was observed to be successful, distinguished by the liquid sample becoming a solid mass. In one iteration (Iteration 1), the sample was heated for less time and observed to be free-flowing, indicating the fusion had not been completed. In subsequent iterations, a longer fusion time was used. The prolonged heating period should not adversely affect the compound at this stage.

While the precipitate from the centrifuge was not analyzed, it is theorized to contain titanium oxides, calcium compounds, and scandium isotopes in the precipitate. This is logical; titanium and calcium oxides tend to be white, and the precipitate was white. In general, little radioactivity was retained in this precipitate: the yield of radioactivity recovered from the platinum crucible and usable for transfer to the cation exchange column was greater than 73%.

For each iteration, the elution from the Chelex-100 column was one of the lowest step-wise yields. This low yield has a couple of potential explanations:

- The vanadium was not completely in the 4+ form. If the vanadium was in another valency state (i.e. V^{5+} or V^{3+}), then it would not bind to the Chelex-100 column [84]. When the target is dissolved, it is thought to be in the V^{4+} form [104]. If the vanadium were the wrong form, the radioactivity would not bind to the column and would instead appear in the column wash.

- The radioactivity is not due to ^{48}V. Tables 6.3 and 6.4 indicate that the ^{48}V should

account for >85% of the radioactivity; at the time of separation via Chelex-100 column, the fraction is likely higher. In addition to vanadium, other transition metals (including scandium isotopes) could bind the column but may not be eluted by the ammonia solution. If this were the case, the radioactivity could pass through unbound (if not a transition metal) or could stay on the column after elution (if a non-vanadium transition metal). This could contribute both to radioactivity in the column wash that passed through unbound, and radioactivity on the column that could not be eluted or removed.

- In most iterations, the column was only eluted to observe the few points beyond the elution peak. Therefore, more radioactivity could potentially have been eluted, though it would likely have been marginal compared to the radioactivity already eluted.
- The ^{48}V is not completely eluted by the ammonia solution.
- Too much column resin was used relative to the amount of radiotracer.

The amount of column resin used was determined based on the mass of the entire titanium foil target. While the portion of the sample passing through unbound was high for Iteration 1, it was much lower (<10% of the sample) for the latter iterations even though less resin was used (3 g compared to 4.5 g for the first 2 iterations). This could indicate that the compound itself bound to the column more easily. In general, it was difficult to assess how much compound was trapped on the column after elution due to the irregular shape of the column. The effect of using more or less resin could be explored in the future; using less resin would result in a higher flow rate but worse separation, while more resin would increase the flow rate but improve separation. Without some sort of analysis of the samples before and after the column, it is difficult to assess the tradeoff. Therefore, samples could be collected and analyzed at different column heights (amounts of resin) to observe the contaminant profile with increasing column height.

The amount of product set to reflux had a large standard deviation; the quantity varied

amongst the iterations. For some iterations, the compound was easier to extract from the platinum crucible than other iterations; sometimes, the compound could easily be extracted with gentle scratching, while other times it was difficult to extract even with sonication. In the latter iterations, an effort was made to minimize scratching of the platinum crucible to decrease potential contaminants. In some iterations, the compound was heated for a longer period of time. This could also have contributed to the difficulty in removing it from the crucible. The tool used to scratch the compound out of the crucible could also have affected the yield: in early iterations, a metal spatula with Teflon coating was used, while, in latter iterations a pipette tip was used.

The percent removed from RBF also varied widely, likely due to drying of the compound on the RBF or the selective nature in which it was extracted. In general, material dried to the sides or neck of the RBF is difficult to extract due to its position.

6.4.2 Method 2

While Method 2 was a much quicker alternative to Method 1, it would require further iterations to fine-tune the procedure and confirm its validity. The direct filtration of the dissolved target solution was much more succinct than the Method 1 filtration and the visual ques were useful in determining when to proceed to the next step; subsequently, the radioactivity collected per 1 aliquot was the highest for this method (Fig. 6.3). This method also had the highest column-activity extraction of any iteration (95.8%).

6.4.3 HPLC Analysis

The HPLC peaks of non-radiolabeled and $^{48}VO(acac)_2$ align well in Fig. 6.5, indicating that the same compound is analyzed with both assays and that the correct compound is synthesized via Methods 1 and 2. In Method 2, Iteration 1 in which the solution could not be evaporated, HPLC analysis showed two peaks, one of which has the same retention

time for UV and radiation signal, and the other of which does not. This indicates that some transformation occurred for the $VO(acac)_2$ compound in this iteration. In subsequent syntheses (Iteration 2), care was taken to evaporate the entire solution and subsequently, only one peak was observed. It was concluded that this evaporation step is important in maintaining radiotracer integrity.

6.5 Conclusion

Two procedures were developed to synthesize $^{48}VO(acac)_2$. Method 1 required a minimum of 13 days, while Method 2 required only 4 days. Gamma-ray spectroscopy indicates that the correct radioisotope was generated due to the lack of visible contaminant peaks within the limits of the NaI(Tl) system used. HPLC analysis of the radiotracer and comparison to non-radiolabeled $VO(acac)_2$ indicated that $^{48}VO(acac)_2$ was synthesized via Method 1 as well as Method 2. Future work should seek to increase the yields in Method 2, primarily in the target dissolution step, and quantify the contaminants produced.

CHAPTER 7

MOLECULAR IMAGING AND KINETIC ANALYSIS STUDIES USING VANADIUM-48-LABELED VANADYL ACETYLACETONATE

7.1 Introduction

This work was motivated by promising results using $VO(acac)_2$ to differentiate malignant tissues in studies by collaborating MRI researchers. On a cellular level, accumulation of $VO(acac)_2$ into the intracellular space in Caco-2 colorectcal cancer cells was demonstrated via MRI by Mustafi et al. [71]. A later study showed that $VO(acac)_2$ accumulates in the intracellular space of colonic adenomas using ultra-high resolution x-ray fluorescence microscopy [73]. On an *in vivo* level, $VO(acac)_2$ was shown to accumulate in xenograft prostate cancer tumors via MRI, while levels of $VO(acac)_2$ in normal tissue were determined to be negligible, leading to twice as much signal attributed to cancerous tissues compared to muscle tissues [72]. These studies indicate that $VO(acac)_2$ could be used to differentiate cancerous tissues from normal, non-malignant tissues. Additionally, the long half-life of ^{48}V means that $^{48}VO(acac)_2$ could be used for longitudinal studies and monitoring of treatment or disease progression, motivating further studies for this compound as a radiotracer.

In this current study, human colorectal carcinoma cell line HCT-116 and human colonic adenocarcinoma cell line HCA-7 were used. While the aforementioned studies did not use these particular cell lines, those studies did demonstrate uptake of $VO(acac)_2$ in a colon cancer model. Additionally, these types of cancer (colorectal and colon, respectively) were chosen for further study herein due to the potential utility of $VO(acac)_2$ in monitoring and managing this disease. Ulcerative colitis, a chronic inflammation of the bowel, is increasingly recognized as a component of colorectal cancer tumorigenesis [32]. Thus, $VO(acac)_2$ could potentially be used to stage and monitor colon and colorectal cancer progression and potentially facilitate

earlier treatment of malignancy.

HCT-116 is a fast-growing model of colorectal cancer. It is reported to have a doubling time of approximately 20 hours. In a study in which nude mice were inoculated with $5x10^6$ cells subcutaneously, approximately half of animals showed tumors after 16±5 days; when inoculated with 10^7 cells, approximately half of animals showed tumors after 6±1 days [13]. This quick doubling time and short latency period can be useful for *in vitro* and *in vivo* studies by making cells and animals ready for use more quickly.

HCA-7 is a more slowly growing model of colon cancer. It is reported to have a doubling time of approximately 36 hours [56]. Depending on the passage number and subpopulation, xenograft tumors were reported to appear between 14 and 194 days after subcutaneous inoculation of 10^7 cells, with the original cell line showing tumors 67.7±13.4 days after inoculation [68]. This slower growth rate, both for cells and xenograft tumors, can complicate the timing of imaging studies, particularly because the $^{48}VO(acac)_2$ target irradiation and synthesis takes at least 2 weeks. However, slow growing tumors may facilitate longitudinal studies of disease progression.

7.1.1 Kinetic Modelling

Using time-activity curves and biodistribution data of various organs and tissues from the animal imaging, kinetic modelling can be done to extract uptake and clearance parameters. A one-tissue compartment model (1TCM) describes a system in which the tracer can be taken up from the arterial plasma into only one tissue. A two-tissue compartment model (2TCM) has two tissue compartments that are linked to each other and therefore, have an uptake rate between them. Compartmental models assume underlying physiological processes are in steady state for the duration of the study so that rate constants do not vary [16]. They assume each compartment is homogeneous. An input function for the blood plasma must be measured in some manner to quantify the activity. Methods to do so include: (1) direct

blood sampling; (2) using a reference region; (3) an image-derived input function; and (4) a population-based input function [103] [75]. Of these methods, method 2 was used in this study due to the ability to distinguish a reference tissue and limitations in the other methods. While method 1 is likely the most direct quantification of blood radioactivity concentration, it can be difficult to accurately assess in mice due to their low blood volume. Method 3 is limited by the ability to delineate a suitable region of interest (ROI) in the heart, which can be difficult to accomplish within the spatial constraints of pre-clinical PET. Method 4 requires direct blood sampling (similar to method 1) of a population of similar subjects in order to obtain an input function that can be applied to other subjects and therefore raises the same problems as method 1.

$VO(acac)_2$ has not previously been analyzed via kinetic modelling; therefore, it is unknown whether it is a 1TCM or a 2TCM or whether it is reversibly bound, meaning that after it enters a tissue, it can exit the tissue and return to the plasma, or irreversibly bound, meaning that once it enters a tissue from the blood it cannot exit. Here, three modelling methods were considered to analyze the data. $VO(acac)_2$ was assumed to be reversibly bound and all modelling methods used are for reversibly bound radioatracers.

Logan Graphical Analysis Using a Reference Tissue

Logan graphical analysis [64] [65] evaluates the kinetic uptake by plotting the activity in a ROI over time against the activity in an input function over time. The resulting slope and intercept can then be interpreted as kinetic binding parameters.

A 1TCM can be described mathematically in Eqn. 7.1, where C_R refers to the radioactivity concentration in a ROI, C_p refers to the radioactivity in plasma due to unmetabolized or unbound radioligand, K_1 is the rate of uptake from the blood plasma to a tissue, and k_2 is the rate of release from the tissue back to the blood plasma. For a 1TCM, these parameters are quantified together as $DV = \frac{K_1}{k_2}$.

$$\frac{dC_R(t)}{dt} = K_1 C_p(t) - k_2 C_R(t) \tag{7.1}$$

Logan analysis can be defined in Eqn. 7.2, where $C_R(T)$ denotes that the function has been integrated over the time of the imaging, T. DV, described above, is the distribution volume, a function of the free receptor concentration, found as the slope of the plot. 'Int' is the intercept of the plot; the plot is determined to be linear when 'int' is constant.

$$\frac{\int_0^T C_R(t)dt}{C_R(T)} = DV\frac{\int_0^T C_p(t)dt}{C_R(T)} + int \tag{7.2}$$

When a reference tissue is used in place of a plasma input function, Logan analysis is described using Eqn. 7.3. With the addition of the above variables, C_{Ref} is the concentration in the reference tissue, $\bar{k_2}$ is the average of k_2 over several samples, DVR is the ratio of the DV in the tissue of interest to the DV in the reference tissue (DV_{Ref}), and int$'$ is again a constant [75].

$$\frac{\int_0^T C_R(t)dt}{C_R(T)} = DVR\frac{\int_0^T C_{Ref}(t)dt + (C_{Ref}(T)/\bar{k_2})}{C_R(T)} + int' \tag{7.3}$$

Simplified Reference Tissue Model (SRTM)

SRTM is a modelling method that does not require an arterial input function and can be solved, or converge to a solution, more quickly than other methods [59].

SRTM requires a reference tissue devoid of receptors that can be modeled by a 1TCM. It assumes that (1) the distribution volume is the same for the tissue of interest and the reference tissue and (2) for the receptor-rich tissue of interest, it is difficult to distinguish specific and non-specific binding such that the TAC can be fitted to a 1TCM with uptake rate constant $k_{2a} = \frac{k_2}{(1+BP_{ND})}$, where BP_{ND} is the ratio at equilibrium of specifically bound radioligand to that of non-displaceable radioligand. This assumption may not be valid and if

so, means that the BP_{ND} estimates calculated will be biased. BP_{ND} and DVR are related according to Eqn. 7.4, where DV (above) is the distribution volume of a tissue of interest and DV_{Ref} is the distribution volume of a reference tissue.

$$DVR = \frac{DV}{DV_{Ref}} = BP_{ND} + 1 \tag{7.4}$$

SRTM can be described mathematically using Eqn. 7.5

$$C_R(t) = R_1 C_{Ref}(t) + R_1(k_2' - k_{2a})e^{-k_{2a}t} * C_{Ref}(t) \tag{7.5}$$

where C_R refers to the concentration of the tissue of interest; $R_1 = \frac{K_1}{K_1'}$, the relative amount of radioligand delivered to the tissue; C_{Ref} refers to the concentration in the reference tissue; k_2' is the clearance rate constant from the reference region to plasma; and k_{2a} can be generally described as the apparent, overall rate constant for transfer from the specifically-bound compartment to plasma [59].

Ichise's Multilinear Reference Tissue Model (MRTM)

MRTM assumes there is an equilibrium time, t^*, after which the linear relation holds. It is reported to have low bias and variability [49], advantageous when finding parameters for which there is not a comparison in the literature.

MRTM can be described mathematically using Eqn. 7.6, where where $C_R(t)$ is the concentration for a region of interest, $C_{Ref}(t)$ is the concentration of a region without receptors, DV and DV$'$ are the total distribution volumes of $C_R(t)$ and $C_{Ref}(t)$, and b is a constant.

$$C_R(T) = -\frac{DV}{DV'b}\int_0^T C_{Ref}(t)dt + \frac{1}{b}\int_0^T C_R(t)dt - \frac{DV}{DV'k_2'b}C_{Ref}(T) \tag{7.6}$$

Each of the integral coefficients in Eqn. 7.6 can be solved using multi-linear regression, as shown in Eqn. 7.7.

$$\gamma_1 = -\frac{DV}{DV'b} \qquad \gamma_2 = \frac{1}{b} \qquad \gamma_3 = -\frac{DV}{DV'k_2'b} \tag{7.7}$$

From these values, binding potential and k_2' can be calculated according to Eqns. 7.8 and 7.9, respectively.

$$DVR = -(\frac{\gamma_1}{\gamma_2}) = -(-\frac{DVb}{DV'b}) = \frac{DV}{DV'} \tag{7.8}$$

$$k_2' = \frac{\gamma_1}{\gamma_3} \tag{7.9}$$

7.2 Methods

7.2.1 In Vitro Cellular Studies

In vitro studies were conducted to examine radiotracer uptake on a cellular level. Colon and colorectal cancer cell lines HCA-7 and HCT-116, respectively, were used [13] [56]. Cells were grown in Dulbecco's Modified Eagle Medium (DMEM) with 10% fetal bovine serum (FBS) and 1% penicillin-streptomycin (P/S). FBS is used to stimulate cellular growth and contains components necessary for cell proliferation, including hormones, vitamins, and growth factors [99]. P/S is used to prevent bacterial contamination in the cell culture. Cells were grown over the course of approximately 1-3 weeks before use for *in vitro* studies.

The day before cell studies, approximately 10^5 HCA-7 and HCT-116 cells per well were washed and plated into 24-well plates (diameter: 14 mm each). Cells were incubated in 0.2 mL of cell culture media containing 10% FBS and no P/S.

The day of the study, the radiotracer solution (in 100% saline) was prepared by serial dilution in DMEM media (no FBS or P/S) such that the concentration of the incubation solution was 2.0 μCi/0.2 mL, 1.0 μCi/0.2 mL, 0.5 μCi/0.2 mL, 0.25 μCi/0.2 mL, 0.125

μCi/0.2 mL, and 0.0625 μCi/0.2 mL. These levels of radioactivity correspond with 0.0075, 0.015, 0.03, 0.06, 0.12, and 0.24 nM.

Three wells were incubated in each activity level; an additional three wells per plate were incubated in 2.0 μCi/0.2 mL and 10 μL of 1 mg/mL non-labeled $VO(acac)_2$ in EtOH (an EtOH concentration of 5%) for competition studies; an additional three wells per plate were not incubated in any solution and were later trypsinized to count the number of cells present.

The cells were incubated in the radiotracer solution for 2 hours at 37°C. After 2 hours, 1 plate of each cell line was washed with phosphate buffer solution (PBS) twice, then lysed by 10 minute incubation in NaOH. One plate per cell line was washed twice with culture media, then incubated in culture media for another 2 hours. At the end of two hours, the cells were washed with PBS and incubated in glycerine for 10 minutes. The glycerine solution was collected, and the cells were subsequently incubated in NaOH for 10 minutes; this solution was then collected.

An aliquot of each radioactivity level (0.0625-2 μCi) was assayed separately via well counter and gamma counter to find the relation between count rate recorded and radioactivity.

All cells were assayed via the Perkin Elmer Wizard^2 Automatic Gamma Counter.

Variations in Studies

The number of cells plated per dish varied per study, from 0.2-5x10^5 cells per dish. This is due to the number of wells used as well as the number of cells cultured and ready for use at the time of study. All data (including cell uptake curves and internalization studies) were normalized to the number of cells plated unless specified.

In earlier studies, HCA-7 or HCT-116 cells were plated into 35 mm dishes; this larger diameter was feasible when fewer samples were assessed. Additionally, in early studies as the radiotracer was developed, $^{48}VO(acac)_2$ solution was prepared by diluting in 50% DMSO (dimethyl sulfoxide) solution and culture media (no P/S or FBS).

Variable levels of radioactivity were assessed in the studies, based on the amount of radioactivity available and the gamma counter used; the level of radioactivity was adjusted in subsequent studies based on experience and results from preceding studies. In some studies, the radiotracer solution was prepared at concentrations from 0.03 nM to 0.97 nM. For these studies using both cell lines, the solution was added to the cells in 1 mL of culture medium at radioactivity levels of 0.25, 0.5, 1, 2, 4, and 8 μCi (corresponding to 0.03, 0.06, 0.12, 0.24, 0.48, and 0.97 nM, respectively). As with later studies, the cells with $^{48}VO(acac)_2$ were incubated at 37°C for 2 hours, then washed with culture medium (no P/S or FBS). In some early studies, cells were trypsinized and collected for radioactivity assay via gamma counter to measure the $^{48}VO(acac)_2$ cellular uptake. Three samples were assayed per radioactivity level.

7.2.2 In Vivo Animal Studies

HSD athymic female nude mice were acquired from Harlan-Envigo and inoculated with 1-5x10^6 HCA-7 or HCT-116 cells in the right hind limb. Tumors were allowed to grow for 1.5-6 weeks until a tumor volume between 100-1000 mm^3 was reached. Tumors were measured manually using a caliper: the longest portion of the tumor (length) and the dimension perpendicular to it (width) were measured. The volume was calculated using Eqn. 7.10, where V is the tumor volume, l is the tumor length, and w is the tumor width.

$$V = \frac{l \cdot w^2}{2} \tag{7.10}$$

Prior to imaging studies, mice were anesthetized and injected intravenously via tail vein with 30-100 μCi of $^{48}VO(acac)_2$ radiotracer diluted in 50% DMSO and saline for mice 1-7; for mice 8-10, the radiotracer was prepared in 100% saline and a catheter was used. Peak tracer uptake time was chosen as four hours based on the literature [72]. Animals were

imaged for four hours via Molecubes β-Cube PET system; a CT image was obtained after PET imaging. After four hours, the animals were sacrificed. Biodistribution studies were conducted by excising selected tissues. All radioactivities were assayed via gamma counter.

Time-activity curves were obtained using VivoQuant (Invicro, Boston, MA). Regions of interest (ROIs) were manually selected per animal based on the CT image and confirmed with the PET image to extract the activity concentrations in the organ as a function of time. Here, the time-activity curve shows the percent of the injected dose per volume of tissue (%ID/mL). This is calculated according to Eqn. 7.11, where c_i is the concentration of radioactivity in a given tissue (decay corrected) and ID is the injected dose

$$\frac{\%ID}{mL} = \frac{c_i}{ID} \cdot 100\% \tag{7.11}$$

All animals were handled and studies conducted in accordance with protocols approved by the University of Chicago Institutional Animal Care and Use Committee. Statistical significance of tumor uptake compared to muscle, expressed as p-value, was determined by using a one-tailed Student's t-test [79].

7.2.3 Kinetic Modelling

Using the time-activity curves generated in Section 7.2.2, modelling methods were used to assess the kinetic uptake and washout. The obtained kinetic parameters were then used to infer the mechanisms of radiotracer uptake and retention based on the literature and experimental data.

$VO(acac)_2$ has not been previously assessed with kinetic modelling. Therefore, the modelling methods used were first developed and validated using an existing data set for two nicotinic tracers, 2-FA and Nifene, used in mouse imaging studies. Both radiotracers have previously been modelled using data from similar experiments and therefore, values for

comparison were available in the literature.

The aforementioned modelling methods (Logan Analysis, SRTM, MRTM) were implemented in MATLAB (Mathworks, Natick USA). All models use some form of linear regression for curve fitting, described in Eqn. 7.12. β_k is the kth coefficient, f_k is a scalar-valued function of $X_{i,j}$ that does not need to be linear, $X_{i,j}$ is ith observation of the jth predictor variable, and ϵ_i is the ith noise term, or random error; the 'linearity' refers to the response variable y with the coefficients, β_k.

$$y_i = \beta_0 + \sum_{k=1}^{K} \beta_k f_k(X_{i1}, X_{i,2}...X_{ip}) + \epsilon_i \tag{7.12}$$

The fitted linear function takes the form of Eqn. 7.13, where $\hat{y_i}$ is the estimated response and b_k is the fitted coefficient.

$$\hat{y_i} = b_0 + \sum_{k=1}^{K} b_k f_k(X_{i1}, X_{i,2}...X_{ip}) \tag{7.13}$$

The coefficients are estimated to minimize the residual (the mean-squared difference between the predictor and the response) using the method of least squares.

7.3 Results

7.3.1 In Vitro Cellular Studies

Earlier studies demonstrated that $VO(acac)_2$ is preferentially sequestered in cancer cells [72] [73] [67]. *In vitro* cell studies were carried out to characterize cellular uptake and internalization of the $^{48}VO(acac)_2$ synthesized in this study.

Activity Saturation Study

Fig. 7.1 shows the uptake of $^{48}VO(acac)_2$ for HCA-7 and HCT-116 cells at levels of radioactivity incubation from 0-8 μCi and 0-4 μCi, respectively, normalized to the number of cells plated. The HCA-7 cells exhibited linear uptake of radioactivity over the 0-4 μCi range (corresponding to calculated 0-0.48 nM $^{48}VO(acac)_2$) with apparent plateauing at 8 μCi (0.97 nM, Fig. 7.1A), indicating that saturation of uptake radioactivity occurred over the 4-8 μCi (0.48-0.97 nM) range. Experiments with HCT-116 cells indicated that the rate of cellular uptake of radioactivity increased linearly over the 0-2 μCi (0-0.24 nM) range, continuing at a lower rate over the 2-4 μCi (0.24-0.48 nM) range, as seen in Fig. 7.1B. These experiments demonstrated that $^{48}VO(acac)_2$ was accumulated by both cell lines.

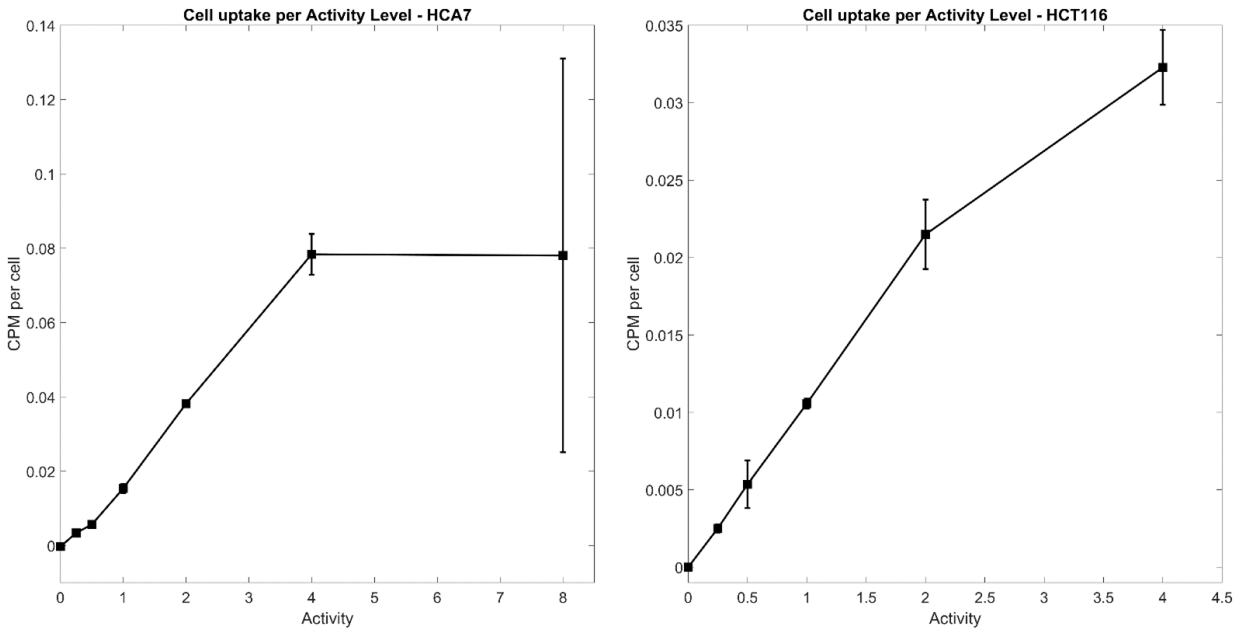

Figure 7.1: Cell uptake curve for HCA-7 (left, A; n=2) and HCT-116 (right, B; n=3) cells incubated in 0-8 μCi. Radiotracer was produced using Method 1.

Uptake and Internalization Studies

The gamma counter used had high levels of error and observed higher background with higher levels of radioactivity used. Due to these limitations, lower radioactivity was used for subsequent $^{48}VO(acac)_2$ uptake and internalization studies. Fig. 7.2 shows the radioactivity taken up by HCA-7 cells in black and the radioactivity taken up by HCT-116 cells in red. The radioactivity remaining after cells were washed after 2 hours and lysed is denoted by a solid line. The radioactivity internalized in the cells is shown by the dashed lines; this data shows the radioactivity remaining after the cells were incubated an additional 2 hours in cell culture media, washed, treated with glycerin, and then lysed. The values herein were normalized to the number of cells per well. This figure shows that the uptake by the HCA-7 cells was much greater than the uptake by the HCT-116 cells: for all incubation activities, the HCA-7 uptake was at least four times higher than the HCT-116 uptake. This trend is also seen in the internalization study: for all incubation activities, the HCA-7 uptake was at least twice the HCT-116 uptake. However, for both cell lines, the amount of radioactivity internalized is much smaller than the amount taken up. For the HCA-7 cells, the amount taken up was at least 10 times higher than the amount internalized at all incubation activities; for the HCT-116 cells, the amount taken up was at least 5 times higher than the amount internalized at all incubation activities.

Fig 7.3 shows the fraction of $^{48}VO(acac)_2$ taken up and internalized. The data shown here is the radioactivity at each point normalized to the incubated radioactivity, not normalized to the number of cells. For all incubation activities and cell lines, the most activity retained was less than 1% the incubation activity. As the incubation activity increased, the fraction taken up or internalized decreased.

Fig. 7.4 shows the difference in uptake of 2 μCi of $^{48}VO(acac)_2$ for cells treated with or without additional, non-radiolabeled $VO(acac)_2$, normalized to the number of cells per dish. For both cell lines, the amount of activity increased with the addition of the $VO(acac)_2$. For

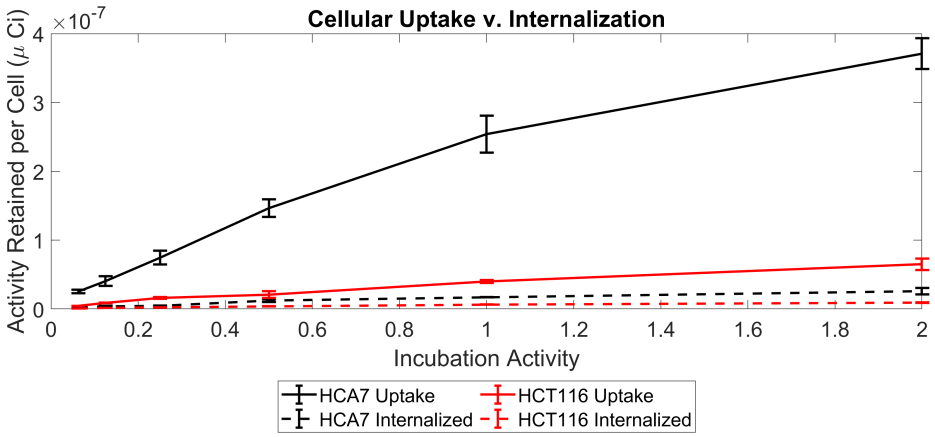

Figure 7.2: Cell uptake curve for HCA-7 and HCT-116 cells incubated in 0-2 μCi, normalized to the number of cells plated; n=3. Radiotracer was produced using Method 2.

the HCT-116 cells, however, the increase was within one standard deviation. The uptake is substantially higher for the HCA-7 cells compared to the HCT-116 cells; the internalization is somewhat higher for the HCA-7 cells compared to the HCT-116 cells.

7.3.2 In Vivo Animal Studies

Tumor Growth Curves

Fig. 7.5 shows the growth of the xenograft tumors over a period of 1 month. The individual tumor sizes varied widely, as demonstrated by the large error bars, particularly in the early weeks post inoculation (shown in the right plot of Fig. 7.5). In general, inoculation with more cells lead to quicker tumor growth: animals inoculated with 5x10^6 HCA-7 cells had tumors of a size suitable for imaging (100-1000 mm^3) after 10 days, while animals inoculated with 1-2x10^6 cells were not ready for imaging for several weeks. In the 2022 imaging study, animals inoculated with HCT-116 cells could be imaged much more quickly than HCA-7 animals - they could be imaged after 2 weeks if inoculated with 2x10^6 HCT-116 cells, while the HCA-7 mice still had small tumors at the end of the growth period (30 days).

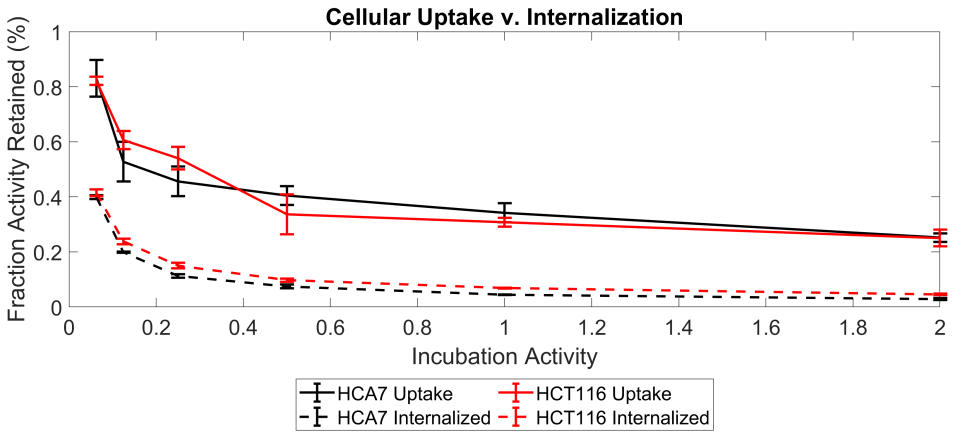

Figure 7.3: Fractional uptake curve for HCA-7 and HCT-116 cells incubated in 0-2 μCi; n=3. Radiotracer was produced using Method 2.

PET Studies

In the 12 animals imaged, tumor sizes ranged from 84-2270 mm^3. An example of the static image of a coronal section of a mouse during imaging is shown in Fig. 7.6. For the first 8 mice imaged, the dose was administered through tail-vein injection and imaging began immediately after; for the last 4 mice imaged, the dose was administered through a catheter and imaging began immediately. Average time-activity curves are shown in Fig. 7.7 for mice inoculated with HCA-7 cells (average of 10 mice imaged) and in Fig. 7.8 for mice inoculated with HCT-116 cells (average of 2 mice imaged). Fig. 7.9 shows the time-activity curve of just the tumor and muscle tissues for both cell lines.

HCA-7: These figures show that the uptake is primarily in the liver and kidney tissues: for the HCA-7 inoculated mice, the uptake in the kidney and liver tissues was 3-5 times higher compared to the brain, muscle, and tumor tissues. The muscle and tumor tissues had comparable uptake and were within one standard deviation of each other in value for all time points. In comparing the muscle and tumor tissues, the level of uptake is similar for most of the studies: for 3 out of 8 animals imaged, the tumor uptake is greater at the end of the study; for 4 out of 8 mice imaged, the muscle concentration is greater. For only one

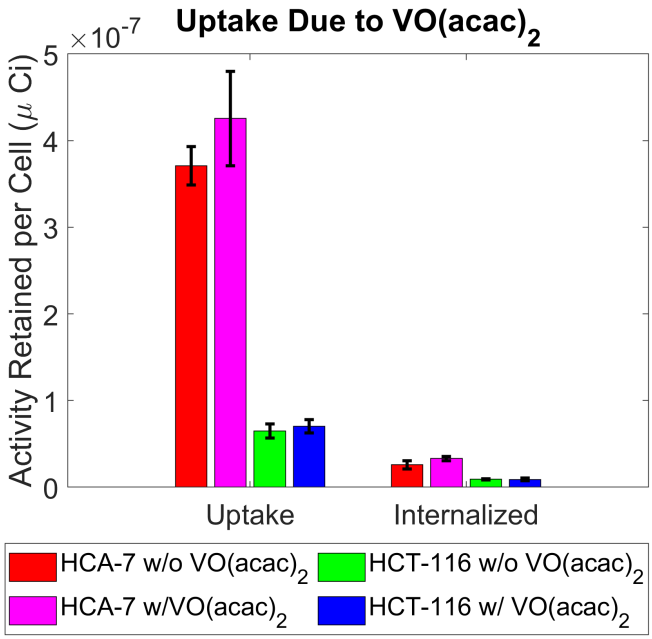

Figure 7.4: Cell uptake values for HCA-7 (n=2) and HCT-116 cells (n=3) incubated in 2 μCi with or without added $VO(acac)_2$, normalized to the number of cells plated. Radiotracer produced using Method 2

mouse imaged, the uptake in the brain was greater than the muscle or tumor uptake, though still substantially less than the kidney or liver. Uptake values could not be obtained for two mice due to lack of CT for anatomical correlation. At the end of the four-hour imaging, the %ID/mL was 1.51±0.21% for the brain, 8.10±1.67% for the kidney, 8.64±1.48% for the liver, 1.65±0.18% for the muscle, and 1.61±0.16% for the tumor. Of these tissues, the uptake varied the most in the kidney and liver tissues, where the standard deviation was 21% and 17% of the mean, respectively.

HCT-116-7: Mice inoculated with HCT-116 cells showed the greatest uptake in the kidney and liver tissues. The uptake varied widely between animals, evidenced by the large standard deviation and error bars shown. The uptake in the kidney and liver tissues was 10 times higher than the muscle, tumor, or brain tissues. For all time points, the uptake in the muscle and tumor tissues was within one standard deviation of each other. At the end of the four

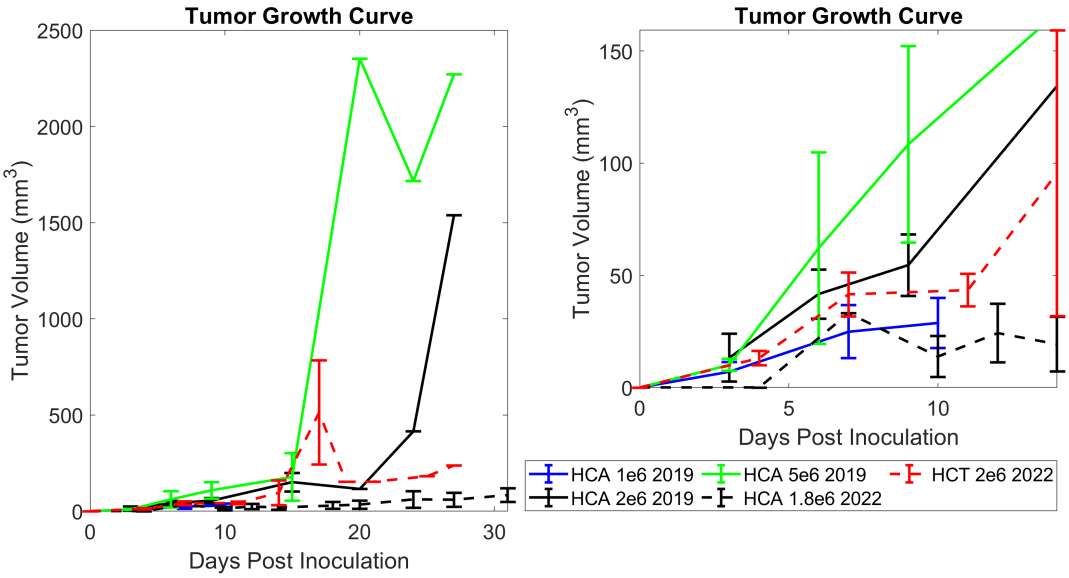

Figure 7.5: Growth curve of xenograft HCA-7 and HCT-116 tumors. The inset is shown expanded to the right. For each curve, n=5

hour imaging, the %ID/mL was 0.84±0.60% for the brain, 11.58±8.19% for the kidney, 6.23±4.40% for the liver, 0.38±0.27% for the muscle, and 0.63±0.44% for the tumor.

Overall, the average uptake in the HCT-116 tumors (a maximum value of 0.95% at 37 minutes) was lower than the uptake in the HCA-7 tumors (a maximum value of 1.72% at 65 minutes). Fig. 7.10 shows the uptake in HCA-7 tumors per tumor size. The larger tumors tend to be towards the top of the plot, indicating higher uptake. However, there is not a clear separation in uptake per tumor size and the smallest tumors (<100 mm^3) are in the middle of the plot for most time points.

Biodistribution Studies

Average biodistribution results for muscle and tumor are shown in Fig. 7.11 and Fig. 7.12. The assayed radioactivity of the tissue was normalized to the weight of the tissue once excised and the initial injected dose. While the time-activity curves showed comparable uptake in the kidney and liver for both cell lines, the biodistribution studies show higher uptake in the

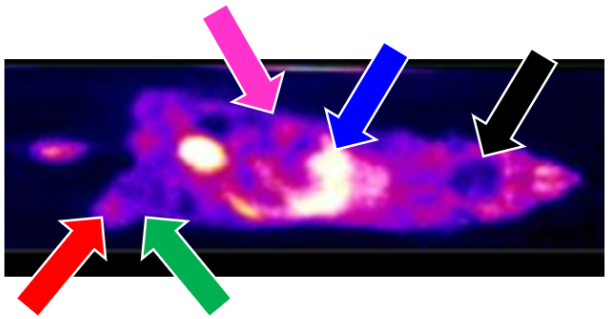

Figure 7.6: An example of the static image of mouse with HCA-7 xenograft tumor. Colored arrows denote the ROI selected. Colors correspond with the ROIs shown in Fig. 7.7; black is the brain, pink is the kidney, blue is the liver, green is the muscle, and red is the tumor.

liver tissues. Additionally, the biodistribution results show high radiotracer uptake in the intestine, lungs, and spleen. Similar to the PET results, the excised tumor, muscle, and brain tissues all show low uptake compared to other tissues. The uptake in tissues excised from mice inoculated with the two different cell lines is within one standard deviation for most tissues. The exceptions are the spleen and heart. For both tissues, the mice inoculated with HCT-116 cells had much higher uptake in these tissues.

For the HCA-7 tissues, the tumor showed a 50% increase in radioactivity compared to muscle tissues with a p-value less than 0.001 (shown in Fig. 7.12), indicating a statistically significant uptake increase in tumor and potential effective detection. Fig. 7.9 shows comparable uptake in the tumor and muscle at the end of the four hour imaging, the closest time point of the biodistribution study. The difference could reflect different volumes selected: the tumor ROI is selected based on the PET/CT image, while the excised tissue is selected based on visual confirmation of the tumor location and is therefore a more reliable metric of tumor volume. The analysis was not repeated with the HCT-116 tissues due to the low number of samples (n=2). Fig. 7.12 shows that for mice inoculated with HCT-116 cells, the tumor had lower uptake than the muscle, though these values are within one standard deviation of each other.

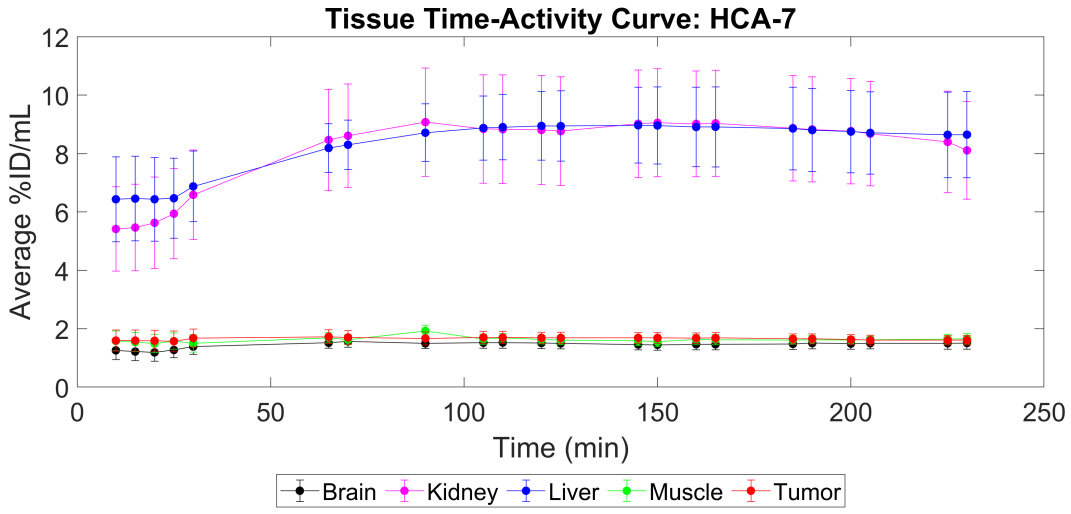

Figure 7.7: Time-activity curve for tissues of interest over 4 hour imaging of mice inoculated with HCA-7 cells (n=10).

7.3.3 Kinetic Modelling

The time-activity curves from Section 7.3.2 were used for kinetic modelling to determine the distribution volume ratio (DVR), a unit-less metric. Only the data from mice inoculated with HCA-7 (n=10) were used; the data from the HCT-116 mice were not used for kinetic modelling due to the small number of animals studied (n=2). Values obtained for DVR are shown in Table 7.1 for kidney, liver, muscle, and tumor tissues. The brain was used as a reference tissue and therefore, no value of DVR is provided for that tissue. All three methods are averaged together and presented in the 'Average' row.

The largest DVR values were observed for the liver and kidney tissues. The two tissues were similar in value for the Logan Analysis and SRTM methods. However, using MRTM, the liver DVR was three times higher than the kidney DVR (14.74 and 4.87, respectively). The tumor tissue DVR was larger than the muscle for two modelling methods (SRTM and MRTM) but was smaller than muscle when calculated using Logan Analysis. For all three methods, the tumor and muscle DVR are within one standard deviation of each other. Comparing methods,

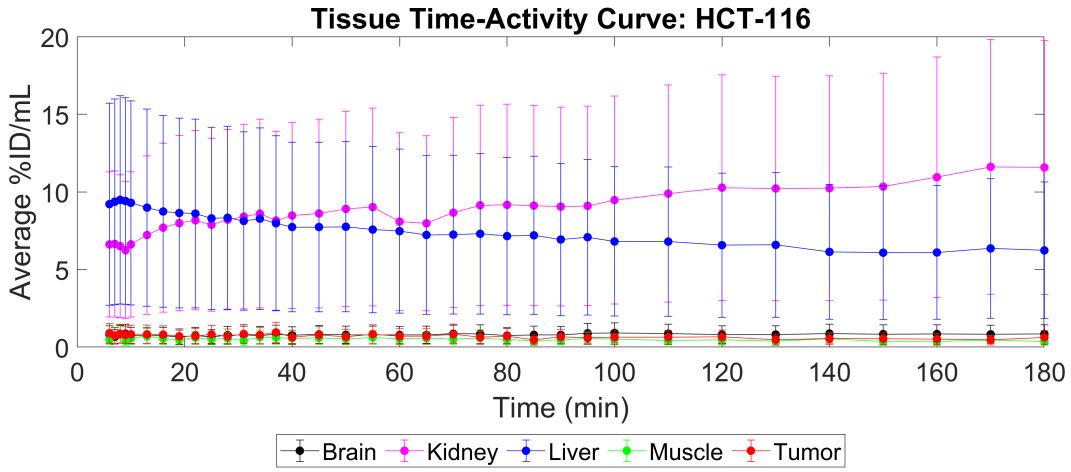

Figure 7.8: Time-activity curve for tissues of interest over 4 hours of imaging mice inoculated with HCT-116 cells (n=2).

MRTM tended to have the highest variation: it had the highest cumulative coefficient of variation (the ratio of standard deviation to the mean value, calculated as 2.1 for MRTM) across all tissues, followed by SRTM (coefficient of variation of 1.6), then Logan Analysis (coefficient of variation of 1.0). This indicates that Logan Analysis provided the values with the least variation across all datasets. For MRTM and SRTM, the liver had the highest variation in the DVR values; the standard deviation accounted for 115% and 61% of the mean, respectively. The variation tended to be smallest for the muscle and tumor values across all modelling methods.

	Kidney	Liver	Muscle	Tumor
Logan	5.20±1.87	5.22±0.86	1.30±0.38	1.29±0.28
SRTM	6.64±3.67	7.60±4.61	1.12±0.28	1.14±0.29
MRTM	4.87±1.84	14.74±16.95	1.18±0.27	1.33±0.46
Average	5.57±0.94	9.19±4.95	1.20±0.09	1.25±0.10

Table 7.1: DVR values for kidney, liver, muscle, and tumor tissues obtain using Logan Analysis, SRTM, or MRTM.

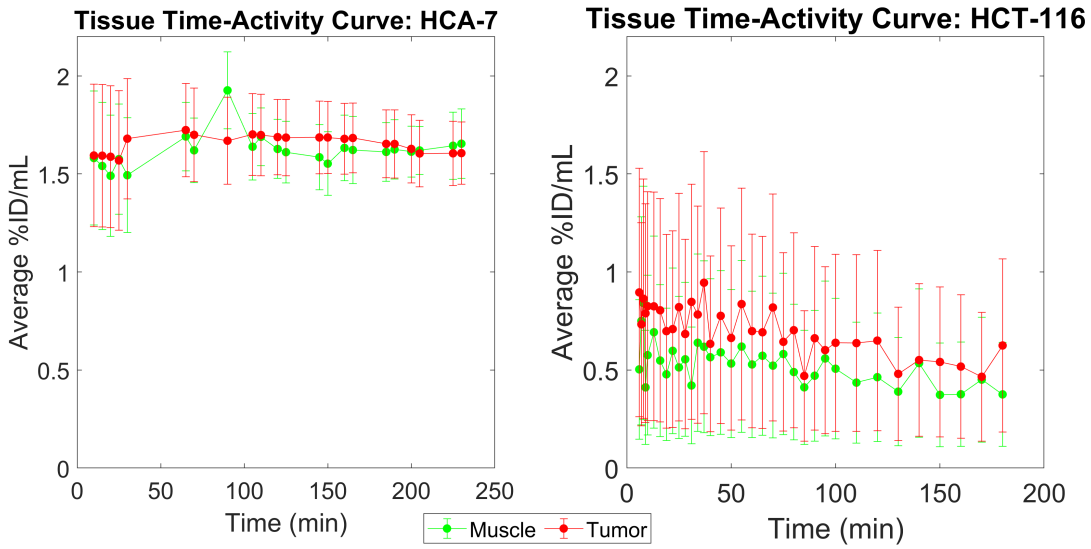

Figure 7.9: Time-activity curve for muscle and tumor tissues over 4 hours of imaging mice inoculated with HCA-7 cells (left, n=10) or HCT-116 cells (right, n=2).

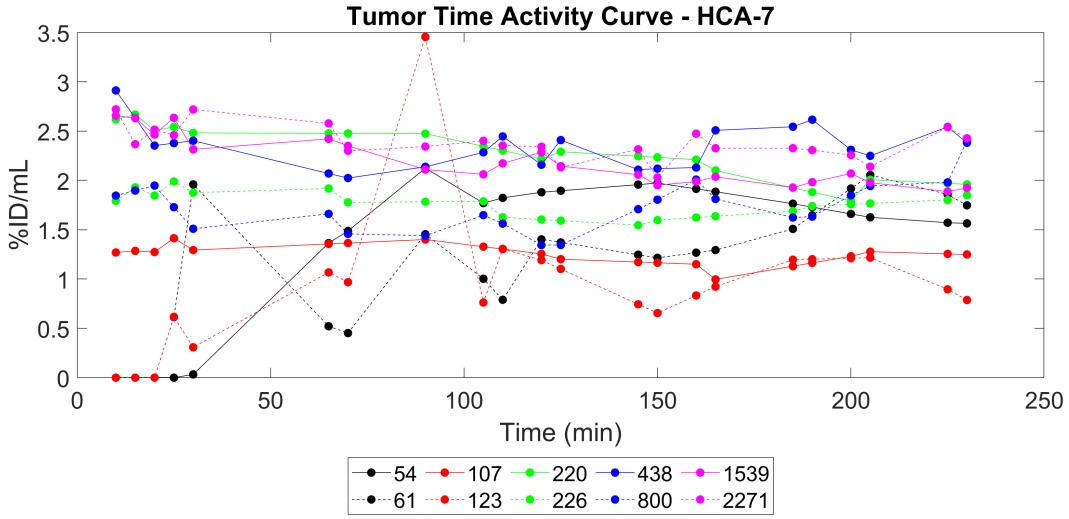

Figure 7.10: Time-activity curve for tumor tissues over 4 hours of imaging mice inoculated with HCA-7 cells, sorted by tumor size (n=10).

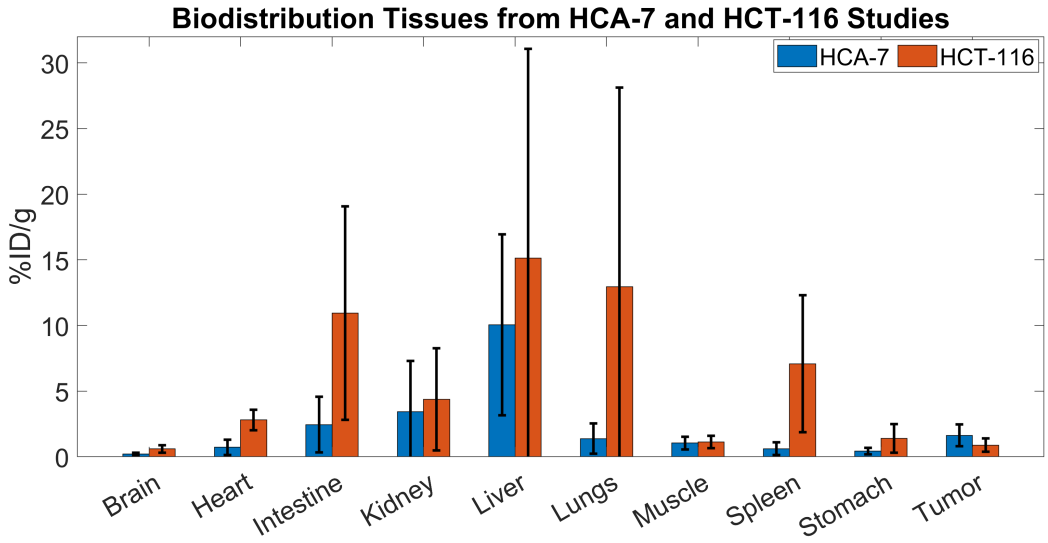

Figure 7.11: Biodistribution of excised tissues from mice inoculated with HCA-7 (n=4) or HCT-116 (n=4) cells. Muscle was taken from the same leg as the tumor.

7.4 Discussion

In vitro studies indicated the compound was taken up by the corresponding cancer cell lines. For both HCA-7 and HCT-116 cells, the amount of radiotracer taken up was much higher than the amount internalized, indicating that the $^{48}VO(acac)_2$ is not being internalized as much as previously reported. Further work is needed to understand this difference, including potentially exploring other cell lines with different receptors that might be more suitable to uptake of $VO(acac)_2$.

In comparison across studies, the HCA-7 tumors grew more quickly in the 2019 study; while the 'HCA-7 2x10^6 2019' and 'HCA-7 1.8x10^6 2022' groups were inoculated with similar numbers of cells, the tumors in the 2019 study grew more quickly. This trend could also be seen in the cell culture - qualitatively, the HCA-7 cells took much longer to culture in the later study. All cells were initially frozen for later use at the same time. However, at some point the freezer experienced technical difficulties, which may have affected the integrity of the cells and limited their growth.

While *in vivo* studies showed some uptake of $^{48}VO(acac)_2$, the uptake in the muscle

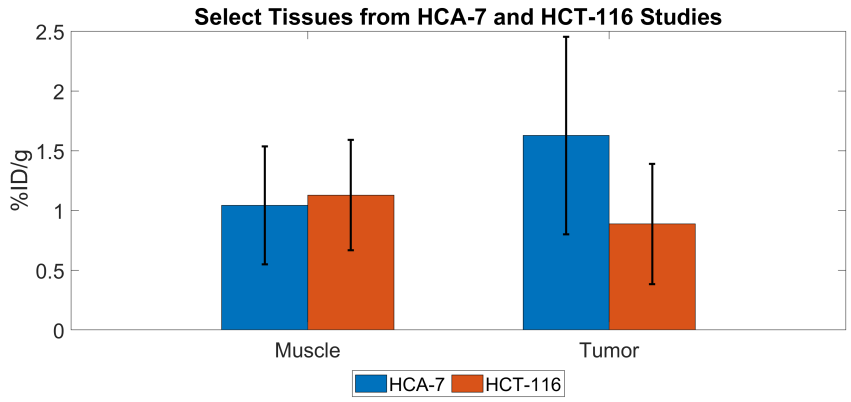

Figure 7.12: Biodistribution of excised muscle and tumor tissues from mice inoculated with HCA-7 (n=10) or HCT-116 (n=4) cells. Muscle was taken from the same leg as the tumor.

was comparable to tumor, indicating a tumor-muscle ratio around 1; this is a metric often used to determine whether a radiotracer is likely to be successful in imaging of malignant tissues. The poor tumor-muscle contrast demonstrated also limits the utility of differentiating these tissues, a primary motivator for this radiotracer. The non-enhanced uptake could have several contributing factors. For example, the *in vivo* study in the literature for comparison, Mustafi et al. 2009 [72], did not use xenograft tumors and also used a prostate cancer cell line. Future work should explore studies with other cell lines, including other types of CRC as xenograft tumors and possibly endogenous tumors.

In this study, PET imaging was conducted over four hours. However, ^{48}V has a 16-day half-life, indicating it could be used for longitudinal studies or disease monitoring. Future studies should be conducted over longer durations to assess radiotracer retention over time. A longer time scale for imaging studies could also help confirm that the radiotracer is reversibly bound to the tissue.

In early studies, the tumor was thought to be necrotic, which would inhibit uptake at the tumor core where the cells have died. Layer analysis in Vivoquant showed that uptake was greater for the external layers of the tumor, but this could not be used to confirm necrosis; the tissue was not excised after this imaging study. After necrosis was thought to be a problem,

tumor size was monitored more closely and a wider variety of tumor sizes, including smaller tumors, were used in order to cover different stages of tumor progression. As discussed in Section 7.3.2, the larger tumors did tend to show greater uptake of the $^{48}VO(acac)_2$, but there was not a clear correlation between uptake and tumor size.

A factor affecting the ability of the radiotracer to reach various tissues was the composition of the radiotracer injected. Tracer solubility was difficult for early syntheses, resulting in DMSO being used to dissolve the compound. For these studies, dissolution in saline was attempted first before introducing increasing quantities of DMSO. Since cold vanadyl is soluble in water, this indicates that some contaminant is precipitating in the solution. After elemental analyses of the radiotracer, it was shown that calcium, which can form a precipitate, was present in the sample. In studies using the compound from Method 2, there was no indication a precipitate had formed. While elemental analyses were not conducted for the compound resulting from Method 2, the lack of precipitate indicated that Method 2 more effectively filtered these insoluble contaminants.

The low DVR values for the tumor reflect the low uptake in this region compared to other tissues. The feasibility of kinetic modelling is significantly impacted by tissue-specific radiotracer uptake. As shown in Section 7.3.2, the data do not form a clear curve. Other radiotracers used for modelling (2FA, nifene, etc.) have a distinct period of uptake and release visible in the time-activity curve. The lack of adequate uptake seen in the $^{48}VO(acac)_2$ studies makes the modelling data difficult to interpret. Future work should improve radiotracer uptake through alteration of the synthesis or utility of other cells lines in order to improve the quality of data and subsequently, the quality of the kinetic modelling parameters.

7.5 Conclusion

While $^{48}VO(acac)_2$ was shown to be taken up by HCA-7 and HCT-116 cells *in vitro*, subsequent animal imaging of mice inoculated with these cell lines showed relatively low

uptake in the xenograft tumors, making kinetic modelling difficult and the parameters obtained difficult to interpret. Future work should explore alternative cell lines and possible endogenous tumors in order to increase the uptake in the tumor and improve the tumor-muscle ratio overall.

CHAPTER 8

CONCLUSIONS AND FUTURE DIRECTIONS

The purpose of this work was to develop a novel radiotracer for imaging and potential staging of colorectal cancers, with possible applications to other types of cancer in the future. Specifically, the objectives were to (1) Produce ^{48}V via a Compact Medical Cyclotron; (2) Establish a New Procedure for the Synthesis of $^{48}VO(acac)_2$; and (3) Conduct *In-Vitro* and *In-Vivo* Studies to Model Kinetics of $^{48}VO(acac)_2$. The below sections summarize how these aims were fulfilled, the conclusions that can be drawn from them, and outline future work related to this research.

8.1 Summary of Work

Chapter 3 explored the feasibility of producing ^{48}V using thin natural titanium foils placed in the beamstop of the UC cyclotron. Using this system, targets were irradiated for 0.5-72 hours, producing radioactive yields of 0.064-34.8 mCi. Two geometries were used in this system: a cup and a sphere.

Due to the inexact nature of the beamstop target system, Chapter 4 examined the effect of target movement or irregularities in target formation on the radiation yield using Monte Carlo program TOPAS. Cup- and sphere- shaped ^{nat}Ti targets were simulated. Movement was simulated by placing the target at three positions along the z-axis: at a position determined to be the origin where the beam parameters were determined; 2 cm closer to the beam; and 2 cm farther from the beam. The cup targets were also simulated as having no tilt, a 10° tilt, or a 15° tilt. Irregularities in target formation were simulated by altering the base of the cup targets (15 or 17 mm) and the diameter and corresponding density of the sphere targets (8, 10, 12, or 14 mm).

$^{48}VO(acac)_2$ had not previously been synthesized and no methods exist in the literature

to characterize it that are suitable for detecting the small, femtogram-level quantity of material present in a radiotracer solution. Chapter 5 assessed HPLC methods to characterize $VO(acac)_2$. Fifteen methods were assessed with variable conditions, including EtOH and MeCN mobile phases, various gradients, different flow rates, the presence of 0.1% TFA, and two different wavelengths.

Equipped with a means to characterize the compound, Chapter 6 details the development of a procedure to synthesize $^{48}VO(acac)_2$. Two different methods were attempted and the modifications made from each iteration of radiotracer synthesis detailed. The target was dissolved with concentrated or 6 M H_2SO_4 and HF; ^{48}V was isolated from other transition metals and elements using a Chelex-100 or AG 50W-X8 separation column; vanadate was reduced to vanadyl and chelated to acetylacetone; and the compound was characterized via HPLC, TLC, and gamma-ray spectroscopy.

Using the radiotracer synthesized, *in vitro* and *in vivo* studies were conducted. Colon and colorectal cancer cell lines HCA-7 and HCT-116 were used. Cell studies were conducted with radioactivity levels from 0-8 μCi/0.2 mL and consisted of uptake and internalization assays. For animal imaging, HSD athymic nude mice were inoculated with 1-5x10^6 HCA-7 or HCT-116 cells in the right hind limb and imaged via PET/CT when tumors had a volume of 100-1000 mm^3. The injected dose was between 30-100 μCi and imaging lasted 4 hours, followed by biodistribution studies. The time-activity curves obtained during this imaging were used for kinetic modelling to obtain a value for distribution volume using Logan Analysis, SRTM, or MRTM modelling methods.

8.2 Conclusions

Of the two geometries used, the sphere produced higher yields. However, use of this target geometry increased the target dissolution time significantly, resulting in later studies returning to the cup geometry. Target irradiations were most efficient when maximizing the time of

irradiation over as few days as possible, while allowing a period post irradiation for short-lived isotopes to decay. With a timeline of 4-5 days of irradiation and 2-3 days of decay, this process creates a target whose radioactivity is >85% ^{48}V based on potentially co-produced radionuclides and their rates of decay. These studies illustrated the feasibility of using a beamstop in a regular compact medical cyclotron without a solid target system to produce ^{48}V.

TOPAS simulations estimated a larger yield for the sphere targets than was experimentally assayed. The simulated target yield closest to the assayed yield was for the 14 mm diameter target, which provided a 12% overestimation of the 31.6 mCi assayed yield. Three of the four cup-shaped targets assayed experimentally had yields that agreed with the TOPAS estimated value to within 5%. Overall, simulations of a 17 mm base cup with no translation or tilt agreed best with the experimental targets 12, 13, and 15. All simulations overestimated the yield of target 14 by at least 70%, likely due to irregularities in the formation of this target. These results demonstrated the usefulness of computer simulation studies, such as those using TOPAS herein, to investigate and evaluate various parameters and factors involved in cyclotron-based production of radioisotopes. This work provides insight to improve setup parameters for target irradiation

The best method to observe $VO(acac)_2$ was determined to be a mobile phase of 40-60% MeCN-H_2O in 0.1% TFA with a flow rate of 1.2 mL/min. and 320 nm wavelength. This was the only method that could differentiate between $VO(acac)_2$ and acetylacetone, an important quality due to the presence of acetylacetone in the synthesized radiotracer solution. The amplitude of the HPLC peak observed decreased over the course of week, indicating that the compound may not be stable in EtOH.

The separation of ^{48}V from co-produced radionuclides was confirmed via gamma-ray spectroscopy, which showed no peaks other than those associated with ^{48}V within the limits of the NaI detector used. HPLC analysis confirmed that $^{48}VO(acac)_2$ was synthesized using

both Method 1 and Method 2 by observing a radiopeak at the same retention time as the UV peak of $VO(acac)_2$. However, TLC results were inconclusive. Overall synthesis time was at least 13 days for Method 1 and 4 days for Method 2; the yield was 16.5±3.9% for Method 1 and 12.4% for Method 2.

Cell studies demonstrated that $^{48}VO(acac)_2$ was taken up by both HCA-7 and HCT-116 cell lines *in vitro*. However, initial animal imaging studies demonstrated low tumor uptake, comparable to the muscle tissue and therefore yielding poor tumor to muscle contrast. At the end of the four-hour imaging, for mice inoculated with HCA-7, the %ID/mL was 1.51±0.21% for the brain, 8.10±1.67% for the kidney, 8.64±1.48% for the liver, 1.65±0.18% for the muscle, and 1.61±0.16% for the tumor. For mice inoculated with HCT-116, the %ID/mL was 0.84±0.60% for the brain, 11.58±8.19% for the kidney, 6.23±4.40% for the liver, 0.38±0.27% for the muscle, and 0.63±0.44% for the tumor. Biodistribution studies showed 50% greater radioactivity in the tumor compared to the muscle at the end of imaging for the HCA-7 mice. Kinetic modelling using the muscle as a reference tissue provided a distribution volume ratio of 5.57±0.94 in the kidney, 9.19±4.95 in the liver, 1.20±0.09 in the muscle, and 1.25±0.10 in the tumor. Due to the low uptake in the tumor tissue, it is difficult to extract meaning from these values. Additional, future *in vitro* and *in vivo* studies will be needed to draw more definitive conclusions.

8.3 Future Directions

Although the beamstop target system is not an ideal setup, it does provide a mechanism to generate ^{48}V, allowing feasibility studies to be conducted with the radioisotope. Long-term, regular production of ^{48}V would require a solid target system that can more efficiently cool the target, allowing use of a thicker target that can make more effective use of the beam and resulting in either shorter irradiations to generate comparable yields or comparable irradiations to generate higher yields. Yield could also be increased by using enriched ^{48}Ti

instead of ^{nat}Ti, which would also decrease co-produced radionuclides. Future work should explore these methods to increase radioactivity yields.

This work demonstrated that TOPAS simulations can be a useful tool in predicting target yields and assessing irradiation conditions. Ultimately, the target formation and irradiation conditions provide a range of potential irregularities that are difficult to fully capture and replicate in simulation, complicated by the lack of appropriate physics list at this energy regime. Future studies in TOPAS should find a more suitable physics list for these conditions and explore further irregularities that could be introduced by the beamstop target system.

Establishing an appropriate method to characterize $VO(acac)_2$ via HPLC is a necessary step to characterizing $^{48}VO(acac)_2$. Future work should explore the stability of $VO(acac)_2$ over time and assess the composition of the peaks in terms of the oxidation state and the presence of any vanadium species to determine how the compound changes.

While the synthesis of $^{48}VO(acac)_2$ was confirmed via HPLC and gamma-ray spectroscopy, future work should explore why the TLC results were inconclusive. Additionally, the yields were quite low for both methods of synthesis. The lowest step-wise yield was during the C-18 cartridge filtration step, which yielded 53% of radioactivity for Method 1 and only 20% of radioactivity for Method 2. Future work should attempt to increase these yields, perhaps by improving the previous steps in reduction of oxidation state and chelation to acetylacetone and potentially exploring alternative filtration methods.

Despite uptake in *in vitro* studies, *in vivo* uptake was relatively low across all animals imaged. Future work should explore other cell lines to find a cancer model more suitable to take up this radiotracer. This could include imaging mice with endogenous instead of xenographic tumors. Additionally, work should be done with $^{48}VO(acac)_2$ to understand why these cell lines do not take up the radiotracer - perhaps they are lacking some critical pathway or receptor. These parameters should improve imaging data, which would provide more meaning to kinetic analysis.

This work demonstrates the feasibility of producing ^{48}V in a beamstop target system and using it to synthesize the novel radiotracer $^{48}VO(acac)_2$. Methods were developed to characterize the radiotracer, which subsequently indicated that the ^{48}V had been radioisotopically separated and correctly chelated. These developed procedures serve as a starting point for future work to more efficiently produce this radiotracer. Additionally, simulations were developed to explain variations in target yield. The simulations can serve as a tool to help develop targetry and explore how various conditions can affect the amount of radioactivity generated in future studies. Further *in vivo* work is needed to identify a cell line or cancer time more suitable to take up this radiotracer and provide data suitable for kinetic analysis.

APPENDIX A

EXAMPLE TOPAS FILES

A.1 Cyclotron File

```
i:Ts/ShowHistoryCountAtInterval = 0
includefile = cs-v48_par.txt #—Textfile for target
b:Ts/PauseBeforeQuit = "False"
s:Ph/Default/Type = "QGSP_BERT_HP"

#—Define World
s:Ge/World/Material = "Vacuum"
d:Ge/World/HLX = 100 cm
d:Ge/World/HLY = 100 cm
d:Ge/World/HLZ = 200 cm

#—Define Beam
s:So/protons/Type = "Emittance"
s:So/protons/Component = "BeamPosition"
s:So/protons/BeamParticle = "proton"
d:So/protons/BeamEnergy = 18.00 MeV
uc:So/protons/BeamEnergySpread = 0.1
ic:So/protons/NumberOfHistoriesInRun = 1000
d:Ge/BeamPositions/TransZ = 140 cm

#—Define Emittance Source Properties
sc:So/protons/Distribution = "BiGaussian"
dc:So/protons/SigmaX = 0.01 cm
uc:So/protons/SigmaXprime = 0.001
uc:So/protons/CorrelationX = 0
dc:So/protons/SigmaY = So/protons/SigmaX cm
uc:So/protons/SigmaYPrime = So/protons/SigmaXprime
uc:So/protons/CorrelationY = So/protons/CorrelationX

#—Define Time and Threads
d:Tf/TimelineStart = 0. s
d:Tf/TimelineEnd = 1. s
i:Tf/NumberOfSequentialTimes = 1000
i:Ts/NumberOfThreads = 4
```

A.2 Target File

sv:Ma/natTi/Components = 1 “Titanium”
uv:Ma/natTi/Fractions = 1 1.0
d:Ma/natTi/Density = 4.54 g/cm3

s:Ge/Nest/Type = “TsBox”
s:Ge/Nest/Parent = “World”
s:Ge/Nest/Material = “Vacuum”
d:Ge/Nest/HLX = 5.0 cm
d:Ge/Nest/HLY = 5.0 cm
d:Ge/Nest/HLZ = 5.0 cm
d:Ge/Nest/TransZ = 0.0 cm
d:Ge/Nest/RotX = 0 deg

#–Define target edges (sides) and base (end) s:Ge/Edge/Type = “TsCylinder”
s:Ge/Edge/Parent = “Nest”
s:Ge/Edge/Material = “natTi”
d:Ge/Edge/TransX = 0 cm
d:Ge/Edge/TransY = 0 cm
d:Ge/Edge/TransZ = 3.774 mm
d:Ge/Edge/RotX = 0 deg
d:Ge/Edge/RotY = 0 deg
d:Ge/Edge/RotZ = 0 deg
d:Ge/Edge/RMin = 4.988 mm
d:Ge/Edge/RMax = 5 mm
d:Ge/Edge/HL = 3.75 mm
d:Ge/Edge/SPhi = 1 rad

s:Ge/End/Type = “TsCylinder”
s:Ge/End/Parent = “Nest”
s:Ge/End/Material = “natTi”
d:Ge/End/TransX = 0 cm
d:Ge/End/TransY = 0 cm
d:Ge/End/TransZ = 0 mm
d:Ge/End/RotX = 0 deg
d:Ge/End/RotY = 0 deg
d:Ge/End/RotZ = 0 deg
d:Ge/End/RMin = 0.0 mm
d:Ge/End/RMax = 5 mm
d:Ge/End/HL = 0.0124 mm
d:Ge/End/SPhi = 1 rad

REFERENCES

[1] Kehinde Adekola, Steven T Rosen, and Mala Shanmugam. Glucose transporters in cancer metabolism. *Current opinion in oncology*, 24(6):650, 2012.

[2] International Atomic Energy Agency. Cyclotron produced radionuclides: Principles and practice., 2008. URL https://www-pub.iaea.org/MTCD/publications/PDF/trs465_web.pdf.

[3] International Atomic Energy Agency. Alternative radionuclide production with a cyclotron, 2021. URL https://www-pub.iaea.org/MTCD/publications/PDF/P1937_web.pdf.

[4] Sigma Aldrich. Certificate of analysis, 2014. URL https://www.sigmaaldrich.com/certificates/COFA/55/550787/550787-BULK_____MKBS2189V_.pdf.

[5] Carolyn J Anderson, Xiaoxi Ling, David J Schlyer, and Cathy S Cutler. A short history of nuclear medicine. In *Radiopharmaceutical Chemistry*, pages 11–26. Springer, 2019.

[6] Eric Berg, Herman Gill, Jan Marik, Annie Ogasawara, Simon Williams, Guus van Dongen, Daniëlle Vugts, Simon R Cherry, and Alice F Tarantal. Total-body pet and highly stable chelators together enable meaningful 89zr-antibody pet studies up to 30 days after injection. *Journal of Nuclear Medicine*, 61(3):453–460, 2020.

[7] MJ Berger, JS Coursey, MA Zucker, and J Chang. Stopping-power and range tables for electrons, protons, and helium ions, nist standard reference database 124. *National Institute of Standards and Technology*, 2017.

[8] Bio-Rad. Biologic quadtec uv/vis detector, Accessed 9 March 2022. URL https://www.bio-rad.com/webroot/web/pdf/lsr/literature/Bulletin_2845.pdf.

[9] BioRad. Ag 50w and ag mp-50 cation exchange resins instruction manual, Accessed 29 April 2022. URL https://www.bio-rad.com/webroot/web/pdf/lsr/literature/LIT203.pdf.

[10] BioRad. Chelex 100 and chelex 20 chelating ion exchange resin instruction manual, Accessed 29 April 2022. URL https://www.bio-rad.com/sites/default/files/webroot/web/pdf/lsr/literature/LIT200.pdf.

[11] Guenther Boden, Xinhua Chen, Jose Ruiz, George DV van Rossum, and Salvatore Turco. Effects of vanadyl sulfate on carbohydrate and lipid metabolism in patients with non—insulin-dependent diabetes mellitus. *Metabolism*, 45(9):1130–1135, 1996.

[12] ML Bonardi, E Rizzio, M Gallorini, F Groppi, and HS Mainardi. Improved radiochemical separation of no-carrier-added vanadium-48 from proton irradiated titanium target. *Journal of radioanalytical and nuclear chemistry*, 263(1):23–28, 2005.

[13] Michael G Brattain, W David Fine, F Mahnaz Khaled, Jerry Thompson, and Diane E Brattain. Heterogeneity of malignant cells from a human colonic carcinoma. *Cancer research*, 41(5):1751–1756, 1981.

[14] ME Brown and BV Stewart. The thermal decomposition of ammonium metavanadate, i. *Journal of thermal analysis*, 2(3):287–299, 1970.

[15] BE Bryant and W Conard Fernelius. Direct preparation from vanadium (v) oxide. *Inorganic Syntheses*, 5:115–116, 1957.

[16] Richard E Carson. Tracer kinetic modeling in pet. In *Positron emission tomography*, pages 127–159. Springer, 2005.

[17] Esther Castellano and Julian Downward. Ras interaction with pi3k: more than just another effector pathway. *Genes & cancer*, 2(3):261–274, 2011.

[18] National Nuclear Data Center. Nudat 2.8, 2022. URL `https://www.nndc.bnl.gov/nudat3/chartNuc.jsp`.

[19] Jaroslav Červenák and Ondřej Lebeda. New cross-section data for proton-induced reactions on natti and natcu with special regard to the beam monitoring. *Nuclear Instruments and Methods in Physics Research Section B: Beam Interactions with Materials and Atoms*, 480:78–97, 2020.

[20] Simon R Cherry, James A Sorenson, and Michael E Phelps. *Physics in nuclear medicine e-Book*. Elsevier Health Sciences, 2012.

[21] DA Chesler. 3-dimensional activity distribution from multiple positron scintigraphs. In *Journal of Nuclear Medicine*, volume 12, page 347. Soc. Nuclear Medicine Inc., 1971.

[22] O Chiewitz and G v Hevesy. Radioactive indicators in the study of phosphorus metabolism in rats. *Nature*, 136(3445):754–755, 1935.

[23] Jim Clark. The beer-lambert law, 2020. URL `https://chem.libretexts.org/Bookshelves/Physical_and_Theoretical_Chemistry_Textbook_Maps/Supplemental_Modules_(Physical_and_Theoretical_Chemistry)/Spectroscopy/Electronic_Spectroscopy/Electronic_Spectroscopy_Basics/The_Beer-Lambert_Law`.

[24] Neil Cohen, Meyer Halberstam, Pavel Shlimovich, Chee Jen Chang, Harry Shamoon, Luciano Rossetti, et al. Oral vanadyl sulfate improves hepatic and peripheral insulin sensitivity in patients with non-insulin-dependent diabetes mellitus. *The Journal of clinical investigation*, 95(6):2501–2509, 1995.

[25] Maurizio Conti and Lars Eriksson. Physics of pure and non-pure positron emitters for pet: a review and a discussion. *EJNMMI physics*, 3(1):1–17, 2016.

[26] John Christopher Cornell, editor. *The IBA PET-Dedicated Cyclotrons: Main Features and Improvements.*, Cape Town, South Africa, 1996. World Scientific.

[27] K Cusi, S Cukier, RA DeFronzo, M Torres, FM Puchulu, and JC Pereira Redondo. Vanadyl sulfate improves hepatic and muscle insulin sensitivity in type 2 diabetes. *The Journal of Clinical Endocrinology & Metabolism*, 86(3):1410–1417, 2001.

[28] EC Dijkers, TH Oude Munnink, JG Kosterink, AH Brouwers, PL Jager, JR De Jong, GA Van Dongen, CP Schröder, MN Lub-de Hooge, and EG De Vries. Biodistribution of 89zr-trastuzumab and pet imaging of her2-positive lesions in patients with metastatic breast cancer. *Clinical Pharmacology & Therapeutics*, 87(5):586–592, 2010.

[29] John W Dolan. How does it work? part iv: ultraviolet detectors: detectors based on ultraviolet absorbance are the most common detectors in use for liquid chromatography. *LC-GC North America*, 34(8):534–539, 2016.

[30] J Edel and E Sabbioni. Vanadium transport across placenta and milk of rats to the fetus and newborn. *Biological trace element research*, 22(3):265–275, 1989.

[31] Gerard Elberg, Jinping Li, and Yoram Shechter. Vanadium activates or inhibits receptor and non-receptor protein tyrosine kinases in cell-free experiments, depending on its oxidation state. possible role of endogenous vanadium in controlling cellular protein tyrosine kinase activity. *Journal of Biological Chemistry*, 269(13):9521–9527, 1994.

[32] Masayuki Fukata, Anli Chen, Arunan S Vamadevan, Jason Cohen, Keith Breglio, Suneeta Krishnareddy, David Hsu, Ruliang Xu, Noam Harpaz, Andrew J Dannenberg, et al. Toll-like receptor-4 promotes the development of colitis-associated colorectal tumors. *Gastroenterology*, 133(6):1869–1869, 2007.

[33] M Gallorini, C Birattari, M Bonardi, L Magon, and E Sabbioni. Preparation of high specific activity radiotracers for radioanalytical studies. *Journal of radioanalytical and nuclear chemistry*, 160(2):549–561, 1992.

[34] Eric Garrido, C Duchemin, Arnaud Guertin, Ferid Haddad, Nathalie Michel, and Vincent Métivier. New excitation functions for proton induced reactions on natural titanium, nickel and copper up to 70 mev. *Nuclear Instruments and Methods in Physics Research Section B: Beam Interactions with Materials and Atoms*, 383:191–212, 2016.

[35] William Z Gelbart and Nigel R Stevenson. Solid targetry systems: a brief history. In *Proceedings of the 15th International Conference on Cyclotrons and their Applications, Caen, France, 14–19 June*, pages 90–93. Inst. Phys., 1998.

[36] Joseph G Hamilton. The rates of absorption of radio-sodium in normal human subjects. *Proceedings of the National Academy of Sciences of the United States of America*, 23 (9):521, 1937.

[37] Joseph G Hamilton and Mayo H Soley. Studies in iodine metabolism by the use of a new radioactive isotope of iodine. *American Journal of Physiology-Legacy Content*, 127 (3):557–572, 1939.

[38] David Harvey. High-Performance Liquid Chromatography, jun 5 2019. [Online; accessed 2022-03-09].

[39] Alex Hermanne, Sandor Takacs, Ferenc Szelecsenyi, Ferenc Tarkanyi, Michel Sonck, and Joeri Van Hoyweghen. The use of cross section data for monitoring charged particle beam parameters. In *15th Int. Conf. on Cyclotrons and their Applications, 246*, 1999.

[40] Alex Hermanne, Anatoly V Ignatyuk, Roberto Capote, Brett Vern Carlson, Jonathan W Engle, Mark A Kellett, Tibor Kibedi, Guinyun Kim, Filip G Kondev, Mazhar Hussain, et al. Reference cross sections for charged-particle monitor reactions. *Nuclear Data Sheets*, 148:338–382, 2018.

[41] George Hevesy. The absorption and translocation of lead by plants. a contribution to the application of the method of radioactive indicators in the investigation of the change of substance in plants. In *A Source Book in Chemistry, 1900-1950*, pages 48–50. Harvard University Press, 2013.

[42] RD Hichwa, D Kadrmas, GL Watkins, SD Wollenweber, S Maniam, LL Boles Ponto, JCW Richmond, and JA Koeppel. Vanadium-48: A renewable source for transmission scanning with pet. *Nuclear Instruments and Methods in Physics Research Section B: Beam Interactions with Materials and Atoms*, 99(1-4):804–806, 1995.

[43] Hitachi. Principle and system configuration of hplcbiologic quadtec uv/vis detector, Accessed 9 March 2022. URL `https://www.hitachi-hightech.com/global/products/science/tech/ana/lc/basic/course1.html#jump1`.

[44] Michibata Hitoshi, Seki Yuko, Hirata Junko, Kawamura Mieko, Iwai Kunihisa, Iwata Ren, and Ido Tatsuo. Uptake of 48v-labeled vanadium by sebpopelations of blood cells in the ascidian, ascidia gemmata. *Zoological science*, 8(3):447–452, 1991.

[45] FDA Home. Orange book: approved drug products with therapeutic equivalence evaluations. *US Food Drug Adm*, 2021.

[46] Jason Hon, Michelle S Hwang, Meara A Charnetzki, Issra J Rashed, Patrick B Brady, Sarah Quillin, and Marvin W Makinen. Kinetic characterization of the inhibition of protein tyrosine phosphatase-1b by vanadyl (vo2+) chelates. *JBIC Journal of Biological Inorganic Chemistry*, 22(8):1267–1279, 2017.

[47] Godfrey N Hounsfield. Computerized transverse axial scanning (tomography): Part 1. description of system. *The British journal of radiology*, 46(552):1016–1022, 1973.

[48] Brian F Hutton. The origins of spect and spect/ct. *European journal of nuclear medicine and molecular imaging*, 41(1):3–16, 2014.

[49] Masanori Ichise, Jeih-San Liow, Jian-Qiang Lu, Akihiro Takano, Kendra Model, Hiroshi Toyama, Tetsuya Suhara, Kazutoshi Suzuki, Robert B Innis, and Richard E Carson. Linearized reference tissue parametric imaging methods: application to [11c] dasb positron emission tomography studies of the serotonin transporter in human brain. *Journal of Cerebral Blood Flow & Metabolism*, 23(9):1096–1112, 2003.

[50] Kuni Iwai, Tatsuo Ido, Ren Iwata, Mieko Kawamura, and Shuichi Kimura. Localizing efficiency of [48v] vanadyl-pheophorbide in tumor as a new tumor imaging agent. *International Journal of Radiation Applications and Instrumentation. Part B. Nuclear Medicine and Biology*, 16(8):783–789, 1989.

[51] Ren Iwata, K Iwai, Tatsuo Ido, and S Kimura. Preparation of no-carrier-added 48 v (iv) and 48 v (v) for biological tracer use. *Journal of radioanalytical and nuclear chemistry*, 134(2):303–309, 1989.

[52] Frédéric Joliot and Irène Curie. Artificial production of a new kind of radio-element. *Nature*, 133(3354):201–202, 1934.

[53] Maureen Joseph. Hplc detector options for the determination of polynuclear aromatic hydrocarbons. *Varian Chromatography Systems*, 2012.

[54] C Kennedy, MH Des Rosiers, JW Jehle, M Reivich, F Sharpe, and L Sokoloff. Mapping of functional neural pathways by autoradiographic survey of local metabolic rate with [14c] deoxyglucose. *Science*, 187(4179):850–853, 1975.

[55] Mayeen Uddin Khandaker, K Kim, MW Lee, KS Kim, GN Kim, YS Cho, and YO Lee. Investigations of the natti (p, x) 43, 44m, 44g, 46, 47, 48sc, 48v nuclear processes up to 40 mev. *Applied Radiation and Isotopes*, 67(7-8):1348–1354, 2009.

[56] Susan C Kirkland. Dome formation by a human colonic adenocarcinoma cell line (hca-7). *Cancer Research*, 45(8):3790–3795, 1985.

[57] AJ Koning, D Rochman, J-Ch Sublet, N Dzysiuk, M Fleming, and S Van der Marck. Tendl: complete nuclear data library for innovative nuclear science and technology. *Nuclear Data Sheets*, 155:1–55, 2019.

[58] P Kopecky, F Szelecsenyi, T Molnar, P Mikecz, and F Tárkányi. Excitation functions of (p, xn) reactions on natti: monitoring of bombarding proton beams. *Applied Radiation and Isotopes*, 44(4):687–692, 1993.

[59] Adriaan A Lammertsma and Susan P Hume. Simplified reference tissue model for pet receptor studies. *Neuroimage*, 4(3):153–158, 1996.

[60] Ernest O Lawrence and M Stanley Livingston. The multiple acceleration of ions to very high speeds. *PhysIcal review*, 45(9):608, 1934.

[61] VN Levkovski et al. Cross sections of medium mass nuclide activation (a= 40-100) by medium energy protons and alpha-particles (e= 10-50 mev). *Inter-Vesi, Moscow, USSR*, 1991.

[62] M Stanley Livingston. The magnetic resonance accelerator. *Review of scientific instruments*, 7(1):55–68, 1936.

[63] M Stanley Livingston and Edwin M McMillan. History of the cyclotron (part 1, livingston; part 2 mcmillan). *Physics Today*, 12(10), 1959.

[64] Jean Logan, Joanna S Fowler, Nora D Volkow, Alfred P Wolf, Stephen L Dewey, David J Schlyer, Robert R MacGregor, Robert Hitzemann, Bernard Bendriem, S John Gatley, et al. Graphical analysis of reversible radioligand binding from time—activity measurements applied to [n-11c-methyl]-(-)-cocaine pet studies in human subjects. *Journal of Cerebral Blood Flow & Metabolism*, 10(5):740–747, 1990.

[65] Jean Logan, Joanna S Fowler, Nora D Volkow, Gene-Jack Wang, Yu-Shin Ding, and David L Alexoff. Distribution volume ratios without blood sampling from graphical analysis of pet data. *Journal of Cerebral Blood Flow & Metabolism*, 16(5):834–840, 1996.

[66] Marvin W Makinen and Matthew J Brady. Structural origins of the insulin-mimetic activity of bis (acetylacetonato) oxovanadium (iv). *Journal of Biological Chemistry*, 277(14):12215–12220, 2002.

[67] Marvin W Makinen, Ravinder Bamba, Lynda Ikejimba, Christian Wietholt, Chin-Tu Chen, and Suzanne D Conzen. The vanadyl chelate bis (acetylacetonato) oxovanadium (iv) increases the fractional uptake of 2-(fluorine-18)-2-deoxy-d-glucose by cultured human breast carcinoma cells. *Dalton Transactions*, 42(33):11862–11867, 2013.

[68] Katrina A Marsh, Gordon WH Stamp, and Susan C Kirkland. Isolation and characterization of multiple cell types from a single human colonic carcinoma: tumourigenicity of these cell types in a xenograft system. *The Journal of pathology*, 170(4):441–450, 1993.

[69] MATLAB. *Version 9.9.0.1397035 (R2020b)*. The MathWorks Inc., Natick, Massachusetts, 2020.

[70] G Muehllehner. Resolution limit of positron cameras. *Journal of Nuclear Medicine*, 17 (8):757–757, 1976.

[71] Devkumar Mustafi, Walter J Liszewski, Reba Mustafi, Anusara Chumsangsri, Marc Bissonnette, Elizabeth Peng, Gregory S Karczmar, John W Ejnik, and Heather Martin. A novel class of vanadium-based magnetic resonance imaging contrast agents for targeting colon cancer cells with high glycolitic activity. In *Gastroenterology*, volume 132, pages A169–A169. WB. Saunders Co.- Elsevier Inc., 2007.

[72] Devkumar Mustafi, Bo Peng, Sean Foxley, Marvin W Makinen, Gregory S Karczmar, Marta Zamora, John Ejnik, and Heather Martin. New vanadium-based magnetic resonance imaging probes: clinical potential for early detection of cancer. *JBIC Journal of Biological Inorganic Chemistry*, 14(8):1187–1197, 2009.

[73] Devkumar Mustafi, Jesse Ward, Urszula Dougherty, Marc Bissonnette, John Hart, Stefan Vogt, and Gregory S Karczmar. Xfm demonstrates preferential accumulation of a vanadyl-based mri contrast agent in murine colonic tumors. *Molecular imaging*, 14, 2015.

[74] Masami Nakai, Hiromi Watanabe, Chikako Fujiwara, Hisao Kakegawa, Toshio Satoh, Jitsuya Takada, Rokuji Matsushita, and Hiromu Sakurai. Mechanism on insulin-like action of vanadyl sulfate: studies on interaction between rat adipocytes and vanadium compounds. *Biological and Pharmaceutical Bulletin*, 18(5):719–725, 1995.

[75] Vesa Oikonen. Compartmental models, 2019. URL `http://www.turkupetcentre.net/petanalysis/model_compartmental.html`.

[76] Chromatography Online. The 0.1% tfa revolution—a sign of chromatographic laziness?, 2017. URL `https://www.chromatographyonline.com/view/01-tfa-revolution-sign-chromatographic-laziness-0`.

[77] Sanjay K Pandey, Jean-Francois Théberge, Michel Bernier, and Ashok K Srivastava. Phosphatidylinositol 3-kinase requirement in activation of the ras/c-raf-1/mek/erk and p70s6k signaling cascade by the insulinomimetic agent vanadyl sulfate. *Biochemistry*, 38(44):14667–14675, 1999.

[78] AI Papash and Yu G Alenitsky. Commercial cyclotrons. part i: commercial cyclotrons in the energy range 10–30 mev for isotope production. *Physics of Particles and Nuclei*, 39(4):597–631, 2008.

[79] A Papoulis. Probability, statistics, and random variables, 1991.

[80] Joseph Perl, Jungwook Shin, Jan Schümann, Bruce Faddegon, and Harald Paganetti. Topas: an innovative proton monte carlo platform for research and clinical applications. *Medical physics*, 39(11):6818–6837, 2012.

[81] F Poignant, S Penfold, J Asp, P Takhar, and P Jackson. Geant4 simulation of cyclotron radioisotope production in a solid target. *Physica Medica*, 32(5):728–734, 2016.

[82] RA Rowe and Mark M Jones. Preparation from vanadium (v) oxide through prior reduction to oxovanadium (iv) ion. *Inorganic Syntheses*, 5:114–114, 1957.

[83] Ernest Rutherford. Liv. collision of α particles with light atoms. iv. an anomalous effect in nitrogen. *The London, Edinburgh, and Dublin Philosophical Magazine and Journal of Science*, 37(222):581–587, 1919.

[84] E Sabbioni, E Marafante, L Amantini, L Ubertalli, and C Birattari. Similarity in metabolic patterns of different chemical species of vanadium in the rat. *Bioinorganic chemistry*, 8(6):503–515, 1978.

[85] Gopal B Saha. *Physics and radiobiology of nuclear medicine*. Springer Science & Business Media, 2012.

[86] Ulrich Schindewolf and JW Irvine. Preparation of carrier-free vanadium, scandium, and arsenic activities from cyclotron targets by ion exchange. *Analytical Chemistry*, 30 (5):906–908, 1958.

[87] David J Schlyer and Thomas J Ruth. Accelerator production of radionuclides. In *Industrial Accelerators and Their Applications*, pages 139–181. World Scientific, 2012.

[88] Thermo Scientific. Dionex onguard ii cartridges, 2017. URL `https://assets.thermofisher.com/TFS-Assets/CMD/manuals/Man-031688-IC-OnGuard-II-Cartridges-Man031688-EN.pdf`.

[89] IA Setyawati, KH Thompson, VG Yuen, Y Sun, M Battell, DM Lyster, C Vo, TJ Ruth, S Zeisler, JH McNeill, et al. Kinetic analysis and comparison of uptake, distribution, and excretion of 48v-labeled compounds in rats. *Journal of Applied Physiology*, 84(2): 569–575, 1998.

[90] LG Stang Jr, WD Tucker, HD Banks Jr, RF Doering, and TH Mills. Production of iodine-132. Technical report, Brookhaven National Lab.(BNL), Upton, NY (United States), 1954.

[91] Nobuo Suzuki, Makoto Takahashi, and Hisanori Imura. Substoichiometric liquid-liquid extraction and determination of vanadium based on the synergic effect of thenolytrifluoroacetone and trioctylphosphine oxide. *Analytica chimica acta*, 160:79–85, 1984.

[92] WG Sweet. Localization of brain tumors with positron emitters. *Nucleonics*, 11:40–45, 1953.

[93] C Tamburella and TJ Giles. Beam diagnostics for an 18 mev medical cyclotron. *Nuclear Instruments and Methods in Physics Research Section B: Beam Interactions with Materials and Atoms*, 266(19-20):4678–4681, 2008.

[94] Gabriele Tarantola, Felicia Zito, and Paolo Gerundini. Pet instrumentation and reconstruction algorithms in whole-body applications. *Journal of Nuclear Medicine*, 44 (5):756–769, 2003.

[95] Michel M Ter-Pogossian, Michael E Phelps, Edward J Hoffman, and Nizar A Mullani. A positron-emission transaxial tomograph for nuclear imaging (pett). *Radiology*, 114 (1):89–98, 1975.

[96] AC Thomson, DT Attwood, M Gullikson Eric, et al. X-ray data booklet center for x-ray optics and advanced light source, lawrence berkeley national laboratory, 2019.

[97] Geant4-A Simulation Toolkit. Guide for physics lists: Release 11.0, 2020. URL https://geant4-userdoc.web.cern.ch/UsersGuides/PhysicsListGuide/fo/PhysicsListGuide.pdf.

[98] Walter D Tucker, Margaret W Greene, Allen J Weiss, and Alex Murrenhoff. Methods of preparation of some carrier-free radioisotopes involving sorption on alumina. Technical report, Brookhaven National Lab., Upton, NY, 1958.

[99] Jan van der Valk, Karen Bieback, Christiane Buta, Brett Cochrane, Wilhelm G Dirks, Jianan Fu, James J Hickman, Christiane Hohensee, Roman Kolar, Manfred Liebsch, et al. Fetal bovine serum (fbs): past–present–future. *ALTEX-Alternatives to animal experimentation*, 35(1):99–118, 2018.

[100] Juan José Vaquero and Paul Kinahan. Positron emission tomography: current challenges and opportunities for technological advances in clinical and preclinical imaging systems. *Annual review of biomedical engineering*, 17:385–414, 2015.

[101] GR Willsky, AB Goldfine, PJ Kostyniak, JH McNeill, LQ Yang, HR Khan, and DC Crans. Effect of vanadium (iv) compounds in the treatment of diabetes: in vivo and in vitro studies with vanadyl sulfate and bis (maltolato) oxovandium (iv). *Journal of inorganic biochemistry*, 85(1):33–42, 2001.

[102] J Derek Woollins. *Inorganic experiments*. John Wiley & Sons, 2010.

[103] Paolo Zanotti-Fregonara, Renaud Maroy, Marie-Anne Peyronneau, Régine Trebossen, and Michel Bottlaender. Minimally invasive input function for 2-18f-fluoro-a-85380 brain pet studies. *European journal of nuclear medicine and molecular imaging*, 39(4): 651–659, 2012.

[104] S Zeisler and T Ruth. Preparation of [48 v]-vo 2+ for biomedical studies. *Journal of radioanalytical and nuclear chemistry*, 200(4):283–290, 1995.

[105] Shuang-Qing Zhang, Xu-Ying Zhong, Wan-Liang Lu, Li Zheng, Xuan Zhang, Feng Sun, Gui-Ying Fu, and Qiang Zhang. Pharmacodynamics and pharmacokinetics of the insulin-mimetic agent vanadyl acetylacetonate in non-diabetic and diabetic rats. *Journal of inorganic biochemistry*, 99(5):1064–1075, 2005.